Study on the electroforming and resistive switching behaviour of nickel oxide thin films for non-volatile memory applications

Robert Weng

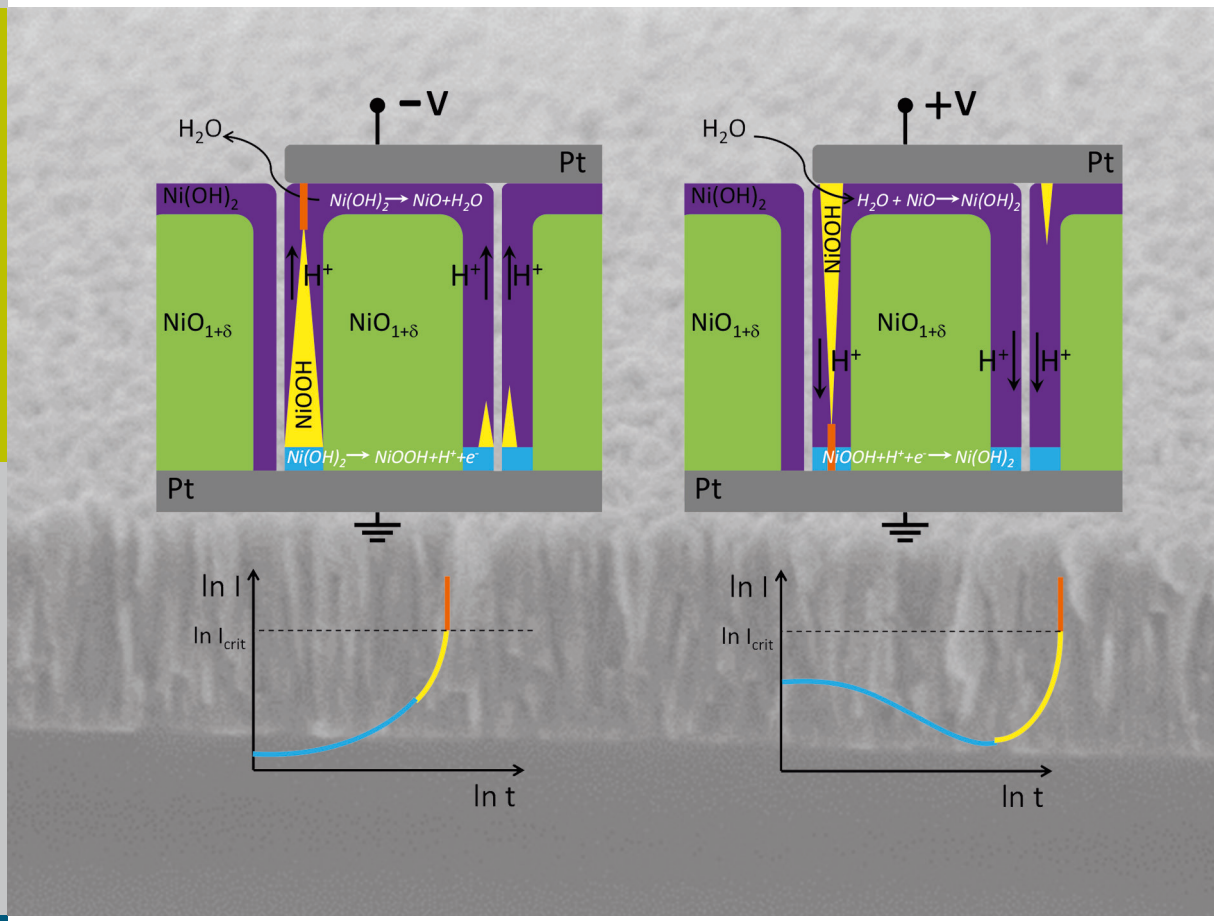

Schlüsseltechnologien / Key Technologies
Band / Volume 109
ISBN 978-3-95806-062-3

JÜLICH
FORSCHUNGSZENTRUM

Schriften des Forschungszentrums Jülich
Reihe Schlüsseltechnologien / Key Technologies Band / Volume 109

Forschungszentrum Jülich GmbH
Peter Grünberg Institute (PGI)
Electronic Materials (PGI-7)

Study on the electroforming and resistive switching behaviour of nickel oxide thin films for non-volatile memory applications

Robert Weng

Schriften des Forschungszentrums Jülich
Reihe Schlüsseltechnologien / Key Technologies Band / Volume 109

ISSN 1866-1807 ISBN 978-3-95806-062-3

Bibliographic information published by the Deutsche Nationalbibliothek.
The Deutsche Nationalbibliothek lists this publication in the Deutsche Nationalbibliografie; detailed bibliographic data are available in the Internet at http://dnb.d-nb.de.

Publisher and Distributor:	Forschungszentrum Jülich GmbH Zentralbibliothek 52425 Jülich Tel: +49 2461 61-5368 Fax: +49 2461 61-6103 Email: zb-publikation@fz-juelich.de www.fz-juelich.de/zb
Cover Design:	Grafische Medien, Forschungszentrum Jülich GmbH
Printer:	Grafische Medien, Forschungszentrum Jülich GmbH
Copyright:	Forschungszentrum Jülich 2015

Schriften des Forschungszentrums Jülich
Reihe Schlüsseltechnologien / Key Technologies, Band / Volume 109

D 82 (Diss. RWTH Aachen University, 2015)

ISSN 1866-1807
ISBN 978-3-95806-062-3

The complete volume is freely available on the Internet on the Jülicher Open Access Server (JuSER) at www.fz-juelich.de/zb/openaccess.

Abstract

Over the past decade, the resistance switching effect has drawn attention within the scientific community as a potential candidate for non-volatile random access memories (RAM) and crossbar logic concepts. The resistance switching memory cells are based on (at least) two well-defined non-volatile resistance states, e.g., high resistance state (HRS) and low resistance state (LRS), that define two (or more) logic memory states, e.g., 1 or 0. Often these cells have a simple capacitor structure and are therefore easy to fabricate. However, the market launch of RRAMs is hindered by several serious obstacles. For example, the underlying microscopical physical and chemical switching mechanism of RRAM devices is still under debate although various models have been proposed to explain the observed phenomena. By missing a deep understanding of the resistive switching effect on an atomistic scale, a reliable fabrication of predictable and well performing Gbit memory seems to be questionable.

This thesis is an attempt to develop and physically understand the nickel oxide (NiO) based resistive switching non-volatile memory devices. Although the underlying microscopical switching mechanism is still under debate, the macroscopic switching mechanism of this material system is often described by the creation and rupture of well-conducting nickel filaments embedded within an insulating NiO matrix, the so called fuse-antifuse mechanism. The resistive switching characteristics, essentials for future non-volatile memories, such as low voltage and current operation with high resistance ratio between HRS and LRS, fast switching speed, high retention and endurance are presented.

Additionally, the emphasis is layed on the understanding of the so called forming process. It describes the first resistance transition of the resistive switching device in which the proposed nickel filament is formed. Therefore, it is the key process for understanding the resistive switching phenomena. The statistical distribution of the observed forming process is studied under accelerated constant voltage stress conditions and at varying temperatures within the framework of the Weibull statistics.

To understand the physical and chemical nature of the filamentary structure, the influence of different ambient atmospheres and temperatures on the forming process is analyzed electrically as well as chemically by XPS analysis. Combining these results with the results of the potentiostatic breakdown studies, a model for the forming process in Pt/NiO/Pt non-volatile resistive switching memory devices is proposed.

Kurzfassung

Im Laufe des letzten Jahrzehnts hat der Widerstand Schalteffekt innerhalb der wissenschaftlichen Gemeinschaft verstärkt das Interesse geweckt als potenzieller Kandidat für nichtflüchtige Speicher mit wahlfreiem Zugriff (RRAM) und Crossbar-Logik Konzepte. Die Widerstand schaltenden Speicherzellen basieren auf (mindestens) zwei gut definierte nichtflüchtige Widerstandszustände zum Beispiel einen Zustand mit hohem Widerstand (HRS) und niedrigem Widerstand (LRS), die zwei (oder mehr) definierte logische Speicherzustände 1 oder 0 representieren. Oft haben diese Zellen eine einfache Kondensatorstruktur und sind daher einfach herzustellen. Allerdings stehen der Markteinführung von RRAMs ernsthafte Hindernisse entgegen. Beispielsweise wird der zugrunde liegende mikroskopische physikalische und chemische Schaltmechanismus der RRAMs noch immer kontrovers diskutiert, obwohl verschiedene Modelle vorgeschlagen wurden, um die beobachteten Phänomene zu erklären. Durch ein fehlendes tiefes Verständnis für die Phänomene des resistiven Schaltens auf atomarer Skala, scheint eine zuverlässige Herstellung von vorhersagbare und gut funktionierende Gbit Speicher fraglich zu sein.

Diese Arbeit stellt ein Versuch dar, Nickeloxid (NiO) basierte resistive schaltende nicht-flüchtige Speicher zu entwickeln und zu verstehen. Obwohl der zugrunde liegende mikroskopische Schaltmechanismus noch diskutiert wird, wird der makroskopische Schaltmechanismus dieses Materialsystems häufig beschrieben durch den Aufbau und das wieder Aufbrechen von gut leitenden Nickelfäden eingebettet in der isolierenden NiO Matrix, der sogenannte Fuse-Antifuse Mechanismus. Die resistiven Schalteigenschaften der Zellen, die essentielle Eigenschaften für zukünftige nichtflüchtige Speicher darstellen, wie niedrige Schaltspannung und -Strom mit hohem Widerstands-verhältnis zwischen HRS und LRS, schnelle Schaltgeschwindigkeiten, hohe Haltbarkeit und Ausdauer der Widerstandszustände werden vorgestellt.

Darüber hinaus liegt der Schwerpunkt dieser Arbeit auf das Vertiefen des Verständnisses des sogenannten Formprozesses. Dieser beschreibt den ersten Widerstandsübergang der resistiv schaltedenden Zelle, bei dem der angenommene Nickelfaden gebildet wird. Daher ist dieser Prozess der Schlüsselprozess zum Verständnis der Phänomene des resistiven Schaltens. Die stochastische Natur des Formprozesses wird mittels beschleunigten Studien mit konstanten Spannungen und bei unterschiedlichen Temperaturen im Rahmen der Weibull Statistik untersucht.

Um die physikalische und chemische Beschaffenheit der fadenförmigen Struktur zu verstehen, wird der Einfluss verschiedener umgebenden Atmosphären und Temperaturen auf den Formprozess sowohl elektrisch analysiert als auch chemisch analysiert durch XPS-Analyse. Aus der Kombination dieser Ergebnisse mit den Ergebnissen der potentiostatischen Studien wird ein Modell für den Formprozess in Pt/NiO/Pt nichtflüchtigen resistiv schaltenden Speicherzellen präsentiert.

Contents

List of Figures

List of Tables

Acknowledgements

This PhD thesis was performed at the Forschungszentrum Jülich, within the Peter Grünberg Institute (PGI). I felt very welcome at the PGI and in particular in the Electronic Materials department thanks to the great people working here. It is now a great pleasure to thank all those who have accompanied me on this exciting journey.

First of all, I sincerely thank Prof. Dr. Rainer Waser for giving me the opportunity to perform this thesis in his institute.

I thank my advisors, Dr. Carsten Kügeler, Dr. Rainer Bruchhaus for their guidance and support in my research for this thesis.

Especially, I wish to express my deep gratitude to Dr. Paul Meuffels for his kindness, constant support, motivation and feedback, and for always putting me back on the right track. He always made time for me, even if it was late at night, to discuss physics and many other topics. Not least, I want to thank him for the correction of this thesis.

My gratitude goes to Prof. Dr. Krystof Szot for being a source of inspiration and for giving me the opportunity to cooperate with him. During the joint experiments I learned many experimental skills, as well as several theoretical physical concepts. I also want to thank Dr. Ramanathaswamy Pandian for the many hours together at the TEM.

Without the technical support many experimental setups and processes would not have been possible to realize. Therefore, I want to thank Marcel Gerst, Hans Haselier, René Borowski, Manfred Gebauer, Holger John, Mirka Grates, Stefan Masberg, Jochen Friedrich and Georg Pickartz.

I am grateful to Maria Garcia and Martina Heins who have often guided me through the administrative labyrinth.

I warmly thank my officemates Serge Röhrig, Lars Steffens, Michael Paßens, Ying Li, Peigang Li and Thomas Selle for the fruitful discussions and a good laugh. Besides them I want to thank all the colleagues of the PGI-7 and the IWE-2 of the RWTH-Aachen University for the warm atmosphere.

My special thanks go to Dr. Rohit Soni, Dr. Doo-Seok Jeong, Dr. Sacha J. Van Albada, Dr. Hyo-Jeong Moon, Dr. Sandipan Mohanty, Dr. Sebastian Gliga, Dr Emmanuel Stiakakis, Dr. Martin Weides, Chanwoo Park, Hayato Katsu – and all the people I met in Jülich and who have accompanied me on this journey. We had a great time.

Finally, I dedicate this thesis to my family: my brother Stefan, my mother and father Ans and Friedrich Weng, as well as to my wife Jiahua Weng who has always had the greatest support and faith in me and of course to our lovely daughter Lea.

Robert Weng

1 Introduction

The modern knowledge and information technology based society has a never-ending desire for evermore faster and cheaper memory devices with simultaneously increasing data storage density [176]. However, the corresponding further down scaling according to *Moore's law* as shown in figure 1.1 is expected to run into physical limits in the near future [112]. Therefore, new memory concepts are needed to fulfill the further continuation of Moore's law.

In present-day information technology, very fast memory applications are realized by *Random Access Memories* (RAM). These kind of memories are organized in a matrix. The stored data can be accessed randomly, in other words, each memory cell can be addressed directly according to its storage address, which allows the fast data processing. In larger memory modules, however, the data is not accessed cell by cell, but by a *Word*. The width of a Word is determined by the width of the memory architecture.

RAM memory devices can be classified into volatile concepts, which exhibit information loss upon removal of the operating voltage, and into non-volatile concepts, which do not require any operating voltage to retain the stored information.

The most famous volatile RAM type is the *dynamic RAM* (DRAM). The information is stored in terms of the charge state of a minute capacitor. The simple configuration enables a very high data storage density, but the tiny capacity on the other hand gives rise to a fast discharge of the capacitors. Therefore, the memory cells have to be recharged regularly. This refresh rate depends strongly on the dimensions of the capacitors and therefore increases drastically by downscaling the device.

Another type of volatile RAM is called *static RAM* (SRAM). In contrast to DRAM no refresh cycle is needed to retain the information and the data is stored as long as the operating voltage is applied. This is realized by a bistable flipflop per saved Bit. This design enables fast read and write operations, but the size of the cell on the other hand is relatively large because of the required 6 transistors per memory cell. Therefore, SRAM is mostly used as cache and

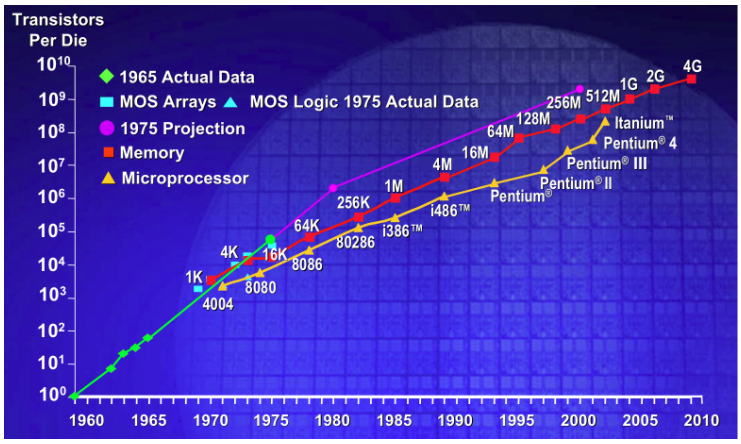

Figure 1.1: An illustration of Moore's law describing a long-term trend in the history of computing hardware. The number of transistors that can be placed inexpensively on an integrated circuit doubles approximately every two years. This trend has continued for more than half a century. [113].

main memory in computers and micro controllers.

The most prominent non-volatile memory concept is the *Flash memory*. In this type of memory, one Bit of information is saved by means of the charge state of a *floating-gate* within a field effect transistor. When the floating gate is uncharged, the source-drain channel of the field effect transistor is conducting, while a charged floating gate leads to a non-conducting source-drain channel. Information is read by the verification of the conductivity of the source-drain channel. To achieve non-volatile data storage the floating gate has to be electrically insulated. This memory design has advantages as non-volatility, high density and low cost fabrication and disadvantages as low endurance, low write speed and high voltages required for the write operation. Additionally, the further scaling of this technology is expected to run into physical limits in the near future.

The ultimate non-volatile memory should exhibit the non-volatility and low cost fabrication of the Flash memory, the fast write, erase and read access and the low energy operation of the SRAM, and the high density, high retention and high endurance of the DRAM. By regarding the combination of these requirements a *voltage-time dilemma* rises [177]. Write voltages (V_{write}) should be in the range of a few hundred mV to be compatible with scaled CMOS, while the length of a write voltage pulse should be smaller than $t_{write} < 10ns$. Because of constraints of the circuit design, read voltages V_{read} cannot be less than $\frac{1}{10}$ of V_{write} and the minimum read current should be $I_{read} \geq 1\mu A$, while $V_{read} \ll V_{write}$ is required to prevent a change of the written state. In contrast to the

fast read and write operations, the states should be retained for at least ten years ($t_{ret} \geq 10y$) during a constant stream of read pulses at at least $85°C$. To fulfill this combination of fast read and write operations and long retention, a ratio of $V_{write}/V_{read} \leq 10$ has to lead to an acceleration of the switching kinetics by a factor of $t_{ret}/t_{write} \approx 10^{16}$! There are only a few physical mechanisms that could give rise to such a huge non-linearity.

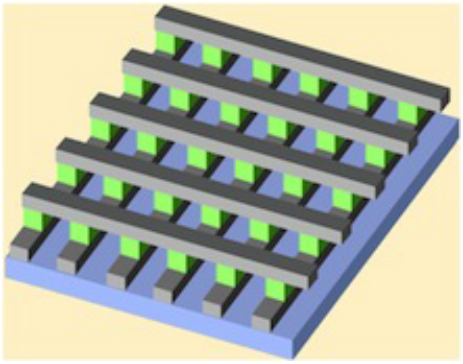

Figure 1.2: Schematic of a ReRAM crossbar array.

A very promising candidate which could fulfill all or at least many of these requirements is Resistive Random Access Memory (ReRAM) (see figure 1.2). The single ReRAM memory cell consists of a capacitor-like structure with an insulating layer, confined between two metallic electrodes. The resistance of these Metal-Insulator-Metal (MIM) cells can be switched between at least two distinct resistance states by external electrical stimuli. First reports of the resistive switching phenomena date back to as early as the 1960's [52, 35, 60, 131]. Successively, over several decades many attempts to explain the phenomena appeared and the resistive switching effect was observed to occur in a wide range of material systems [133, 160, 39, 140, 132], without considerable attention by the semiconductor industry. At the end of the 1990's however, publications of *Y. Watanabe et al.* [178], *Beck et al.* [15] and *Kozicki et al.* [86] led to a dramatic change and a new interest for resistive switching effects emerged in the scientific community as well as in semiconductor industry.

Within the scope of this work the resistive switching behaviour of memory devices with nickel oxide (NiO) as resistive switching material quenched between two metallic electrodes is investigated. Besides the resistive switching characterizations, the main focus in this thesis is on the understanding of the later described forming step, which is needed to convert the capacitor structure into a device capable of the resistive switching effect.

This thesis is structured in the following way. In chapter 2 a short overview on the resistive switching material systems, the associated switching characteristics

and a classification of the underlying switching mechanisms is given, with an emphasis on NiO.

Chapter 3 deals with the experimental methods used to fabricate and characterize the resistive switching NiO devices, followed by chapter 4, which describes the fabrication of the devices used in this work. To investigate the potential integration into CMOS and the related required performance of NiO-based memory devices, devices with several nanometer sized tungsten plugs were used as bottom electrodes. The drawback of the tungsten plugs is the inevitable oxidation of the plugs during the NiO deposition. Therefore also so called nano crossbar structures are made of 100 nm wide bottom platinum lines and 100 nm wide top platinum lines, that overlay each other in a resulting active cell area of 100 nm by 100 nm. Finally, to investigate the scaling properties, also devices with planar platinum bottom electrode and square platinum top electrodes were fabricated.

In chapter 5 the structural and electrical properties of the pristine films and devices are discussed. First, the influence of different nickel to oxygen ratios on the resistance of these NiO films is investigated and correlated with the theory of point defect chemistry. To study the morphology and crystal structure of the NiO films used for resistive switching, X-ray diffraction (XRD) and transmission electron microscopy (TEM) measurements are performed. Finally, to verify the scaling properties of resistive switching devices using NiO, the morphological and electrical behaviour of NiO films of different thicknesses are studied.

Chapter 6 attempts to verify the resistive switching behaviour and the associated critical physical quantities and values that trigger the transitions between the pristine state, the low resistance state (LRS) and the high resistance state (HRS).

Chapter 7 is dedicated to the study of the forming process. Therefore a detailed characterization and statistical analysis of the dielectric breakdown in NiO resistive switching memory devices under constant voltage stress and at elevated temperature conditions are discussed.

In chapter 8 the influence of different ambient atmospheres on the resistive switching devices is discussed. From these results a model for the forming process in NiO resistive switching memory devices is proposed.

Finally, in chapter 9 the results of this work are summarized and a short outlook on further required studies is given.

2 Fundamentals

In this chapter, a short overview on the resistive switching material systems, the associated switching characteristics and a classification of the underlying switching mechanisms is given. Furthermore, the basic crystallographic, magnetic and electrical properties of nickel oxide (NiO), the material system investigated in this work, are discussed in order to shed some light on the underlying mechanism of resistive switching in this material system.

2.1 Resistive switching

A typical resistive switching memory cell in a RRAM is configured as a insulator sandwiched between two, sometimes different, metallic electrodes resulting in a Metal-Insulator-Metal (MIM) structure. By applying the required voltage or current for a sufficient time, the resistance of the MIM cell can be switched between at least two distinct resistance states. The low resistance state is often referred to as the *ON state*, the high resistance state as the *OFF state*.

For the switching between these two resistance states two different switching modes can be distinguished, depending on the applied electrical stimuli and on the material systems involved. In the *unipolar* resistive switching mode, the transition from the ON state to the OFF state (*RESET process*) or vice versa (*SET process*) is independent of the voltage or current polarity. Both processes can take place at the same polarity or at different polarities, independently of each other. In the *bipolar* resistive switching mode however, the SET and RESET processes always occur at opposite voltage or current polarities. These behaviours are schematically shown in figure 2.1.

During the SET process in both resistive switching modes, the current is limited by a compliance current or by an external series resistor to prevent the device from permanent breakdown. Also transitions between bipolar and unipolar switching are reported in some material systems, depending on external settings, e.g., the current compliance [71, 156].

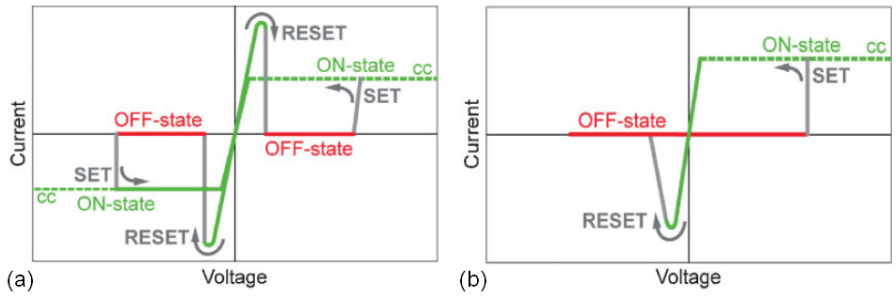

Figure 2.1: Schematic current-voltage characteristics of the two basic modes of resistive switching memory cells [177]. The voltage is thereby swept in a triangular shape and cc stands for the compliance current, which is set to prevent the device from hard breakdown. The dashed lines show the control voltage while the cc is in action. (a) The unipolar switching mode. Typically, the SET voltage in this mode is higher than the RESET voltage while the SET current is lower than the RESET current. (b) The bipolar switching mode. In this mode the SET operation occurs at one voltage or current polarity, while for the RESET operation the opposite polarity is required.

2.1.1 Classification of the resistive switching effects

The possible physical driving force behind the resistive switching phenomena observed in numerous material systems [161, 70, 110, 120, 89, 145, 125, 152, 76, 90, 91] can be very different: mechanical, thermal, electronic, chemical, magnetic, or a combination of these physical processes are discussed. A classification of the resistive switching effects based on the assumed underlying mechanisms can be found in a recent review by *Waser et al.* [177]. The special emphasis is here on redox-related chemical effects, which in their turn can be divided into the *electrochemical metallization effect* (ECM), the *valency change memory effect* (VCM) and into the *thermochemical memory effect* (TCM) (see figure 2.2).

ECM memory cells consist of an electrode made from an electrochemically active metal, such as Cu, Ag or Ni, an electrochemically inactive counter electrode, such as Pt, Ir, Au or W, and a thin insulating film acting as a solid electrolyte, sandwiched between both electrodes. The SET process in these cells utilizes an electrochemical metal deposition of the electrochemically active electrode material and involves three steps. First, the electrochemically active metal is ionized and dissolved into the solid electrolyte thin film. Thereafter, these dissolved *cations* migrate across the solid electrolyte under the action of the high external electrical field. Finally, when reaching the inert counter electrode, the cations are discharged again and electrocrystallize to small metallic clusters. Further electrocrystallization at such a cluster leads to the formation of a metal

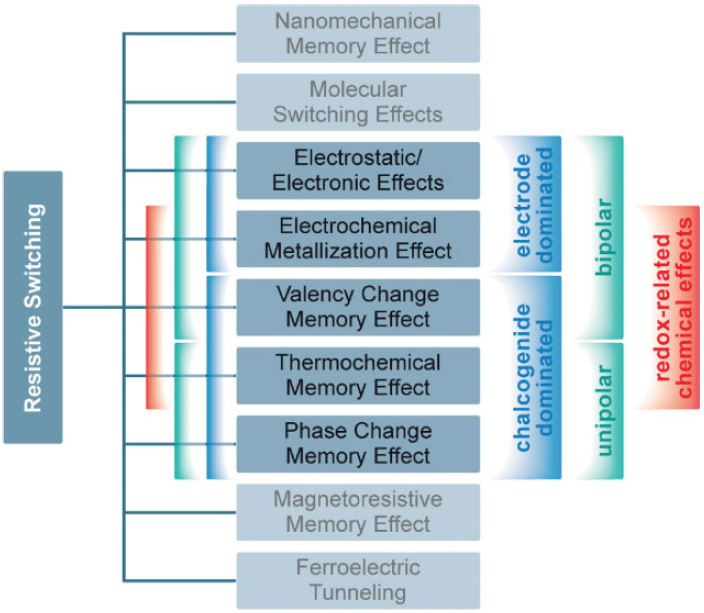

Figure 2.2: A classification of the resistive switching effects, which are considered for non-volatile memory applications [177].

filament, made of the electrochemically active metal, preferentially growing from the inert electrode towards the the active electrode. Since this process resembles building a metallic bridge from electrode to electrode, ECM cells are also called *conductive bridging* (CB) cells. The RESET process is realized by applying the opposite voltage polarity. Then, the active metal in the filament is ionized, dissolved into the solid electrolyte and migrates back towards the active metal electrode, where it is discharged again. The metallic bridge is dissolved and the OFF state is regained.

In many binary transition metal oxides and in many multinary oxides with at least one transition metal sublattice, however, bipolar resistive switching is found although no electrochemically active metal electrodes are used in the MIM structure. For the resistive switching in these material systems the transport of *anions*, instead of cations, is considered as essential. In many transition metal oxides, the mobility of oxygen related defects, such as oxygen vacancies, is much higher than the mobility of the transition metal cations. By applying an external voltage of sufficient strength and a certain polarity, an enrichment or depletion of oxygen vacancies will locally change the valence state of the transition metal cations, thereby giving rise to a local change in the electrical conductiv-

ity. Therefore, this type of resistive switching is referred to as *valence change memory* (VCM). Applying an external voltage of the opposite polarity will lead to a depletion or enrichment, respectively, which will restore the original valence state again. There are also many purely electronic and/or ionic switching mechanisms which are discussed, such as the charge-trap model [160, 130, 24, 56], trapping at interface states, which may affect the adjacent Schottky barrier at the metal/semiconductor interface [150, 51], and a insulator-metal-transition in strongly correlated electron systems [9, 48, 77, 109]. For the purely electronic models however, it has not been shown up to now how by such processes the earlier mentioned voltage-time dilemma (see chapter 1) can be overcome.

The third class of the redox-related resistive switching effects, the *thermochemical memory effect* (TCM), is primarily based on *thermal effects* and shows *unipolar* resistive switching. The most prominent material out of many that can be classified as TCM is NiO, the material investigated in this work. The first resistive switching in NiO was reported in 1964 by *Gibbons and Beadle* [52] at the Stanford Electronics Laboratories in Stanford, California. They already suggested a unipolar switching model in terms of a conducting metallic filament which forms a bridge between the ohmic contacts they used. According to this model the establishment of this filament, either by diffusion of excess nickel from the region surrounding a void or pinhole into these defects or by migration and accumulation of nickel atoms along defects due to the high electric field, sets the device into the ON state. Its rupture, due to Joule heating, turns the device into the OFF state again.

2.1.2 Resistive switching in NiO

Investigations concerning the *scaling properties* of the resistance states in NiO [13, 154, 4, 36] indicate that the resistance of the pristine devices, as well as the OFF resistances show some dependence on the electrode area, while the ON resistance is almost independent of the electrode area. This is a strong indication for a uniform current density over the entire electrode area in the pristine and OFF state, while the current in the ON state seems to be localized, supporting the assumption of a filamentary conduction in the ON state. Whether there is only a single filament, as indicated by an electrode area independent ON resistance [154, 36, 158, 66], or there are multiple filamentary current paths in the ON state, which are randomly distributed and randomly appear and disappear [4, 82, 184], as indicated in figure 2.3, is still under debate.

The *temperature dependence* of the ON state resistance typically shows a weak metallic behaviour for which a relative resistance ratio of $\frac{R(300K)}{R(5K)} = 1.6$ has been found [80]. This value is well below typical values of pure metals. This indicates that the filament is made of a defective and impure metallic conducting phase. For temperatures $T > 200$ K, the OFF state resistance shows a semiconducting behaviour with a thermal activation energy between 100 to 150 meV [36, 158, 72, 80]. At low temperatures ($T \leq 250$ K) however, *Jung et al.* found that

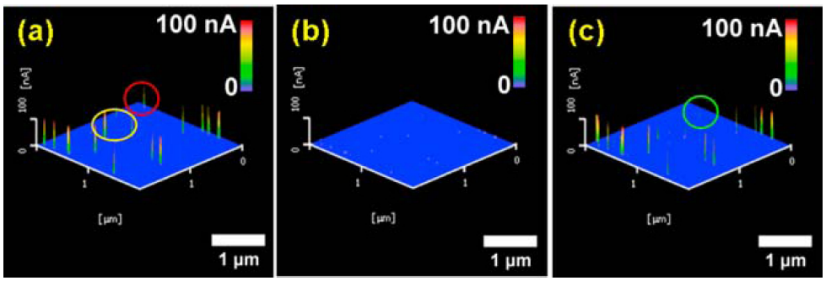

Figure 2.3: Local conductive atomic force microscope (LC-AFM) scans of NiO/Pt samples, covered with an ultra thin (5 nm) Pt top electrode. (a) represents the currents measured in the ON state, (b) the currents measured in the OFF state and (c) the currents measured in the subsequent ON state. The samples are switched between ON and OFF state by the application of voltage sweeps using a semiconductor analyzer. Note the different distribution of conducting spots in (a) and (c), indicating a random appearance and dissolution of conducting spots during switching [184].

the OFF state resistance again exhibits a n-type conductivity (see figure 2.4). According to *Jung et al.* [72] this is due to metallic remains of the disrupted filament which are left in the film. Because of the strong temperature dependent resistance of semiconducting NiO (correlated barrier hopping, see chapter 2.2.3), the contribution of metallic residuals in the film becomes more dominating at lower temperatures.

There is also a discussion about the *shape of the filament*. *Lee et al.*[96] used the percolation theory to explain the dependence of the voltage needed for RESET switching on the previous ON state resistance, R_{ON}, as shown in figure 2.5. The observation of two different regimes found for the I-V charcteristics depending on R_{ON} is hereby explained by the connectivity between the conducting filamentary branches. According to *Lee et al.*, when $R_{ON} < R_{CO}$ all of the conducting branches are multiply connected. When the number of branches decreases, the R_{ON} value increases, the Joule heating in each channel increases and I_{RESET} and V_{RESET} can thus decrease to achieve the breaking of the filament. When $R_{ON} > R_{CO}$ some of the conducting channels become singly connected. In this channel, all of the current should merge. Then, an increase of R_{ON} should be related to an increase of the length of the singly connected channel ($R = \rho \frac{l}{A}$, where R is the resistance, ρ is the resistivity, l is the length and A is the cross section of a conducting channel). Thus, I_{RESET} should be nearly constant, and V_{RESET} should increase. However, due to Joule heating and the metallic conduction of the filament, I_{RESET} decreases with an increase of R_{ON}.

This picture of the filament shape is also supported by the experiments per-

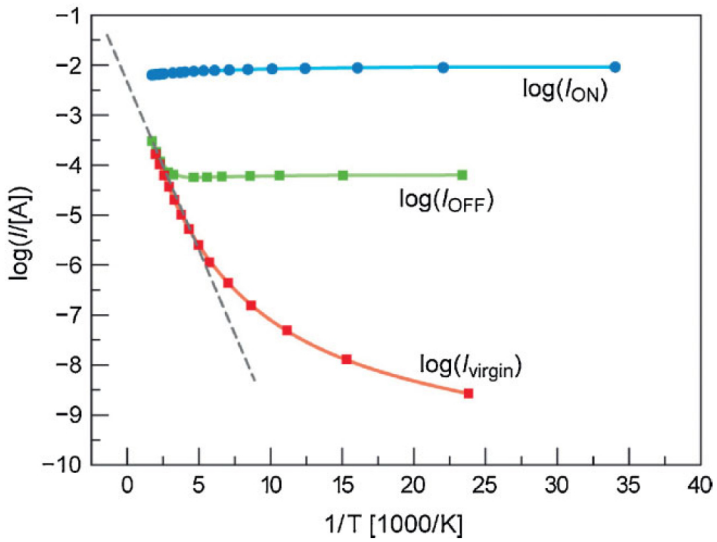

Figure 2.4: The temperature dependence of the conductivity of Pt/NiO/Pt thin films in the pristine state (red), the OFF state (green) and in the ON state (blue) [177].

formed by the group of *Park et al.* [136]. They switched a Pt/NiO/Pt device into the OFF state, ON state and into a permanent ON state, that could not be switched back to the OFF state again. Then, high-resolution transmission electron microscope (HR-TEM) and high-angle annular dark-field scanning transmission electron microscopy (HAADF-STEM) studies with atomic resolution were carried out on cross-sections of these devices, as shown in figure 2.6. In the permanent ON state, electron energy loss spectra (EELS) indicate excess nickel at the grain boundaries, which could not be detected in the pristine or in the OFF state. Based on these results *Park et al.* [136] suggested that the voltage stress during the SET process randomly generates narrow filamentary Ni paths in the NiO film. As grain boundaries are more conductive and defective than other regions, they expect that the percolating filaments (red lines in figure 2.6) will be shaped like a flash of lightning through the Ni enriched NiO grain boundaries. Unfortunately, no excess of metallic Ni could be detected in the samples which were in the "normal" ON state. This is illegible by the narrow size and smaller number of the filaments in the ON state, compared to the permanent ON state. Additionally, a decrease of the grain size at the anode and a roughening of that interface was observed after SET operation, indicating local reduction or oxidation at the anode, according to *Park et al.* [136]

A more fundamental driving force behind the *SET operation* is given by *Waser et al.* [177]. Above a critical electrical field strength all insulating/semiconducting

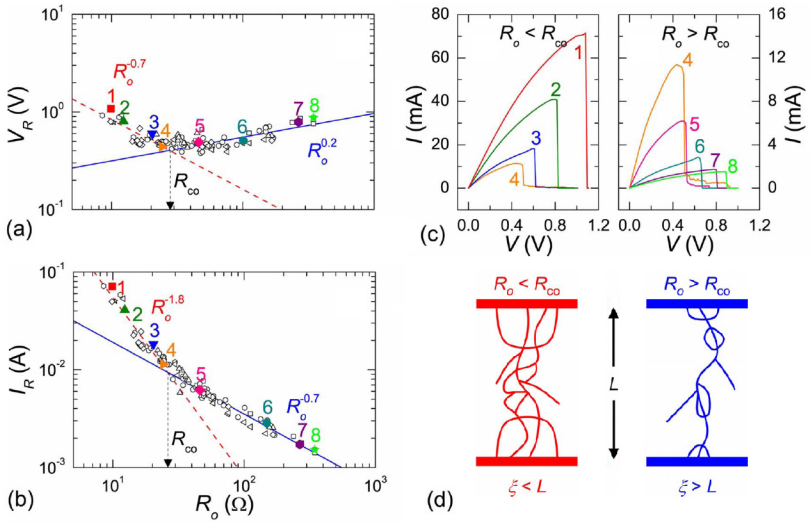

Figure 2.5: (a) The dependence of reset voltage V_{RESET} on R_{ON} and (b) the dependence of reset current I_{RESET} on R_{ON} (here R_o). At $R_{CO} \sim 30\Omega$, the power law dependence for both V_{RESET} and I_{RESET} change. I-V curves of eight selected data points are plotted for $R_{ON} < R_{CO}$ regime ((c) left) and for $R_{ON} > R_{CO}$ regime ((c) right). (d) shows schematic diagrams for the connectivity of the conducting filaments in the two regimes. The conducting filamentary branches are multiply ($R_{ON} < R_{CO}$) and singly connected ($R_{ON} > R_{CO}$) [96].

oxides endure a dielectric breakdown. This breakdown is typically induced be a thermal runaway process. The applied electric field induces a current, which leads to an increase of the temperature because of Joule heating. A temperature increase gives in turn rise to a current increase because of the semiconducting behaviour of the material. Under certain conditions, this self-amplifying process leads to a thermal runaway and may end in a final thermal breakdown. The proposed general driving force behind the SET operation is considered to be the change in the free energy of formation of all stable oxides, which favors lower valence state oxides at higher temperatures (see figure 2.7). Thus, the heating of an oxide under fixed oxygen partial pressure will therefore always lead to the formation of a stable oxide with a lower valence or of the corresponding metal, in case a given temperature is reached.

A model for the *RESET operation* is proposed by *Russo et al.* [148]. They performed an electrochemical simulation of an assumed cylindric metal filament in a NiO matrix to describe the measured RESET I-V curves [148]. Although these calculations, shown in figure 2.8 fit the experimentally measured curves

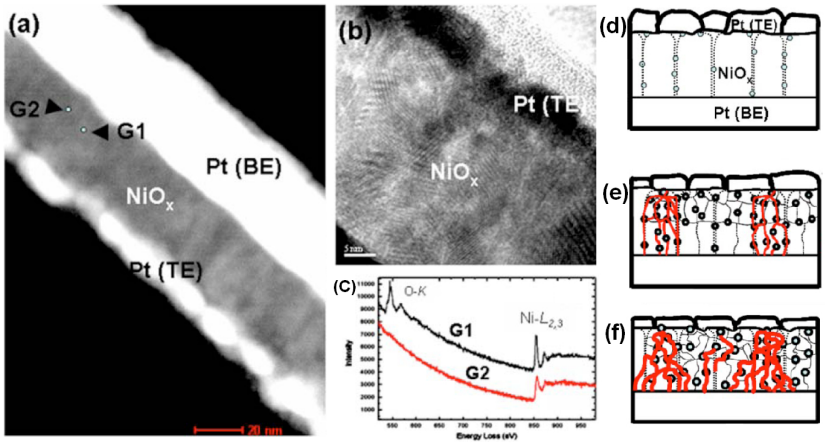

Figure 2.6: A cross-sectional HAADF-STEM image (a) and a HR-TEM image (b) of a Pt/NiO/Pt stack in the permanent ON state. (c) shows electron energy loss spectra taken from the area G1 (grain) and area G2 (grain boundary) with a probe size of $\sim 1nm$. (d) shows a schematic view for a Pt/NiO/Pt stack in the as-grown state, in the ON state (e), and in the permanent ON state (f) according to the model proposed by *Park et al.* [136].

surprisingly well, the suggestion that the dissolution of the filament occurs near the central region, is in conflict with the experimental results of *Park et al.* [136] discussed earlier, who found that switching in NiO occurs in the anodic region. Also *Kinoshita et al.* [81] found similar results. They switched several NiO films by means of a LC-AFM into the ON and OFF state using different polarities in each case. Subsequent Pt sputtering on the switched region of the NiO film did not change any of the ON states.Samples in the OFF states which were resetted by negative bias did also not change their state. Only samples in the OFF states which were before resetted with positive polarity changed their state into the ON state after the sputtering. The authors assume that the broken parts of the filaments in the OFF states can only be reconnected at the surface of the NiO film by the Pt sputtering process. From this result it is deduced that the switching (breaking of the filaments) occurs near the anode and not at the cathode or in the central region of the filament.

Nevertheless, from the results of *Russo et al.* [148] it is clear that *temperature* is an important factor in resistive switching in TCM material. In combination with the other findings the thermal properties of the electrodes should have a significant influence on the resistive switching properties. *Chang et al.* [31] experimentally found, that by decreasing the thickness of the Pt bottom electrodes, resistance memory switching in Pt/NiO/Pt devices becomes unstable and turns into threshold switching. In threshold switching, the ON state is volatile and

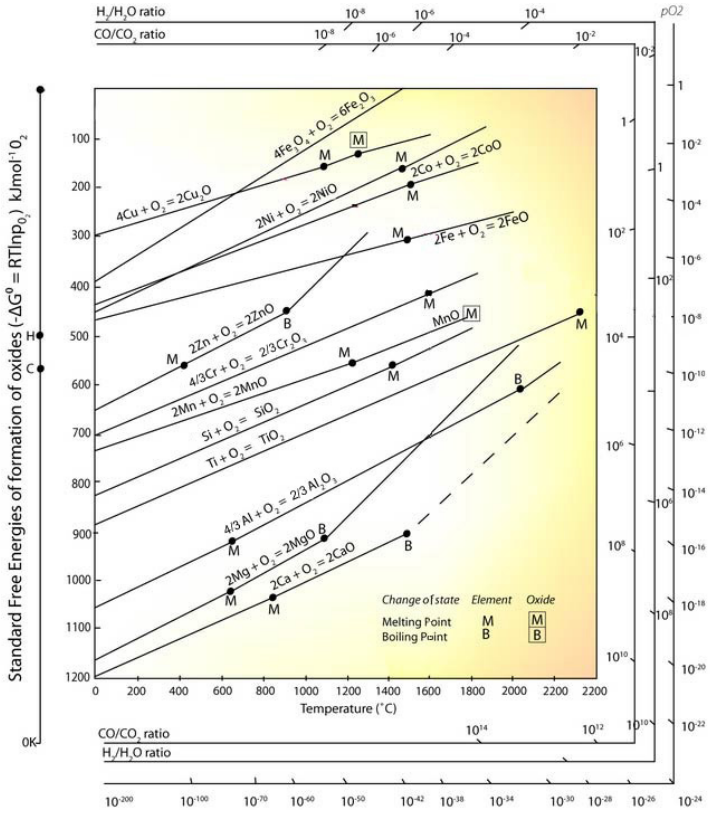

Figure 2.7: The Ellingham Richardson diagram of various transition metal oxides [44].

falls back into the OFF state below a certain threshold voltage. An electro-thermal simulation of these TCM cells explains this bottom-electrode-thickness dependent behaviour in terms of the thermal stability of the conducting filaments [31].

All of the above discussed calculated and experimental results indicate, that the *voltage-time dilemma* for TCM may be overcome by the local formation of different phases (on the nanoscale) [177]. However, despite the numerous studies on the switching in NiO, the mechanism behind the formation and rupture of the metallic filaments and the nature of the filaments are still not clear yet. In the next section, the basic crystallographic, magnetic and electrical properties of NiO are discussed, in order to shed some light on the understanding of the underlying resistive switching mechanisms in this material system.

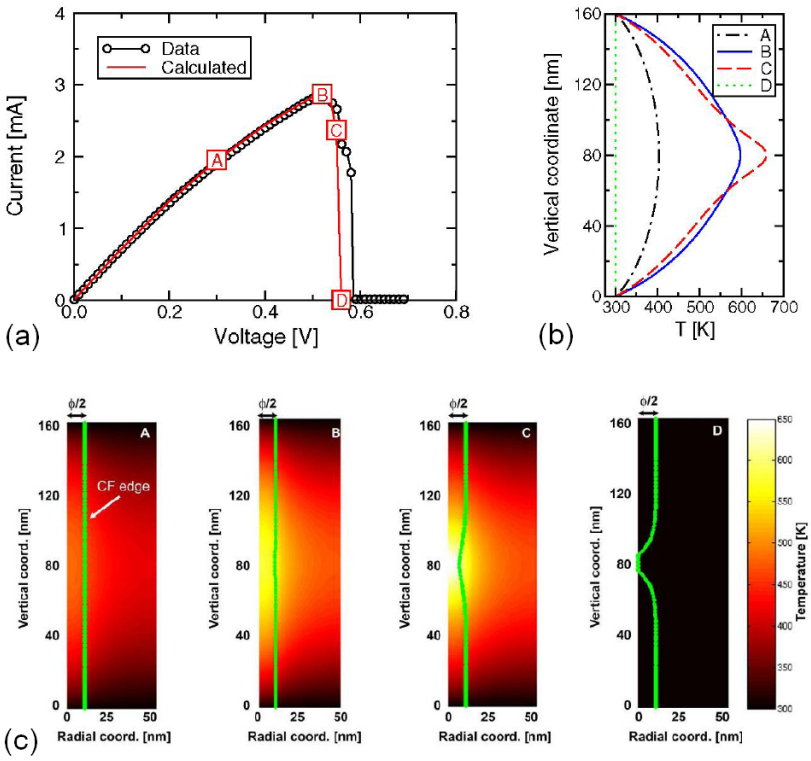

Figure 2.8: (a) Measured and calculated I-V curve during RESET of a 160nm thick NiO film on n-Si and with Au top electrodes. Bias points A, B, C and D, corresponding to simulation results in the figure on the right. (b) Simulation results for thermal dissolution of the conductive filament CF. The dissolution is faster at the hot spot (the middle of the filament in the figure). The formation of a bottleneck further enhances Joule heating due to current crowding, resulting in a self-acceleration of RESET. (c) Also shown is the temperature profile along the cylindrical axis in the filament, for the four bias points. ϕ denotes the filament diameter [177].

2.2 Nickel oxide: a correlated system

Nickel oxide is a really remarkable solid, because of its exceptional electrical and magnetic properties. Depending on the manufacturing conditions it's colour can be either dark green or black. Due to nickel oxide also the construct of the band theory threatened to collapse. According to the band theory namely, nickel oxide should be as conductive as a metal, because the $3d$-band of the Ni^{+2}-ion is only partially occupied. As a matter of fact though pure nickel oxide is a very good insulator.

2.2.1 Crystal structure

For a long time it was thought that nickel oxide has the *rock salt structure*. Seen from a threefold axis of rotation, for example from the (111)-direction, one can recognize that plains of O^{-2}-ions and plains of Ni^{+2}-ions alternate. Both the Ni^{+2}-ions and the O^{-2}-ions form in themselves a face-centered-cubic structure. Like all face-centered-cubic structures, the structure of nickel oxide can be described by a *rhombohedral* unit cell with an angle $\alpha = 60°$ and an edge length $a = \frac{a_0}{\sqrt{2}}$,where a_0 is the edge length of the cubic unit cell. The ratio of the atomic radii of the Ni^{+2}- and O^{-2}-ions is $\frac{r(Ni^{+2})}{r(O^{-2})} = 0.49$. This involves a compression of the rock salt structure in the (111)-direction resulting in the thermodynamically stable rhombohedral structure of nickel oxide. At room temperature ($T = 18°C$) the rhombohedral angle is $\alpha = 60°4.2'$ and at the temperature of liquid nitrogen ($T = -183°C$) the rhombohedral angle is $\alpha = 60°12'$. Heating the crystal leads to a relaxation of this compression and above $T = 250°C$ nickel oxide adopts the ideal rock salt structure with $\alpha = 60°$ (see figure 2.9) [144].

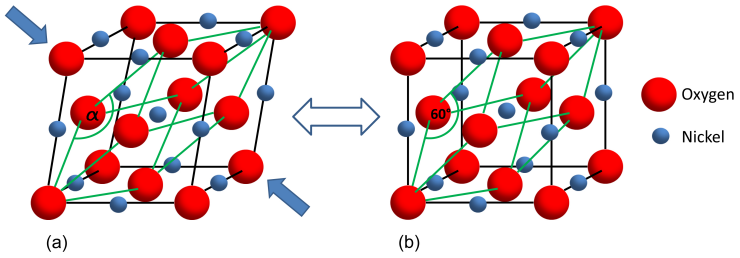

Figure 2.9: (a) The rhombohedral distorted crystal structure of NiO at lower temperatures $T < 250°C$. (b) Relaxation along the (111) axis results in the rock salt structure of NiO with $\alpha = 60°$ for temperatures $T > 250°C$. The cubic and the rhombohedral unit cells are indicated by the black and the green lines, respectively.

2.2.2 Magnetic properties

The bivalent nickel ion exhibits the $3d^8$-valence electron configuration. Thereby, the eight valence electrons occupy the five $3d$-orbitals in the following way:

Obviously there are two unpaired electrons left over. Therefore, one would expect a paramagnetic behaviour following *Curie's law* [10]

$$\chi = \frac{N}{V}\frac{(g \cdot \mu_B)^2}{3}\frac{J(J+1)}{k_B T}, \tag{2.1}$$

where N is the number of ions that contribute to the magnetization in the Volume V, g is the Landé factor, μ_B is the Bohr magneton and J is the total electronic angular momentum. In this case, the thermal lattice vibrations disturb the orientations of the magnetic moments in the external field, causing a decrease of the magnetic susceptibility and magnetization with increasing temperature.

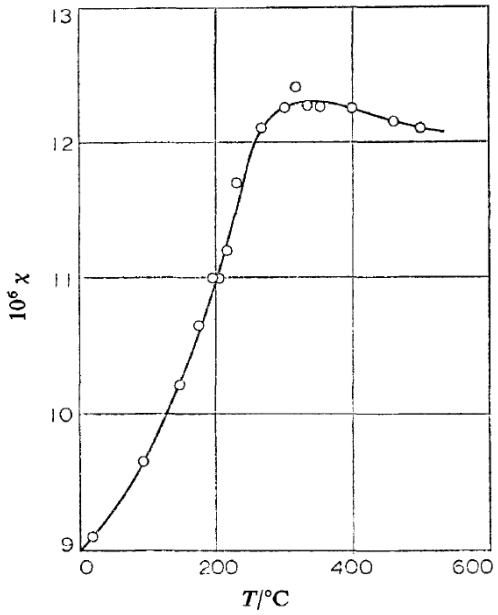

Figure 2.10: The molar magnetic susceptibility χ of NiO as a function of the temperature [41].

Measurements of the molar magnetic susceptibility χ of NiO as a function of the temperature are shown in figure 2.10. One observes an increase of χ with rising temperature and only above $T \approx 250°C$ a behaviour according to Curie's law is found. This is a typical behaviour of *antiferromagnetic* substances which exhibit a transition from antiferromagnetism into paramagnetism at the *Néel temperature*. In the case of NiO, the Néel temperature $T_N = 250°C$ is equal to the temperature where the rhombohedral structure changes into the rock salt structure [58].

In antiferromagnetic substances the spins are oriented regularly, but they do not point all in the same direction. In the case of NiO the spin orientation of one Ni^{+2}-layer is exactly opposite to that of the following layer and so on. That is the reason why the spins do not add to a total moment.

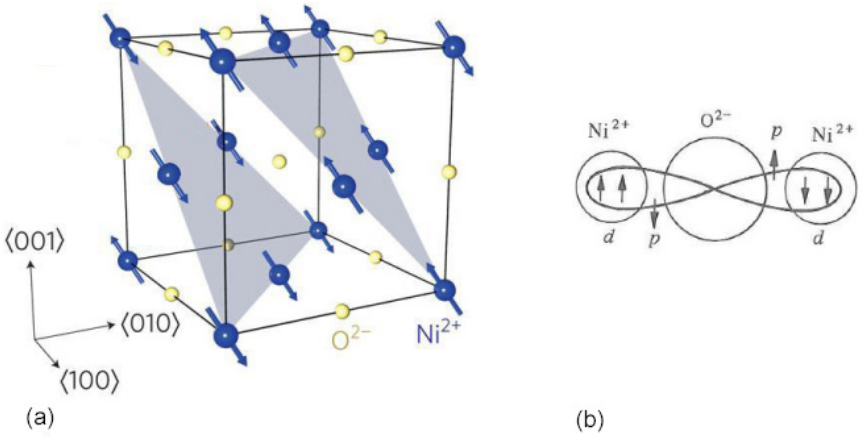

Figure 2.11: (a) The crystallographic unit cell or half of the magnetic unit cell of NiO [73]. The arrows indicate the spin orientation of the Ni^{+2}-ions. (b) The super exchange or the coupling between the d-electrons of the Ni^{+2}-ions across the O^{-2}-p-electrons [114].

As shown in figure 2.11 the resulting *magnetic unit cell* has an edge length exactly twice as large as the crystallographic edge length. To achieve such a spin configuration there must be an interaction between the Ni^{+2}-planes even though there is a O^{-2}-plane in between them, which does not directly contribute to the magnetic behaviour. This long range interaction is realized by a *super exchange mechanism* as first proposed by *Anderson* [7, 8]. The mechanism is schematically shown in figure 2.11. The $3d$-electrons of a Ni^{+2}-ion magnetically couple with the $2p$-electrons of an O^{-2}-ion, which in turn couple to the $3d$-electrons of another Ni^{+2}-ion in the next Ni^{+2}-plane.

2.2.3 Electronic properties

According to the classical *band theory* in the one electron approximation, transition metal oxides like NiO should be metallic conductors since the $3d$-bands which are constructed from the $3d$-orbitals of the metal elements are not filled up completely. As first pointed out by *de Boer* and *Verwey* in 1937 [20] the actual finding that NiO is an insulator contradicts this expectation.

To elucidate this contradiction, *Peierls* suggested that Coulomb interactions between the electrons is the cause of the discrepancy [118]. Theoretical investigations by *Mott* and *Hubbard* established later the concept of the *Mott-Hubbard insulator* for NiO [117]. In this model the so called *Hubbard Hamiltonian* is given as [6]

$$\hat{H} = -t \sum_{<\mathbf{i},\mathbf{j}>,\sigma} c^{\dagger}_{\mathbf{i}\sigma} c_{\mathbf{j}\sigma} + U \sum_{\mathbf{i}} \hat{n}_{\mathbf{i}\uparrow} \hat{n}_{\mathbf{i}\downarrow}, \tag{2.2}$$

where $c^{\dagger}_{\mathbf{i}\sigma}$ is the operator which creates an electron of spin σ on lattice site $\mathbf{i}$. Similarly, $c_{\mathbf{i}\sigma}$ is the annihilation operator, and $\hat{n}_{\mathbf{i}\sigma} = c^{\dagger}_{\mathbf{i}\sigma} c_{\mathbf{i}\sigma}$ is the number operator.

The first term of equation (2.2) is the kinetic energy or transfer integral. It describes the annihilation of an electron of spin σ on site $\mathbf{j}$ and its creation on site $\mathbf{i}$ (or vice-versa). The symbol $< \mathbf{i}, \mathbf{j} >$ emphasizes that hopping of the electrons is allowed only between two adjacent sites. As a first approximation, only hopping between the closest atoms in the lattice is allowed, since wavefunctions die off exponentially. The second term is the Coulomb interaction energy between the electrons with up and down spin on the same atom and is the origin of the electron-electron interactions or also called *electron correlation* [115]. It goes through all the sites and adds an energy U if it finds that the site is doubly occupied.

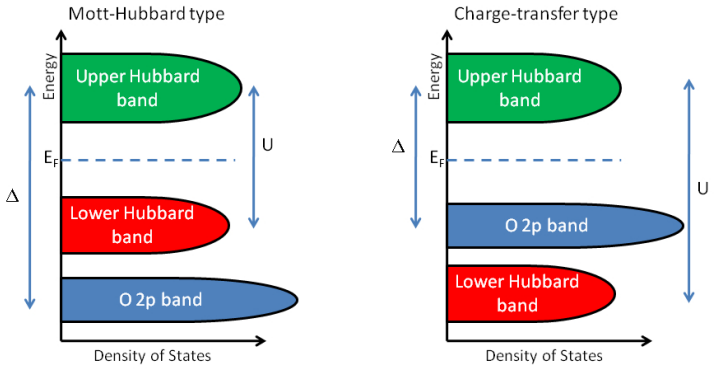

Figure 2.12: Schematic of Mott-Hubbard and charge-transfer insulators.

The ground states of the *Hubbard Hamiltonian* given by equation (2.2) are itinerant states when $t \gg U$ or localized states when $t \ll U$. The formation of an energy gap preventing conduction can thereby be understood as the competition between the repulsive Coulomb interaction between $3d$-electrons and the transfer integral of $3d$-electrons between neighboring atoms. The band gap in a *Mott-Hubbard insulator* exists between bands of similar character, such as $3d$ character and can be described by

$$\left(Ni^{+2}O^{-2}\right)_2 \rightarrow Ni^{+3}O^{-2} + Ni^{+1}O^{-2}. \tag{2.3}$$

On the other hand, the band gap in *charge transfer insulators* exists between anion and cation states, as shown in figure 2.12 and can be described by

$$Ni^{+2}O^{-2} \rightarrow Ni^{+1}O^{-1}. \tag{2.4}$$

In this case, there is no electron transfer between unit cells, only within a unit cell. Therefore, NiO is categorized as *charge transfer insulator*, since it exhibits an energy gap between the O $2p$ and Ni $3d$ bands [92, 151, 111] (see figure 2.13).

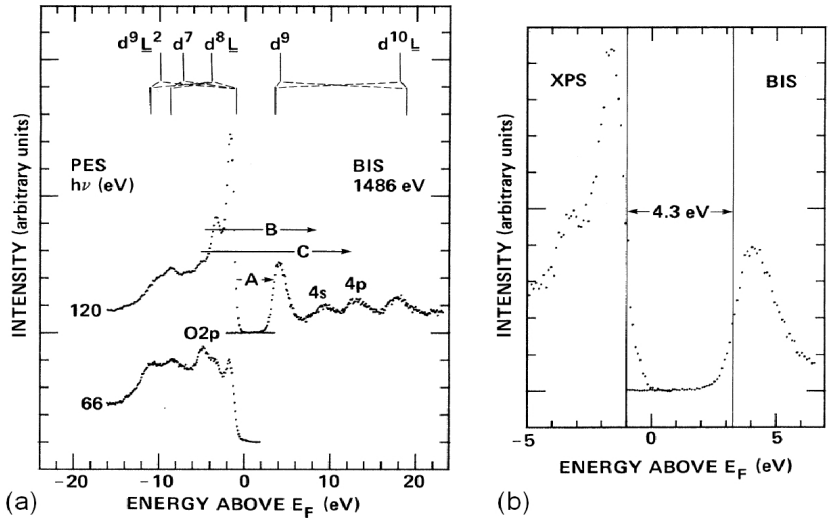

Figure 2.13: (a) The complete valence band structure of NiO [151]. The arrows A (4.3 eV), B (13.5 eV), and C (17.3 eV) correspond closely to structures found in the optical absorption spectrum of NiO [141]. (b) Extract of (a) around the bandgap. Both the valence- and conduction-band edges must have extremely sharp cutoffs. Based on this assumption the band gap is 4.3 eV, measured as indicated [151].

However, the conductivity of NiO is drastically increased when prepared in the form of thin films or consolidated nanoparticles due to the holes generated by Ni vacancies in the NiO lattice [103, 17]. *Makhlouf et al.*[103] found, that for temperatures $T > 200$ K, a band like conduction due to thermally activated *large polarons* in the O $2p$ band with an activation energy of $E_A = 0.3$ eV - 0.6 eV is dominating. At low temperatures $T < 200$ K, however, the conductivity is only weakly temperature dependent, as shown in figure 2.14. In this temperature range the number of thermally activated large polarons is so small, that *small polaron conduction* by means of thermally activated *hopping* with an activation energy of $E_A = 0.01$ eV dominates the conductivity [103]. This behaviour and the additionally observed strong increase of the conductivity for frequencies $\nu > 10^4$ Hz are described by the *correlated barrier hopping* (CBR) model [100, 46].

In this model, first proposed by Pike [138] in 1972, conductivity is explained by an electron transfer by thermal activation over the barrier between two sites, each having a Coulomb potential well associated with it. For neighboring sites at a separation R, the Coulomb wells overlap, resulting in a *lowering of the effective barrier* from W_M to a value W as shown in figure 2.14. W_M is the barrier height for an *infinite* intersite separation and thus corresponds to the energy to take the charge carrier from the defect state into the continuum. As we assume *holes* to be the charge carriers in NiO, the continuum is the *upper edge of the valence band* and the defect states are situated just above, in the bandgap [101].

For the case of a single electron (or hole) transition, W is given by

$$W = W_M - \frac{e^2}{\pi\varepsilon\varepsilon_0 R}, \tag{2.5}$$

where ε_0 is the permittivity of free space, ε is the relative permittivity of (in this case) NiO and e is the elementary charge. When we assume N defect states randomly distributed in space with an energy distribution width of Δ_0 in the bandgap, the a.c. conductivity in the narrow-band limit ($\Delta_0 \ll k_B T$) is given by [138, 100]

$$\sigma(\omega) = \frac{1}{24}\pi^3 N^2 \varepsilon\varepsilon_0 \omega R_\omega^6, \tag{2.6}$$

where the hopping distance R_ω at a frequency ω is given by

$$R_\omega = \frac{e^2}{\pi\varepsilon\varepsilon_0[W_M - k_B T \ln(\frac{1}{\omega\tau_0})]}, \tag{2.7}$$

where k_B is the Boltzmann constant, T is the temperature and τ_0 is a characteristic relaxation time of the order of the inverse Debye frequency [103]. The *frequency dependence* of the a.c. conductivity in the CBH model is embodied in the ωR_ω^6 factor and can be expressed as

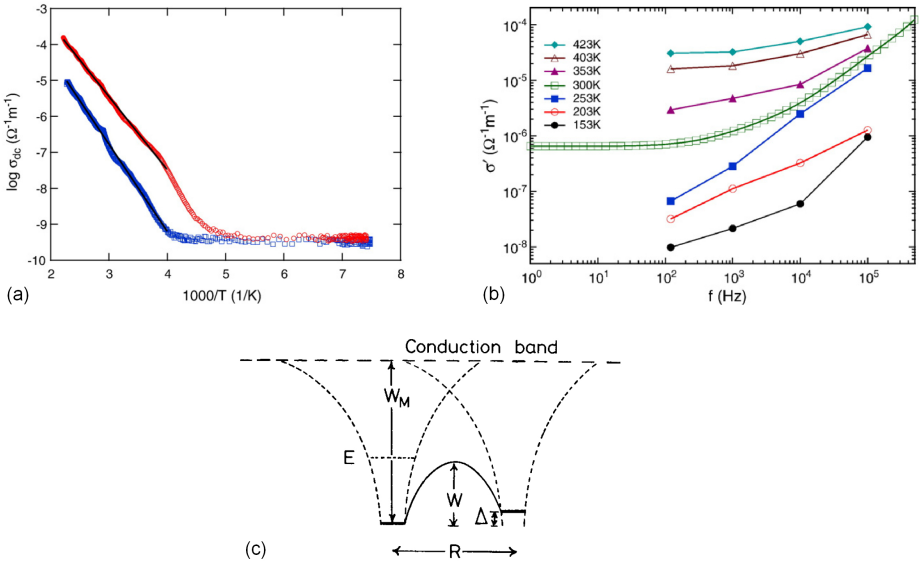

Figure 2.14: (a) The temperature dependence of the DC conductivity of a $3\mu m$ and $8\mu m$ thick NiO film represented by red circles and blue squares respectively [103]. (b) The frequency dependence of the real part of the conductivity of a a $3\mu m$ thick NiO film at the indicated temperatures [103]. (c) An illustration of the lowering of the barrier height for electrons in the case of two closely spaced charged centers in the CBH model [46].

$$\sigma(\omega) \sim \omega^s, \tag{2.8}$$

with the frequency exponent s

$$s = 1 - \frac{6k_BT}{W_M - k_BT\ln(\frac{1}{\omega\tau_0})}. \tag{2.9}$$

The *temperature dependence* of the conductivity in the narrow-band limit ($\Delta_0 \ll k_BT$) is given as [46, 100]

$$\sigma \sim T^n, \tag{2.10}$$

with the temperature exponent n

$$n = (1-s)\ln(\frac{1}{\omega\tau_0}). \tag{2.11}$$

2.2.4 Point defect chemistry

The quality of the specimen is the keystone in experimental investigations of solid state physics, especially for such structure sensitive properties as transport phenomena. In the early stages, experiments on electrical conduction of NiO were carried out on sintered polycrystals. Since NiO crystallizes as described in chapter 2.2.1 in the cubic NaCl structure for $T > 250°C$, no anisotropy is expected in the conductivity. However, the effects of grain boundaries cannot be ignored. Besides mismatching of atomic arrays, the local composition in many cases can become quite different from that of the bulk crystal [180].

Many transition metal oxides have a finite composition width, as shown in the phase diagram of NiO in figure 2.15. Such compounds are called *Berthollides* in contrast to the *Daltonides*, which only exhibit stoichiometric compositions [116]. The composition of a Berthollide-oxide can be controlled by the oxygen partial pressure in the surrounding atmosphere.

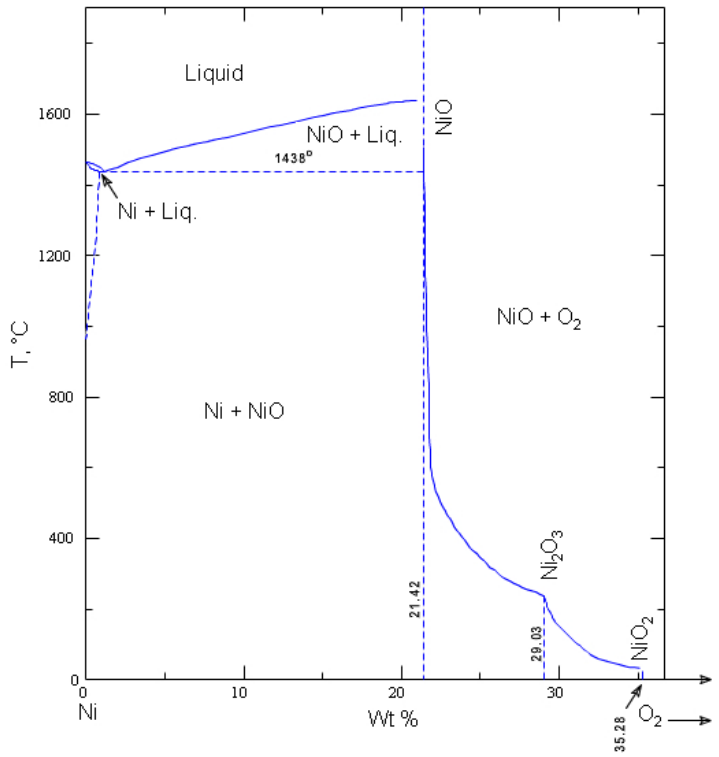

Figure 2.15: Part of the phase diagram of the Ni-O_2 system [21].

The oxidation or reduction of the specimens starts at the surface or at grain

boundaries. For a change of composition inside the crystal grains, atomic diffusion is necessary. In the case of oxidation, either anions enter from the surface or cations migrate to the surface or to grain boundaries. Since the diffusion rates decrease exponentially with decreasing temperature, the composition at boundaries can differ from that in the interior, after the specimens are cooled down or annealed at lower temperatures. Hence, *Wittenauer* and *van Zandt* postulated even in single crystals the existence of a low-resistance surface layer and pointed out the possibility that such a surface layer had a large effect on the transport properties of the highly-resistive NiO [180].

The density of the charge carriers is determined by the deviation of the composition from stoichiometry. For a quantitative discussion, the precise composition should be determined as a function of the *oxygen partial pressure* $p(O_2)$ and *temperature* T. At high temperatures $T > 900°C$ NiO equilibriates relatively fast with the surrounding atmosphere. Changing the ambient oxygen partial pressure therefore involves a change in the composition, as shown in figure 2.16.

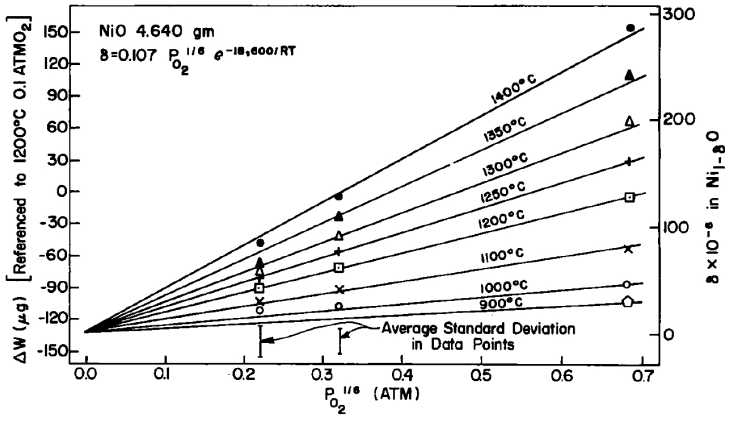

Figure 2.16: The composition of NiO as a function of the oxygen partial pressure and as determined temperature by thermogravimetric measurements [128]. δ represents the deficiency of Ni and can be expressed as $Ni_{1-\delta}O$.

Taking into account the fact that the self-diffusion coefficient of nickel in NiO [157, 34, 50] is significantly larger than the oxygen self-diffusion coefficient [127], it may be assumed that the conductivity in NiO is mainly dominated by defects in the Ni sublattice. The formation of defects in NiO based on this assumption can be described in the *Kröger-Vink notation* [88, 87] by the following chemical reactions [69]

$$Ni_{Ni}^{\times} + V_i^{\times} \rightleftharpoons Ni_i^{\times} + V_{Ni}^{\times} \tag{2.12}$$

$$\frac{1}{2}O_2(g) \rightleftharpoons V_{Ni}^{\times} + O_O^{\times} \tag{2.13}$$

where $Ni_{Ni}^{\times}$ is a neutral, octahedral nickel atom, $V_{Ni}^{\times}$ is a neutral, octahedral nickel vacancy, $V_i^{\times}$ is a tetrahedral interstitial vacancy and $Ni_i^{\times}$ is a nickel atom in a tetrahedral interstitial position. Interstitial nickel atoms and the two vacancies created in these processes may give a complex [139], according to the following reaction

$$Ni_i^{\times} + 2V_{Ni}^{\times} \rightleftharpoons (V_{Ni}Ni_iV_{Ni})^{\times} \equiv Ni_C^{\times} \tag{2.14}$$

The nickel vacancies can be singly or doubly ionized according to the reactions

$$V_{Ni}^{\times} \rightleftharpoons V_{Ni}^{'} + h^{\bullet} \tag{2.15}$$

$$V_{Ni}^{'} \rightleftharpoons V_{Ni}^{''} + h^{\bullet} \tag{2.16}$$

The energy levels owing to interstitial nickel atoms should be energetically placed higher in the forbidden bands than the acceptor levels caused by nickel vacancies and the concentration of the interstitial atoms should not be larger than that of the nickel vacancies over the whole range of oxygen pressure, according to reactions (2.12) and (2.13). All interstitial nickel atoms can be assumed to be doubly ionized according to the reaction

$$Ni_i^{\times} \rightleftharpoons Ni_i^{\bullet\bullet} + 2e^{'} \tag{2.17}$$

The suggested complex in equation (2.14) ionizes as follows

$$Ni_C^{\times} \rightleftharpoons (V_{Ni}^{''}Ni_i^{\bullet\bullet\bullet}V_{Ni}^{''})^{'} + h^{\bullet} \equiv Ni_C^{'} + h^{\bullet} \tag{2.18}$$

where $Ni_i^{\bullet\bullet\bullet}$ is a triply ionized interstitial nickel atom. For the electronic defects the following reaction holds

$$zero \rightleftharpoons e^{'} + h^{\bullet} \tag{2.19}$$

Applying the law of mass action to reactions (2.12) to (2.19) and using the neutrality condition expressed by

$$p + 2[Ni_i^{\bullet\bullet}] = n + [V_{Ni}^{'}] + 2[V_{Ni}^{''}], \tag{2.20}$$

one can finally obtain the following expressions [69]

$$[Ni_i^{\bullet\bullet}] \cdot [V_{Ni}^{''}] = \frac{K_1 K_2 K_3 K_F}{K_i^2} \equiv K_F^{''} \tag{2.21}$$

$$[V_{Ni}^{'}] \cdot p = K_1 \cdot K_V \cdot p(O_2)^{\frac{1}{2}} \tag{2.22}$$

$$[V_{Ni}^{''}] \cdot p^2 = K_1 \cdot K_2 \cdot K_V \cdot p(O_2)^{\frac{1}{2}} \tag{2.23}$$

$$[Ni_C^{'}] \cdot p = K_4 \cdot K_C \cdot K_F \cdot K_V \cdot p(O_2)^{\frac{1}{2}} \tag{2.24}$$

where $[k]$ is the concentration of species k, K_i is the equilibrium constant for the concerning reaction, p is the concentration of holes and $p(O_2)$ is the oxygen partial pressure.

At very *low oxygen partial pressures* Frenkel type defects should predominate (equation (2.12)) because the number of vacancies created in reaction (2.13) is very small under these conditions. The neutrality condition can therefore be written as

$$[Ni_i^{\bullet\bullet}] \cong [V_{Ni}^{''}] \tag{2.25}$$

in this oxygen pressure range.

In the *intermediate range of oxygen partial pressure*, the concentration of holes increases with $p(O_2)$ according to equation (2.23). In this range the simplified neutrality condition can therefor be written as

$$2[V_{Ni}^{''}] \cong p \tag{2.26}$$

For the *high oxygen pressure range* finally, either singly ionized nickel vacancies or singly ionized $Ni_C^{'}$ complexes predominate. In the first case a simplified neutrality condition is given by

$$[V_{Ni}^{'}] \cong p \tag{2.27}$$

and in the second case by

$$[Ni_C^{'}] \cong p \tag{2.28}$$

The resulting expressions for the concentrations of all defects considered here as a function of $p(O_2)$ for these four neutrality conditions are summarized in table 2.1.

Defect	Range I: $[V_{Ni}^{''}] = [Ni_i^{\bullet\bullet}]$	Range II: $2[V_{Ni}^{''}] = p$	Range IIIa: $[V_{Ni}^{'}] = p$	Range IIIb: $[Ni_C^{'}] = p$
p	$\frac{(K_1K_2K_V)^{\frac{1}{2}}}{(K_F^{''})^{\frac{1}{4}}}p(O_2)^{\frac{1}{4}}$	$(2K_1K_2K_V)^{\frac{1}{3}}p(O_2)^{\frac{1}{6}}$	$(K_1K_V)^{\frac{1}{2}}p(O_2)^{\frac{1}{4}}$	$(K_4K_CK_FK_V)^{\frac{1}{2}}p(O_2)^{\frac{1}{4}}$
$[V_{Ni}^{''}]$	$(K_F^{''})\frac{1}{2}$	$(\frac{K_1K_2K_V}{4})^{\frac{1}{3}}p(O_2)^{\frac{1}{6}}$	K_2	$\frac{K_1K_2}{K_4K_CK_F}$
$[Ni_i^{\bullet\bullet}]$	$(K_F^{''})^{\frac{1}{2}}$	$\frac{4^{\frac{1}{3}}K_F^{''}}{(K_1K_2K_V)^{\frac{1}{3}}}p(O_2)^{-\frac{1}{6}}$	$\frac{K_F^{''}}{K_2}$	$\frac{K_4K_CK_VK_F^{''}}{K_1K_2}$
$[V_{Ni}^{'}]$	$\frac{(K_1K_V)^{\frac{1}{2}}(K_F^{''})^{\frac{1}{4}}}{K_2^{\frac{1}{2}}}p(O_2)^{\frac{1}{4}}$	$\frac{(K_1K_V)^{\frac{2}{3}}}{(2K_2)^{\frac{1}{3}}}p(O_2)^{\frac{1}{3}}$	$(K_1K_V)^{\frac{1}{2}}p(O_2)^{\frac{1}{4}}$	$K_1(\frac{K_V}{K_4K_CK_F})^{\frac{1}{2}}p(O_2)^{\frac{1}{4}}$
$[Ni_C^{'}]$	$\frac{K_4K_CK_F(K_V)^{\frac{1}{2}}(K_F^{''})^{\frac{1}{4}}}{(K_1K_2)^{\frac{1}{2}}}p(O_2)^{\frac{1}{4}}$	$\frac{K_4K_CK_F(K_V)^{\frac{2}{3}}}{(2K_1K_2)^{\frac{1}{3}}}p(O_2)^{\frac{1}{3}}$	$\frac{K_4K_CK_F(K_V)^{\frac{1}{2}}}{K_1^{\frac{1}{2}}}p(O_2)^{\frac{1}{4}}$	$(K_4K_CK_FK_V)^{\frac{1}{2}}p(O_2)^{\frac{1}{4}}$

Table 2.1: Expressions for the concentrations of defects in NiO in equilibrium with the ambient oxygen environment for various approximations of the neutrality condition [69].

To represent the expressions given in table 2.1 graphically the method proposed by *Brouwer* [26] and *Kröger and Vink* [88] is used. With this method one can represent the concentrations of the various types of defects as a function of the oxygen partial pressure $p(O_2)$ over the whole range of oxygen pressure in a double-logarithmic graph. These isotherms for the concentration of various defects in NiO are shown in figure 2.17.

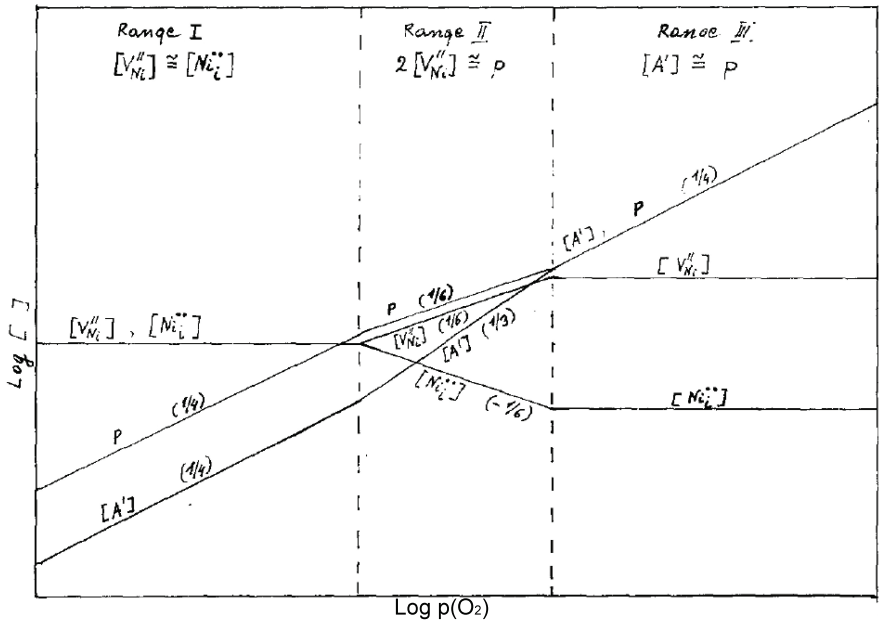

Figure 2.17: Concentrations [] of various defects in NiO as a function of the oxygen pressure at constant temperature [69]. $[A^{'}] \equiv [V^{'}_{Ni}]$ or $[A^{'}] \equiv [Ni^{'}_{C}]$.

Numerous experiments have been performed to prove the above sketched point defect model [25, 37, 47, 173, 128]. Figure 2.18 shows the dependence of the conductivity on the oxygen partial pressure. The slope indicated in the figure is equal to approximately $\frac{1}{4}$ for high temperatures $950°C < T < 1200°C$ and high oxygen partial pressures 10^{-4} atm$< p(O_2) < 1$ atm. This supports the model for Range III, i.e., either $Ni^{'}_{C}$ complexes or singly ionized nickel vacancies predominate, create holes and are therefore the dominant defects.

Fueki and Wagner [50] determined the self-diffusion coefficient D_{Ni} of nickel in NiO as a function of the oxygen pressure for high temperatures in the range $1000°C < T < 1400°C$. These data indicate that D_{Ni} is independent of the oxygen partial pressure at pressures lower than about $10^{-6}atm$ as shown in figure 2.19. Additionally, the results of electrical measurements performed by *Bransky and Tallan* [25] support the above described model for the low oxygen pressure Range I.

Results on single crystalline as well as on polycrystalline NiO are reported that

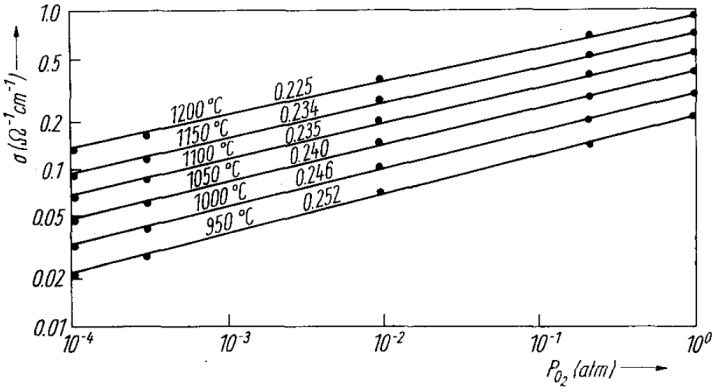

Figure 2.18: Oxygen partial pressure dependence of the electrical conductivity in NiO [47].

indicate a $\frac{1}{6}$ dependence of the log of the conductivity on the log of the $p(O_2)$ at high temperatures [128]. This supports the model in Range II, where doubly ionized nickel vacancies are the predominant defects responsible for the creation of holes and thereby for the conductivity.

Another point is the origin of the activated temperature dependence of the electrical conductivity. Is this due to a temperature dependent *carrier density* or to a temperature dependent *mobility* of the charge carriers or to both? To clarify this question *Bosman* and *Crevecoer* [22] performed *Seebeck* measurements on a $8.8 \cdot 10^{-2}$ at.% Li doped NiO polycrystal.

Figure 2.20 shows the resistivity and the thermoelectric power as a function of the reciprocal temperature. Apparently, the natural logarithm of the resistivity and of the thermoelectric power normalized by $2.3\frac{k_B}{e}$ show the same slope above $170K$. The thermoelectric power can be expressed by [22]

$$\alpha = 2.3\frac{k_B}{e}\log(\frac{N_c e^A}{p}). \tag{2.29}$$

provided that the minority electronic carrier can be ignored. Here, N_c is the effective density of states, A is a constant determined by the dominant scattering process and p is the carrier density.

The resistivity ρ can be expressed by

$$\rho = \frac{1}{pe\mu}, \tag{2.30}$$

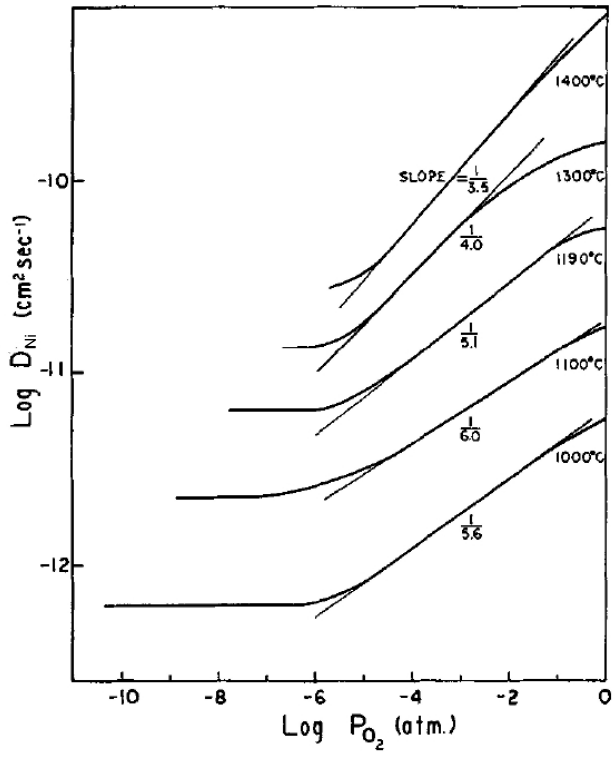

Figure 2.19: The self-diffusion coefficient D_{Ni} of nickel in NiO as a function of oxygen pressure at various temperatures, according to *Fueki and Wagner* [50].

where p is the number of holes, e is the elementary charge and μ is the mobility of the holes.

If we compare $\alpha = 2.3\frac{k_B}{e}\log(\frac{N_c e^A}{p})$ and $\log\rho = \frac{1}{pe\mu}$ we see that the temperature dependence of α is determined by that of p if N_c and A are constant, and the temperature dependence of ρ by that of p and μ. This equation indicates that $\frac{\alpha}{2.3\cdot(k_B/e)}$ is equal to $\log\rho + const.$ if the temperature dependence of the mobility is negligible. This can be clearly seen in figure 2.20. By this reasoning, *Bosman* and *Crevecoer* claimed that figure 2.20 is proof of an almost constant mobility and temperature dependent carrier density for temperatures 170 K $< T <$ 1000 K. The conductivity at high temperatures $T >$ 1000 K should than become relatively independent of temperature because almost all the holes are thermally excited from the traps, which can be seen in figure 2.20 as well. According to this model, the mobility of the carriers can be calculated from the carrier density, estimated, for example, from the quantity of the doped Li. According to *Bosman*

et al. [22], the mobility is about $\mu = 4 \cdot 10^{-5}$ $m^2V^{-1}s^{-1}$ at $T = 1200K$. For sputtered NiO films similar values are found at room temperature [32].

The here found almost *constant mobility* and *temperature dependent carrier density* (band like conduction due to thermally activated large polarons) for temperatures 170 K $< T <$ 1000 K in NiO does not contradict the earlier presented correlated barrier hopping (CBR) model. The CBR model in which the conduction in NiO is explained by *thermal excitation of the mobility* (small polaron hopping) is found for temperatures $T <$ 200 K [101].

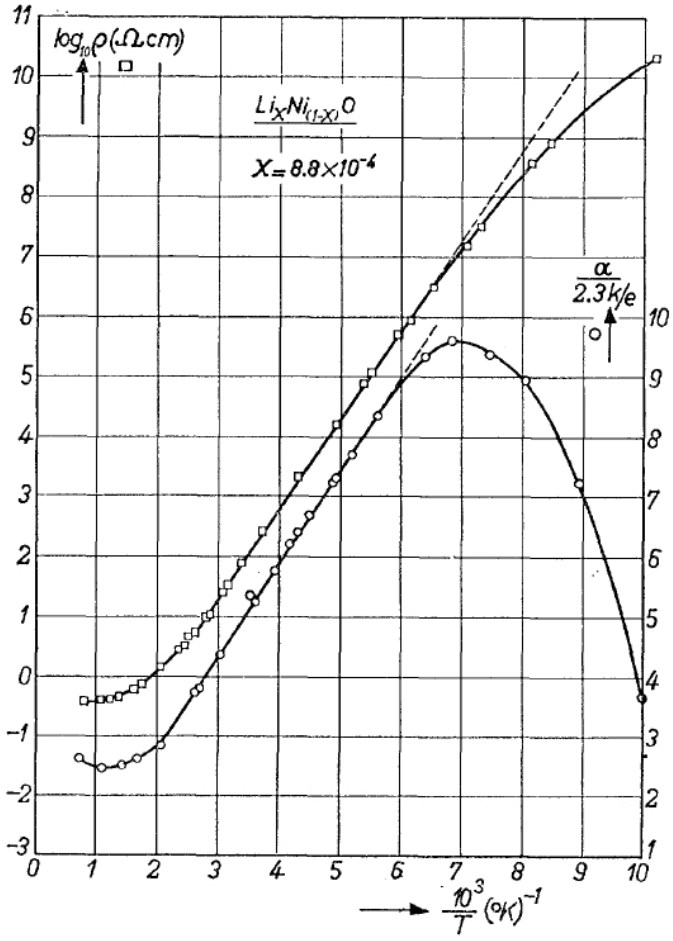

Figure 2.20: Resistivity and thermoelectric power as a function of reciprocal temperature for NiO doped with $8.8 \cdot 10^{-2}$ at.% Li. Above $170K$ the temperature dependence of $\log_{10} \rho$ is practically identical to that of $\frac{\alpha}{2.3(\frac{k_B}{e})}$, indicating that their common origin is the variation in charge carrier concentration [22].

3 Methods

In this chapter the experimental methods used to fabricate and characterize the resistive switching NiO devices are described. First, the radio frequency and direct current sputter deposition technique used for the preparation of the metallic electrodes, as well as the NiO thin films are described. Then, various techniques like X-ray diffraction, Rutherford backscattering spectroscopy, X-ray photoelectron spectroscopy, transmission electron microscopy, scanning electron microscopy and atomic force microscopy, used for the physical characterization of the devices, are briefly discussed. Finally, the techniques used for the electrical characterization are specified.

3.1 Sputter deposition

For the deposition of the NiO films, as well as for the Ti adhesion layers and Pt electrodes, sputter deposition techniques are used.

For the deposition of pure metals, e.g. Ni, Ti or Pt, the *direct current* (DC) sputtering technique is utilized. In this method, a constant high acceleration voltage is applied between the metallic target and the grounded sample substrate, to ignite the plasma in the surrounding Ar sputtering gas. The positive Ar ions are accelerated towards the target. Owing to the bombardment, atoms are ejected from the target material by energy and momentum transfer, which deposit on the sample substrate [126].

To obtain oxidized films, e.g. NiO_x, oxygen gas is added to the Ar sputtering gas, to oxidize the metal, e.g., Ni, during the sputtering process (*reactive sputtering*). By tuning the oxygen partial pressure $p(O_2)$ the stoichiometry of the deposited oxide can be tuned [126].

To deposit oxidic films, e.g. NiO films, using a oxidic target, e.g. a NiO target, the DC sputtering technique cannot be used, because of the buildup of a positive surface charge on the target, which would repel the positively charged Ar ions. In this case the *radio frequency* (RF) sputtering technique is used, where a

alternating electrical field is applied between target and grounded substrate. When the RF frequency is high enough ($\gtrsim$ 50 kHz) only the electrons in the plasma can follow the RF field and the ions cannot any more, because of their higher mass to charge ratio. Therefore, the electrons oscillate in the plasma and ionize the Ar atoms.

Because of the disparity in electron and ion mobility a large initial electron current is drawn during the positive half of the cycle of the RF signal applied to the target. However, only a small ion current flows during the second half of the cycle. This would enable a net current averaged over a complete cycle to be different from zero. But because the target is insulating no charge can be transferred. Therefore, the operating point of the plasma potential is shifted to a negative voltage, the *DC target bias*, and no net current flows. The DC target bias causes a net acceleration of the positive Ar ions towards the target. Owing to the bombardment, atoms are ejected from the target material which deposit on the sample substrate, like in the case of DC sputtering [126].

To realize RF sputtering, a high-frequency generator is connected in series with a matchbox and the plasma. The matchbox is necessary to decouple RF and the DC parts and to maintain the electrical neutrality of the plasma. For efficient sputtering the area of the target should be small compared with the total area of the grounded substrate stage, baseplates and chamber walls to raise the target sheath potential while minimizing ion bombardment of grounded fixtures [126].

Additionally, *magnetrons* can be placed behind the target. In magnetrons, electrons do not even reach the anode but are trapped onto cycloidal trajectories near the target, enhancing the ionization efficiency there. This is accomplished by employing a magnetic field oriented parallel to the target and perpendicular to the electric field. Practically, this is achieved by placing bar magnets with a suitable orientation behind the target (*magnetron sputtering*) [126].

In this study a Leybold Univex 450C sputtering system is used, as shown in figure 3.1. This system is built up as a cluster comprised of six separate sputter chambers, with different targets, which can be operated in either the DC or RF mode. One chamber is used as load lock. Samples can be transferred by a robot arm from one chamber to another. This enables the sputtering of stacks of different films on a sample, without breaking the vacuum.

3.2 X-Ray Diffraction

To investigate the structural properties of the thin films, X-ray diffraction (XRD) is performed. It offers, for example, information about the crystal structure, the lattice parameter, orientation or crystallinity. In this study a Philips PW 3020 diffractometer with a Cu X-ray tube is used. A XRD measurement on thin film samples gives a diffraction pattern, where the peaks can be assigned to the lattice planes of the crystal structure according to Bragg's law [126]

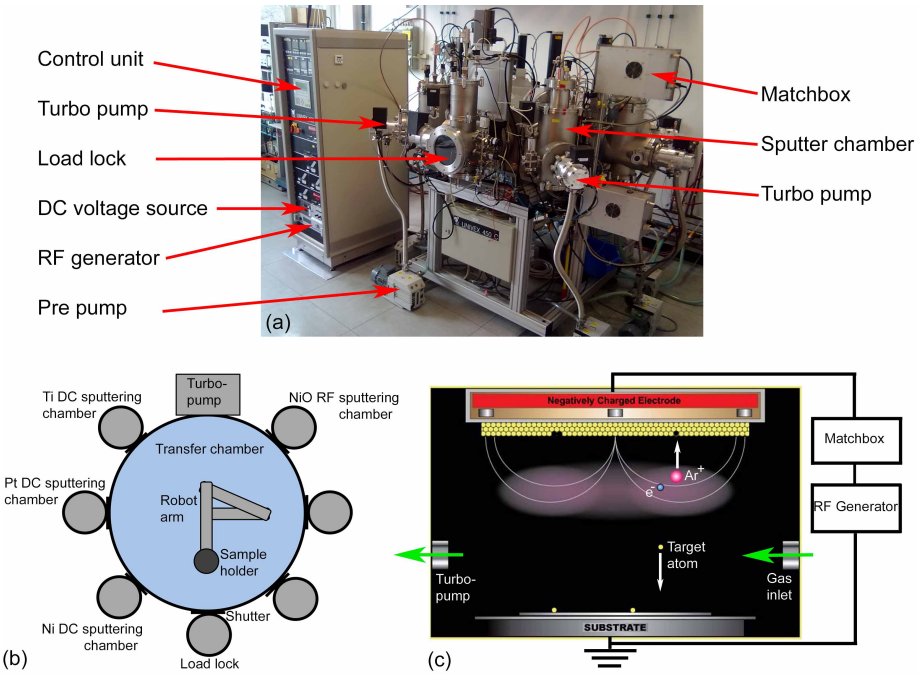

Figure 3.1: (a) Photograph of the Leybold Univex 450C sputter cluster tool. (b) Schematic layout of the sputtertool. (c) Schematic of a RF magnetron sputtering process.

$$n\lambda = 2d_{hkl}\sin(\theta), \tag{3.1}$$

where λ is the wavelength, d_{hkl} the distance of two neighbored lattice planes with the Miller indices (hkl), θ the diffraction angle and n the order of the diffracted beam. The lattice constants a, b and c can be calculated from the peak position by

$$d_{hkl} = \frac{1}{\sqrt{\frac{h^2}{a^2} + \frac{k^2}{b^2} + \frac{l^2}{c^2}}}, \tag{3.2}$$

Because the films investigated in this work are polycrystalline and very thin, the ratio of the intensity of the Bragg reflections originating from the film to the intensity of the Bragg reflections originating from the substrate is very low. The generally used θ-2θ-scan method does not deliver the required intensity to allow a clear identification of the diffraction peaks. Therefore, the *grazing incidence* X-ray diffraction (GID or GIXD) method is used (see figure 3.2(a)). This method typically uses a fixed small incident angle (here $\omega = 2°$) for the incoming X-ray beam, so that diffraction is made surface sensitive by limiting

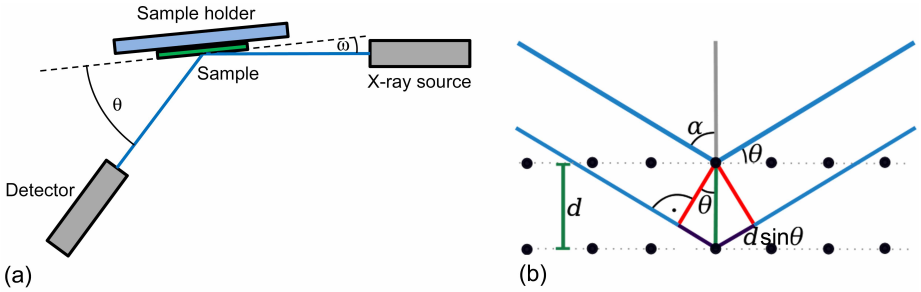

Figure 3.2: (a) Schematic of the Philips PW 3020 diffractometer in the grazing incidence geometry. (b) Schematic of the geometric condition for Bragg reflection.

the wave penetration depth. In this way, the path length of the incident beam through the film is increased and thus the diffracting volume of the film for higher 2θ angles. The background signal of the substrate is minimized and the diffracted radiation stems to a larger extent from the NiO layer. During the measurement only 2θ is changed. To identify the diffraction peaks the measured diffractograms are compared with the reference powder diffractograms from the *International Centre for Diffraction Data* (ICDD).

3.3 Rutherford Backscattering Spectrometry

Rutherford backscattering spectroscopy (RBS) is based on the *elastic, hard-sphere collision* between a high kinetic energy particle from an incident beam and a stationary particle located in the sample. According to the conservation of energy and momentum, the energy of the backscattered ions E_1 depends on the mass of the ions itself M_0 of the mass of the atoms from which they are scattered M as well as on the scattering angle ϑ [126]

$$E_1 = \left(\frac{M_0 \cos\vartheta + \sqrt{M^2 - M_0^2 \sin^2\vartheta}}{M_0^2 + M^2} \right)^2 \cdot E_0. \tag{3.3}$$

Here, E_0 is the energy of the incident beam ions and ϑ the scattering angle of the backscattered ions in the laboratory frame of reference.

When the impinging ion is not scattered from the surface of the sample but inside the bulk, additionally the ions lose their energy on their way through the sample by electronic excitation and ionization of target atoms. These *inelastic scattering* events are so numerous that the energy loss can be considered to be continuous with depth.

The number of inelastic interactions is a statistical process and results in a Gaussian energy distribution. This is called *energy straggling* and causes a widening of the otherwise sharp peaks in the backscattered energy spectrum.

In practice, for a given measurement angle, nuclei of different elements will scatter incident ions to different degrees and with different energies. This produces separate peaks on a plot of backscattered intensity versus backscattered energy. The elements in the specimen are then identified by the positions of the peaks in the energy spectrum. From the width and shifted position of these peaks the depth distribution of the elements is determined. The peak heights give the relative concentration.

In the experiment performed in this work, the sample was bombarded with a high-energy ion beam of He^+ ions of 1.4 MeV with a beam dose of 50 $\mu C/cm^2$. The energy distribution and the yield of the backscattered He^+ ions at an angle of 170° was recorded with a detector with 10 keV energy resolution. To avoid *blocking* and *channeling* effects, the sample was tilted under a small angle from the normal direction and was rotated during the measurements [61].

3.4 X-Ray Photoelectron Spectroscopy

X-ray photoelectron spectroscopy (XPS) is based on the photoelectric effect, which describes the ejection of electrons from a surface when photons impinge upon it. The XPS technique is highly surface specific due to the short mean free path of the photoelectrons inside the material before they are excited from the solid. The kinetic energy (E_k) of the photoelectrons leaving the sample are determined using a concentric hemispherical analyzer (CHA) [174].

A CHA consists of two metal hemispheres, that are arranged in such a way, that their centers of curvature are coincident. Different voltages are placed on each hemisphere such that the electrons injected into the gap between the hemispheres are deflected by the electric field between the two hemispheres. If the electrons are traveling very fast, they will impinge on the outer hemisphere, if they are traveling very slow, they will be attracted to the inner hemisphere. Therefore, only electrons in a narrow energy window succeed in getting all the way round the hemispheres to the detector. In front of the CHA, a lens system is placed, which slow down the electrons in order to be detected, from which the kinetic energy (E_k) of the detected photoelectrons is deduced [174].

This gives a XPS spectrum with a series of photoelectron peaks. The binding energy of the peaks are characteristic for each chemical element. The peak areas are used to determine the relative amount of the chemical elements in the materials surface. The shape of each peak and the binding energy can be slightly altered by the chemical state of the emitting atom. Therefore, XPS also provides information about chemical bonding as well. XPS can detect all other elements, except hydrogen and helium.

3.5 Transmission Electron Microscopy

Transmission electron microscopy (TEM) is used to obtain structural information from specimens that are thin enough to transmit electrons. The resolution of a TEM is much higher than that of optical microscopes because of the shorter de Broglie wavelength of electrons.

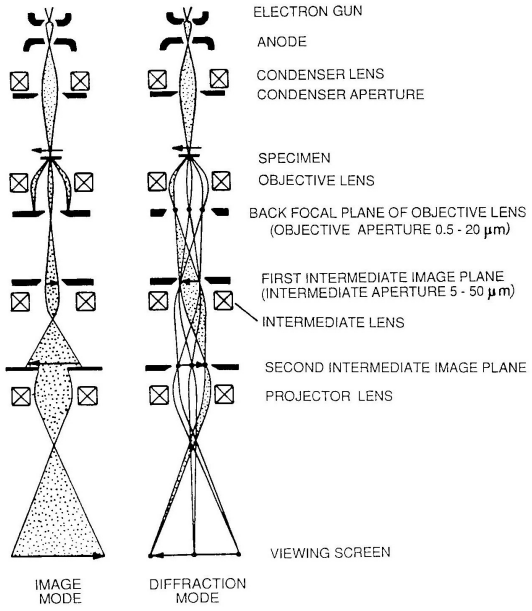

Figure 3.3: Schematic of the path of the electrons in a TEM in the image and diffraction mode [126].

Figure 3.3 shows a simplified schematic of the used Philips CEM200 TEM. The electrons provided by the electron source (200 kV in this study) are deflected by the the capacitor lens system in such a way that the sample is illuminated uniformly and the trajectories of the electrons are parallel to each other and perpendicular to the samples surface. In the sample the electrons are diffracted, mostly by Rutherford diffraction. Therefore, the higher the atomic number and the lower the acceleration voltage, the thinner the sample has to be (see chapter 3.3). Partially also inelastic interaction between beam and matrix electrons at heterogeneities, e.g., grain boundaries, dislocations, second-phase particles, defects, cause complex absorption and scattering effects, leading to a spatial variation in the intensity of the transmitted beam [126].

Electrons that are scattered elastically and exit the sample under the same angle are focussed into one point in the back focal plane of the objective lens. In the *image mode*, an aperture is placed in the focal plane letting pass only the non scattered electrons. Thicker regions in the sample, as well as atoms

with higher atomic number will scatter more electrons and will therefore be darker in the resulting image in the image planes. In this way, in the case of amorphous samples a simple analysis of the acquired image is possible. This is called the *bright field image*. The projector lens system magnifies this image onto a detector, like a fluorescent screen or a CCD sensor [126].

In the case of crystalline samples, additionally the Bragg diffraction has to be taken into account (see chapter 3.2). In this case the electrons disperse into discrete locations in the back focal plane. By blocking the central beam and adjusting the magnetic lenses such that the back focal plane of the lens rather than the imaging plane is placed on the imaging apparatus a diffraction pattern can be generated. This is called the *diffraction mode* of the TEM. The acquired image is known as *dark field image* and allows the identification of the crystallographic structure of the sample [126].

3.6 Scanning Electron Microscopy

A scanning electron microscope (SEM) is a type of electron microscope that provides a magnified (about 10 to more than 500000 times) image of a sample by scanning it with a beam of electrons in a raster scan pattern. With SEM information about the sample's surface topography and composition can be obtained.

A simplified schematic of a SEM is shown in figure 3.4(a). The electron beam is generated in the electron source. Here, electrons are thermionically emitted from a tungsten cathode filament. In more expensive SEM's often a field emission gun is used. In this case the electrons tunnel out of the sharp tip of the gun by applying a very high electrical field. The electrons are then accelerated in an electric field of typically up to 30 kV. Thereafter, one or two condenser lenses focus the electron beam to a diameter of about a nanometer. The beam then passes through the deflection coils which deflect the beam so that it rasters over a rectangular area of the sample surface. Upon impinging on the specimen, the primary electrons decelerate by energy transfer to atomic electrons and the lattice. Through continuous random scattering events, the primary beam effectively spreads and fills a teardrop-shaped interaction volume with a multitude of electronic excitations (see figure 3.4(b)). The energy spectrum of the electrons that manage to leave the specimen is shown schematically in figure 3.4(c). By the correlation of the intensity and the location of the signal coming from the sample surface an image of the surface can be generated. The *magnification* is determined by the ratio of the size of the scanned surface to the size of the image screen.

In the most commonly used mode of the in this study used Hitachi S4100 SEM, the intensity of the *secondary electrons* created by the inelastic interaction of the electron beam with atoms in the sample surface is analysed. Because of their low energy of typically a few eV (see figure 3.4(c)) they originate from the

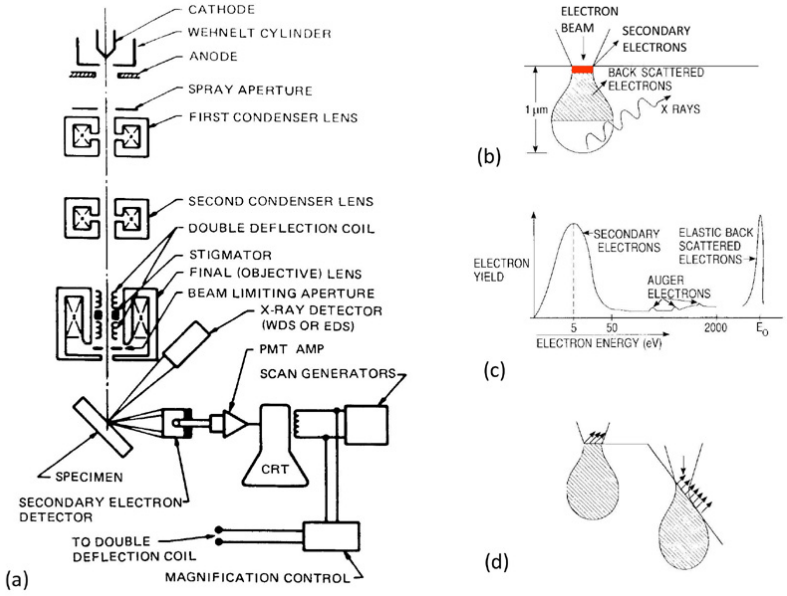

Figure 3.4: (a) Schematic diagram of a SEM. (b) Electron and photon signals emanating from tear-shaped interaction volume during electron-beam impingement on specimen surface. (c) Energy spectrum of electrons emitted from specimen surface. (d) Effect of surface topography on electron emission [126].

upper few nanometers of the sample. They therefore image the *topography* of the surface. Areas that face the detector, as well as ridges appear brighter on the CRT than averted and shadowed areas (see figure 3.4(d)) [126].

In another mode the elastically *backscattered electrons* are detected, which typically have energies of a few keV. Therefore they originate from deeper layers in the sample. The probability of backscattering increases with the atomic number Z of the material. Therefore, heavy elements backscatter more electrons than lighter elements and appear brighter on the CRT screen. Therefore, in this mode a *material contrast* image is obtained, which enables an analysis of the chemical composition of the sample surface. On the other hand, the backscattered fraction is not a very strong function of Z. Elemental identification is therefore not feasible from such information. Since the escape depth for high-energy backscattered electrons is much greater than for low-energy secondary electrons, there is much less topological contrast in these images [126].

By the high energetic electrons of the primary electron beam also *X-rays* characteristic of atoms in the irradiated area are emitted. By an analysis of their energies, the atoms can be identified and by a count of the number of X-rays emitted the concentration of atoms in the specimen can be determined. This technique is called X-ray energy dispersive analysis (*EDX*) [126].

3.7 Atomic Force Microscopy

To determine the topography, roughness and lateral grain sizes on the surface of the samples, a SIS Picostation atomic force microscope (AFM) is used. In general an AFM consists of a sharp tip (typically some tens of nm) mounted on a elastically flexible arm, called *cantilever*. The tip is rastered over a rectangular area of the sample surface, while it interacts with the sample surface by a rich variety of attractive forces like van der Waals forces for distances greater than about 1 nm between tip and sample surface. For smaller distances, repulsive forces like Pauli repulsion between the electron shells of atoms in the tip and the surface atoms take the leading role. The sum of all these forces is described by the *Lennard-Jones potential* [42]. Meanwhile, the excitation of the tip is determined by the deflection of a laser beam on the cantilever (see figure 3.5(a)). In the simplest case, the deflected laser beam is detected by a two-sector diode, which determines the excitation of the cantilever θ by comparison of the intensity of the laser beam detected in the upper with the lower part of the two-sector diode [176].

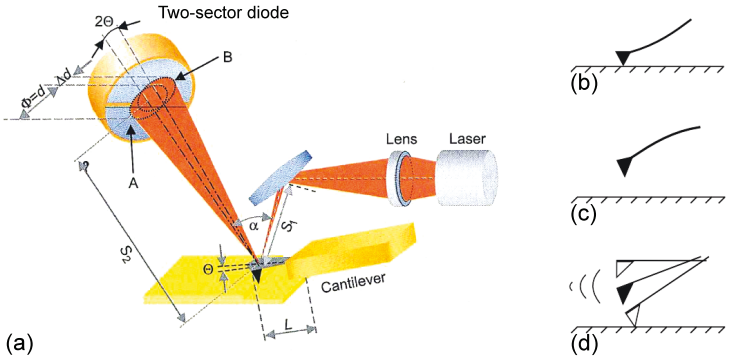

Figure 3.5: Schematic diagram of a AFM [176].

Generally, an AFM can be operated in 3 different modes. The simplest is the *contact mode* (figure 3.5(b)), where the tip makes mechanical contact to the surface and follows the topography because of Coulomb repulsion of the electron shells.

A second, less straining mode is the *non-contact mode* (figure 3.5(c)). Here, the tip of the cantilever is positioned in the attractive, van der Waals dominated range of the Lennard-Jones potential. A control circuit excites the cantilever, while keeping it always in its resonance frequency. The interaction between the tip and surface changes the resonance frequency. The frequency-shift when resonance is maintained, or the phase-shift when the frequency is kept constant, is a measure for the magnitude of the interaction and therefore the distance

between tip and surface. This mode is used under vacuum conditions and can achieve down to atomic resolution [176].

The SIS Picostation used in this work was operated in air and in the intermittent contact mode, or *tapping mode* (see figure 3.5(d)). In this mode the cantilever is excited near its resonance frequency. The interaction between the tip and sample surface changes the resonance frequency, which changes the amplitude and phase relatively to the stimulation. A control circuit keeps the amplitude constant, by adjusting the distance and therefore also the interaction between tip and surface. This "correction" is used to image the topography of the sample surface. Depending on the roughness of the surface, a resolution of 1 nm to 10 nm is possible [176].

3.8 Electrical characterization

The electrical characterization of the MIM-devices are mainly performed using three different techniques. They are briefly discussed in the following paragraphs.

3.8.1 Quasistatic I(V) and static I(t) measurement setup

Most forming and resistive switching characteristics are measured with a commercially available Agilent B1500A semiconductor analyzer, which is equipped with four source measurement units (SMU). Because a two point measurement is adequate to characterize a two terminal device, in general only two of the SMU's are used. Typically the voltage was swept in a quasi-static manner from 0 V $\rightarrow$ V$_{max}$ $\rightarrow$ 0 V or 0 V $\rightarrow$ V$_{min}$ $\rightarrow$ 0 V.

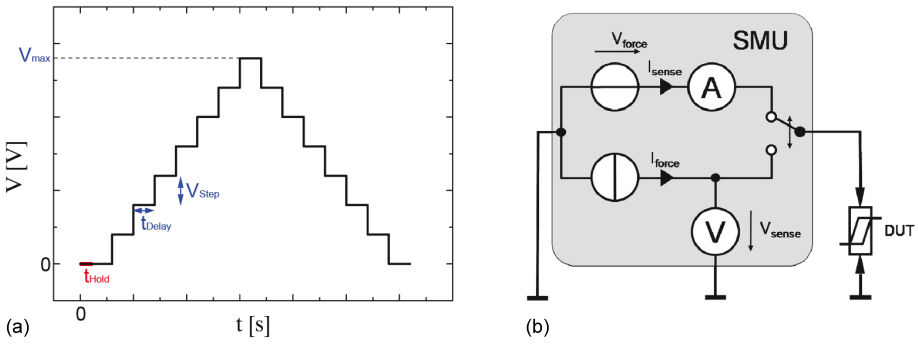

Figure 3.6: (a) Characteristics of a voltage sweep. (b) Schematic of a two terminal measurement showing a simplified circuit diagram of a SMU. The second SMU works as ground in this case.

Figure 3.6(a) shows a schematic of a quasistatic I(V) measurement. The semiconductor analyzer increases the voltage by a preset voltage step and waits a defined time (delay time) until a steady state is reached. At this point, the current is recorded. Afterwards the next voltage step takes place. The step size as well as the delay time can be varied, arbitrarily. Additionally, a hold time can be set, after which the analyzer starts the measurement. A current compliance is set to prevent permanent breakdown of the devices. For the potentiostatic measurements the voltage is set to the required value and the current is measured simultaneously. The maximum number of data points is 10000 for the Agilent B1500A, which requires an adjustment of the delay time for long time measurements.

The samples are placed on a chuck inside a darkbox made by SÜSS MicroTec, which shields the samples and contact needles against light and other external electromagnetic influences. The chuck is automatically movable and is controlled by the semiconductor analyzer. This enables the systematic measurement of a sequence of many devices, which is of great benefit for statistical measurements as they were performed in this work. To enable measurements at elevated temperatures the chuck can be heated from room temperature up to 200°C.

3.8.2 Impedance spectroscopy

Impedance spectroscopy analyzes the complex ratio of the voltage to its current response in an alternating current (AC) circuit. This enables to acquire more information about the electrical properties of the devices, compared to the simple resistance measurements by DC methods. It additionally enables to acquire information about the electrostatic storage of charges, induced by voltages between the electrodes (*capacitance*), and about the induction of voltages in the devices, self-induced by the magnetic fields of currents (*inductance*) [102]. The impedance caused by these two effects is referred to as *reactance* X and forms the imaginary part of the complex impedance Z, whereas the resistance R forms the real part. In cartesian form Z can be expressed as

$$Z = R + iX, \tag{3.4}$$

with magnitude

$$|Z| = \sqrt{R^2 + X^2}. \tag{3.5}$$

In the polar form the complex impedance Z is given by

$$Z = |Z| \cdot e^{i\phi}, \tag{3.6}$$

where ϕ gives the phase difference between the AC voltage and AC current answer.

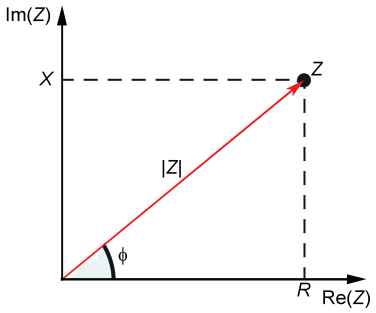

Figure 3.7: A graphical representation of the complex impedance plane

For the measurements performed in this work a Solatron Si1260 impedance / gain-phase analyzer is used. The measurements are performed at frequencies starting from 10 MHz to 1 Hz. The excitation amplitude was chosen to the small value of 50 mV, to guarantee a linear response of the device under test. Afterwards, the measured data is fitted by using the ZView program.

3.8.3 Electrical characterization under different ambient gas conditions

One of the possible mechanisms behind the resistive switching behaviour of oxides is the reduction and oxidation of the oxide by exchange of oxygen with the ambient atmosphere. Therefore, a specially designed vacuum setup (base pressure $p \approx 10^{-9}$ mbar) is used (see figure 3.8) in which forming and switching procedures are performed under different ambient gas conditions. In this work, vacuum, standard atmospheric air and conditions with increased oxygen- or water partial pressure are performed and compared with each other. Additionally the sample holder can be heated from room temperature up to temperatures of about 400°C. The quasistatic voltage sweeps as well as the potentiostatic measurements on the devices are performed using a Keithley 236 Source meter.

To investigate NiO layers without electrodes the setup shown in figure 3.9 is used. To measure the resistivity of the NiO films two leads are contacted to the film by silver paste. Because no contact needles are required a glass tube is used in stead of the vacuum chamber used for the resistive switching devices (see figure 3.8). The advantage is a much smaller volume to evacuate which results in a base pressure of down to 10^{-10} mbar. To investigate the influence of different ambient atmospheres on the NiO layers, different gasses can be let into the glass tube. The temperature can be regulated by the heater, which can be slided over the glass tube. The temperature of the sample is measured with a thermocouple (see figure 3.9(a)).

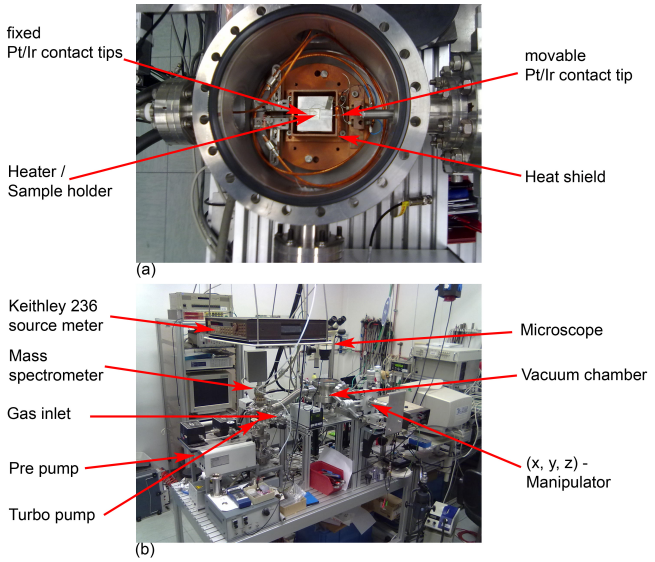

Figure 3.8: (a) Detailed view of the vacuum chamber and (b) a overview of the measurement setup for the electrical characterization of devices under different ambient gas conditions.

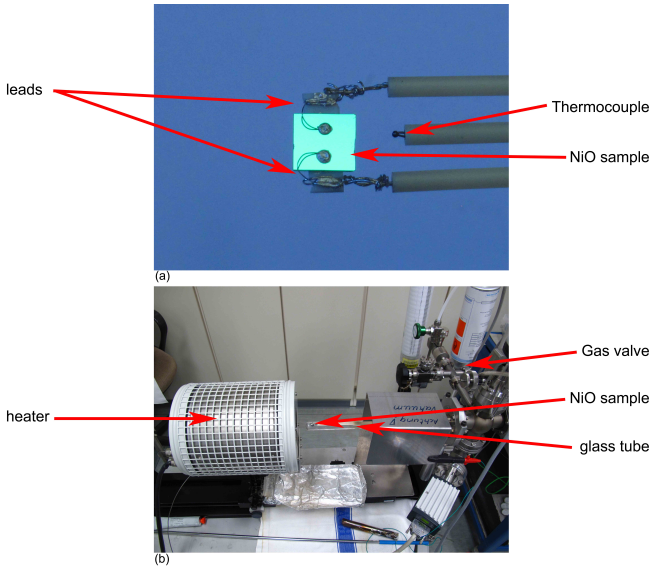

Figure 3.9: (a) Detailed view of the contacted sample and (b) a overview of the measurement setup for the electrical characterization of NiO layers under different ambient gas conditions and temperatures.

4

Sample Preparation

This chapter deals with the fabrication of the three different designs of resistive switching memory devices used in this work. To investigate the potential integration of ReRAM into CMOS and the related required performance of NiO-based memory devices, devices with several nanometer sized tungsten plugs (common in industry) were used as bottom electrodes. The drawback of these devices for basic research is the fact, that the tungsten plugs will inevitably oxidize during the subsequent NiO deposition. Therefore, effects of this extra oxide layer on the resistive switching properties can not be excluded.

To elucidate and avoid these effects nano crossbar structures with platinum bottom and top electrodes were fabricated. These are made of 100 nm wide bottom platinum lines and 100 nm wide top platinum lines, that overlay each other in a resulting active cell area of 100 nm by 100 nm.

To investigate the scaling properties, devices with planar platinum bottom electrode and square platinum top electrodes were fabricated. The thickness of the active NiO layer is thereby varied from 25 nm to 300 nm while the top electrode sizes reach from 50 μm by 50μm to 600 μm by 600 μm.

4.1 Plug devices

To investigate the potential integration into CMOS, our project partner *Qimonda AG* delivered wafers with prefabricated tungsten bottom electrode plugs and contact pads, as shown in figure 4.1. After cleaning the sample with acetone and propanol, the wafer was shortly etched in a Reactive Ion Beam Etching (RIBE) system (Oxford Ionfab 300 plus) using Ar as etching gas to remove a native tungsten oxide layer on the tungsten bottom plug. Subsequently, a NiO layer of $d = 50$nm thicknesses and a 50nm Pt top electrode layer are deposited sequentially, without interrupting the vacuum conditions. For this, the Leybold Univex 450C magnetron sputtering system described in chapter 3.1 is used. The deposition of the NiO layer is performed by DC reactive sputtering from a nickel target using an Ar/O_2 mixture as sputtering gas. The DC reactive sputtering

mode enables a controlled variation of the oxygen content in the deposited NiO film by controlling the Ar/O_2 ratio of the sputter gas. The sputter power is kept constant at $P = 300$ W and the deposition time is adapted in order to achieve 50nm NiO film thickness. All plug devices were deposited at room temperature. The exact Ar/O_2 ratio used are different from experiment to experiment and will be mentioned on the spot (see chapter 4.3). The 50 nm Pt top electrodes are deposited by DC sputtering from a Pt target with $P = 375$ W sputtering power and an ambient Ar gas pressure of $p = 1,5 \cdot 10^{-2}$ mbar.

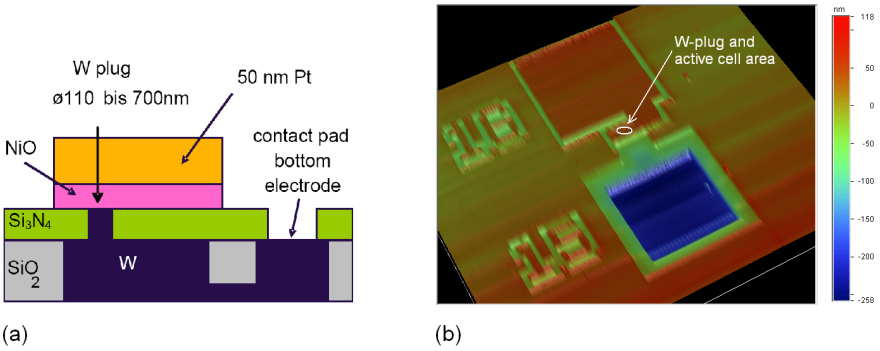

Figure 4.1: (a) The prefabricated Wafer as delivered by our project partner, with the structured NiO active layer and platinum top electrode. Subsequently, the bottom contact pad is opened (b) A profilometric scan of a MIM structure showing the top electrode (red) and opened bottom electrode contact pad (blue). The color scale indicates the height in nanometers. The tungsten bottom plug and the active memory area are located as marked.

Next, the Pt top electrodes and the underlying NiO layer are galvanically insolated from the rest of the layers by optical lithography and subsequent RIBE using Argon as etching gas under an incidence angle of 45°. Finally the contact pads to access the bottom tungsten plugs are opened by a second optical lithography step, followed by the corresponding RIBE step, again using Argon as etching gas, but this time under an incidence angle of 90°.

4.2 Nano crossbar devices

The nano crossbar devices were fabricated without oxidizable electrode materials. Therefore, a Si (100) wafer with 400 nm thermally grown silicon oxide is used as substrate. Then, a 5 nm Ti adhesion layer and a 30nm Pt layer are deposited using DC sputtering. A sputter power of $P = 300$ W and $P = 375$ W under an ambient Ar gas pressure of $p = 2.3 \cdot 10^{-2}$ mbar and $p = 1.5 \cdot 10^{-2}$ mbar

are used for the Ti adhesion layer and the Pt bottom electrode layer, respectively. The 100 nm wide Pt bottom lines and the contact pads are subsequently patterned by Nano Imprint Lithography (NIL).

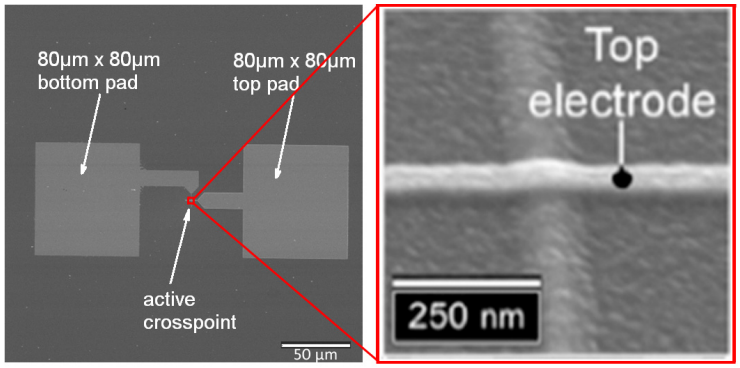

Figure 4.2: (a) A SEM image of a single nano crossbar structure and the contact pads. On the left one can see the bottom electrode, on the right side the top electrode structure. (b) A magnified SEM image of the area where the 100 nm wide bottom electrode line and the 100 nm wide top electrode line cross each other, taken at an angle of $45°$. This area defines the 100 nm $\times$ 100 nm active memory cell.

Then, a NiO layer of varying thicknesses between 25 nm and 300 nm is deposited at room temperature by RF sputtering from a stoichiometric NiO target, with a sputtering power of $P = 98$ W and an Ar partial gas pressure of $p = 1.4 \cdot 10^{-2}$ mbar using the sputtering system described in chapter 3.1. Subsequently, the 100 nm wide top electrode lines and the contact pads are defined by electron beam lithography. After that, a 5 nm nickel adhesion layer and a 30 nm platinum top electrode layer are deposited using thermal evaporation. The top electrodes are then structured using a lift off process in acetone. It turned out, that the lift off process does not work when the Ni and Pt top electrode layers are deposited by sputtering. Probably, the e-beam resist is not as robust against the high energy input involved in sputter deposition compared with thermal evaporation. Therefore, thermal evaporation was chosen here for top electrode deposition.

Finally, optical lithography and a corresponding RIBE step with Ar as etching gas under an incident angle of $90°$ are used to etch the NiO layer and open the bottom contact pads.

4.3 Micro devices

To investigate the scaling properties of the resistive switching behavior in NiO thin films, structures in the micro meter range were fabricated. The benefit of structures in this size range is that the top Pt electrodes can be sputtered, because of the use of optical resist. Therefore, no nickel adhesion layer is needed between the NiO film and the Pt top electrodes, whereby possible effects on the switching properties related to the nickel adhesion layer used in the nano crossbar structures are disposed.

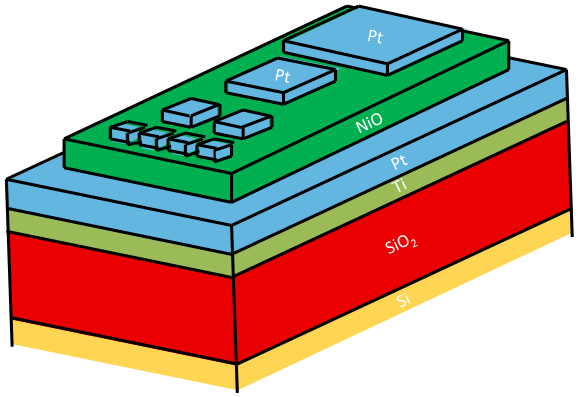

Figure 4.3: A schematic of the micro devices. The Pt top electrode sizes are varied between 50 μm $\times$ 50 μm and 600 μm $\times$ 600 μm.

As substrate, again a Si (100) wafer with 400 nm thermally grown oxide is used. Subsequently, a 5 nm Ti adhesion layer and a 30 nm Pt layer are deposited by DC sputtering, using the same sputter parameters as in the case of the nano crossbar devices. The Pt bottom electrode is afterwards patterned by standard optical lithography and a subsequent RIBE step using Ar as etching gas at an incident angle of 90°. Thereafter, NiO layers of varying thicknesses between 25 nm and 300 nm are deposited at room temperature by RF sputtering from a stoichiometric NiO target, with a sputtering power of $P = 98$ W and an Ar partial gas pressure of $p = 1.4 \cdot 10^{-2}$ mbar. The exact thickness used for a particular experiment will be mentioned on the spot (see chapter 5.4). To pattern the Pt top electrodes standard optical lithography is used, followed by the Pt deposition. The 30 nm Pt top electrodes were deposited by DC sputtering

with Ar gas, using $P = 375$ W sputter power and an ambient Ar gas pressure of $p = 1.5 \cdot 10^{-2}$ mbar. A following lift off process in acetone completes the pattering of the top electrodes. To open the bottom contact pads, a standard optical lithography step followed by the corresponding RIBE, using Ar at an incident angle of 90° is used to finalize the device.

4.4 TEM devices

For TEM analysis, only very thin films in the nanometer range can be investigated because the electrons have to be able to pass through the sample in order to be detected at the other side of the sample. Therefore, a 300 μm thick Si (100) wafer with a 200 nm thick amorphous Si_3N_4 layer on top is used as a substrate. Then, using the chemical etching agent tetramethylammonium hydroxide (TMAH) the silicon is selectively etched up to the Si_3N_4 layer which is not soluble in TMAH. Using an etch mask, this etching is only done in an area of 0.5 mm width and length. In this way, a Si substrate with a 0.5 mm wide amorphous square Si_3N_4 window is accomplished, see figure 4.4, on which the NiO film is deposited. Because the Si_3N_4 film is amorphous, only diffraction, which originates from the NiO film, will occur.

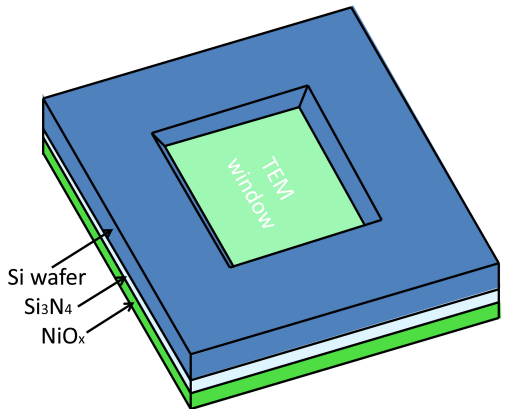

Figure 4.4: Schematic of a TEM window. To enable electron transmission through the sample a special substrate with amorphous Si_3N_4 window is used, which does not produce additional crystalline diffraction.

Finally, using the sputtering system described in chapter 3.1, a 50 nm NiO_x film is sputtered at room temperature onto the TEM substrate by RF sputtering from a stoichiometric NiO target. The Ar partial gas pressure was $p = 1.4 \cdot 10^{-2}$ mbar and the sputtering power was set to $P = 98$ W.

5

Film and Device Characterization

In this chapter the structural and electrical properties of the pristine films and devices are discussed. First, the influence of different nickel to oxygen ratios on the resistance of these NiO films is investigated and analyzed on the base of the point defect chemistry concepts. To study the morphology and crystal structure of the NiO films used for resistive switching, X-ray diffraction (XRD) measurements are performed. To verify the scaling properties of resistive switching devices using NiO, the morphological and electrical behaviour of NiO films of different thicknesses are studied. Finally, the impact of the deposition of the Pt top electrodes on the morphology and stoichiometry of the interface between the Pt and the NiO films is investigated.

5.1 Influence of O content on NiO_x film properties

To investigate the influence of the oxygen content on the structural and electrical properties of the pristine NiO films and devices a series of plug devices (see chapter 4.1) with different compositions are prepared. Hereto, the O_2 flow is varied from 2 to 16 sccm O_2 and the Ar flow is varied from 58 to 44 sccm, respectively, while keeping the total flow rate constant at 60 sccm.

To measure the O/Ni ratio x in these NiO_x films, *Rutherford backscattering spectrometry* (RBS) is used (see chapter 3.3). Figure 5.1(a) shows the RBS spectrum of, e.g., a sample sputtered with a O_2 flow of 6 sccm and a Ar flow of 54 sccm. Every peak or increase of the yield at a certain energy in the spectrum of the backscattered He^+ ions can be addressed to a well defined atomic species in the sample, as described in chapter 3.3. Also the described broadening of the peaks, caused by the energy loss of the scattered He^+ ions on their way back to the surface, can be clearly observed. After inserting the dose of the atomic beam, the effective cross-section of the He^+ ions with the atomic species in the sample and the film thickness, a algorithm fits the measured backscattered energy spectrum, as indicated by the red line in figure 5.1(a). Finally, on the bases of these results, the composition of the films is obtained as shown in

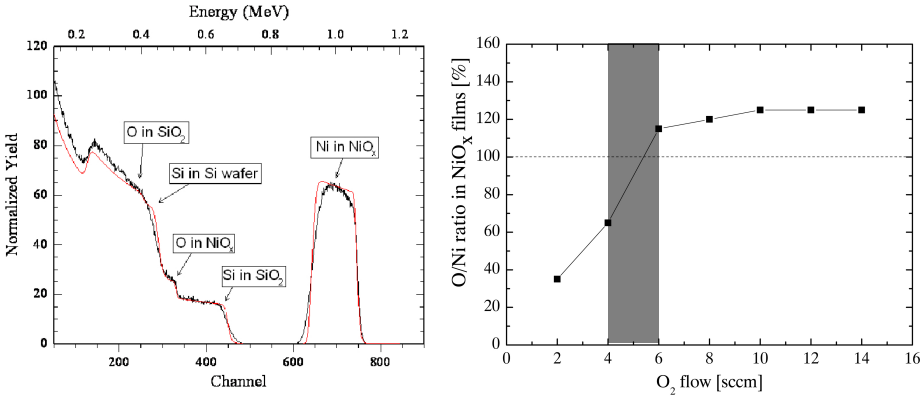

Figure 5.1: (a) A RBS spectrum of a NiO_x film sputtered by DC reactive sputtering using a oxygen flow of 6 sccm, a Ar flow of 54 sccm and a sputter power of $P = 300$ W. A peak or increase of yield at a certain energy corresponds to a specific atomic species in the sample, as indicated by the boxes in the graph. The experimental data (black line) is fitted (red line) to determine the concentration of the specific elements in the sample. (b) The resulting O/Ni ratio in the NiO_x samples in dependence of the O_2 flow during sputtering.

figure 5.1(b).

Apparently, NiO_x films sputtered with more than 10 sccm O_2 in the sputter gas, all have a O/Ni ratio of about 1.25. This is in good agreement with literature that reports a maximum ratio O/Ni=1.3 [53] for stable NiO or even O/Ni=1.44 [2] for NiO thin films sputtered in a pure O_2 atmosphere. The high O/Ni ratio observed in these films can probably be attributed to the formation of Ni_2O_3 (and $Ni(OH)_2$) surface layers [78], because the deposited films exhibit a rather porous structure with a high surface to volume ratio, as discussed later in this chapter. Thus, the measured oxygen concentration of such films can effectively be much higher than stoichiometric NiO, even though the NiO inside the grains below the surface layer will have only minor deviations from the stoichiometric composition.

On the other hand, a mixture between metallic Ni and NiO is easily formed at low O_2 ambient atmospheres [163, 162]. In case the O_2 flow in the sputter gas is $\lesssim 4$ sccm metallic Ni defects probably appear. When the oxygen content in the gas mixture is increased, the density of metallic Ni defects decreases. Stoichiometric NiO would be deposited at an O_2 flow ≈ 5 sccm under the above described sputtering conditions.

To investigate the effect of different oxygen content in the sputtered NiO_x films on the conductivity, the in-plane resistivity (or sheet resistance R_{Sheet}) of the

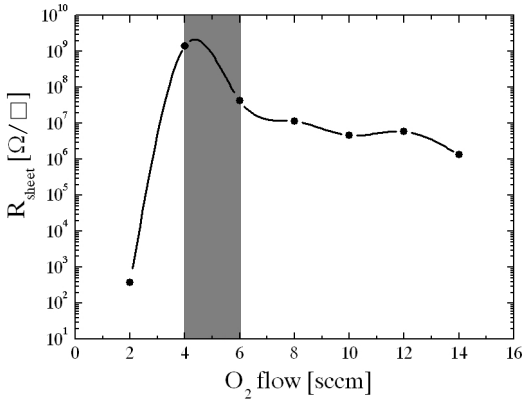

Figure 5.2: Sheet resistance, R_{Sheet}, of NiO_x films sputtered with different O_2/Ar sputter gas ratios. Around the point of stoichiometry R_{Sheet} has a maximum value. When more O is built into the NiO lattice more Ni vacancies and therefore holes are created. The NiO p-type conductivity increases. When less O is built into the NiO lattice below the point of stoichiometry, excess metallic Ni is created and the conductivity rises with decreasing O content.

films are measured using four point probe measurements. Four tungsten needles are contacted onto the film in a linear arrangement with a distance of 1 mm between them. The current I is sourced through the two outer contacts, while the voltage drop U is measured over the two inner contacts. The sheet resistance is then calculated according to

$$R_{Sheet} = \frac{\pi}{\ln 2}\frac{U}{I}. \tag{5.1}$$

The resulting R_{Sheet} as a function of the O_2 flow are shown in figure 5.2. The maximum value of R_{Sheet} is found at an O_2 flow between 4 and 6 sccm. This is in agreement with the O_2 flow needed to deposit nearly stoichiometric films as shown in figure 5.1(b). According to the point defect chemistry model for NiO as described in chapter 2.2.4, an enrichment of O in the NiO lattice leads to an increase of the conductivity due to hole doping by Ni vacancies.

On the other hand, one can expect that a mixture of metallic Ni and NiO is formed at ambient atmospheres with low O_2 pressure [84]. If the amount of Ni increases beyond the point of stoichiometry there is more metallic excess Ni in the NiO_x film which might also increase the conductivity. The maximum value of R_{Sheet} is therefore located around the point of stoichiometry of NiO.

5.1.1 The properties of nearly stoichiometric NiO films

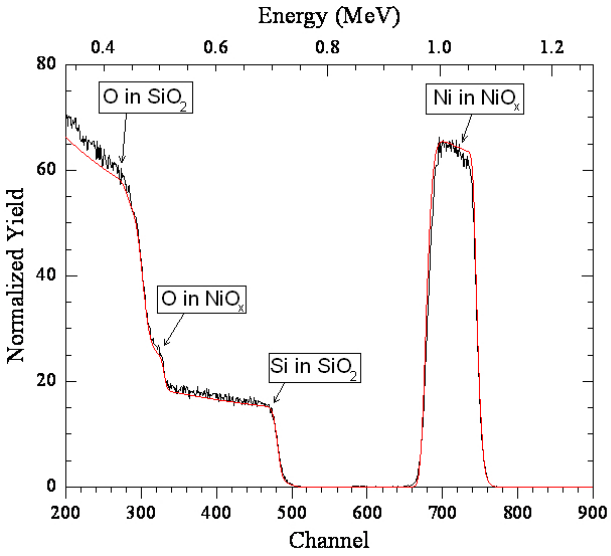

Figure 5.3: A RBS spectrum of a NiO_x film sputtered by RF sputtering from a stoichiometric NiO target using a Ar flow of $60sccm$ and a sputter power of $P = 98W$. A peak or increase of yield at a certain energy corresponds to a specific atomic species in the sample, as indicated by the boxes in the graph. The amount of atoms of a specific species in the sample is revealed by a fit (red line) of the experimental data (black line).

NiO films sputtered with radio frequency (RF) sputtering from a stoichiometric NiO target yield more uniform films in terms of $R_{Pristine}$ and R_{Sheet} on the same wafer as well as in reproducibility from wafer to wafer. Therefore, also samples sputtered by RF sputtering from a NiO target were investigated using Rutherford Backscattering Spectroscopy (RBS). Figure 5.3 shows the RBS spectrum of a micro device as described in chapter 4.3, without Pt top electrodes. The fit (red line) of the experimental data (black line) yields a O/Ni ratio of 1.0 in the NiO film. The films deposited under these conditions can therefore be considered as nearly stoichiometric.

The total number of Ni and O atoms per cm^2 as determined by the fit is found to be $N = 8.7 \cdot 10^{17}$ (Ni+O) atoms/cm^2. With a film thickness of 100 nm one obtains a concentration of $n = 8.7 \cdot 10^{22}$ atoms/cm^3. With the atomic masses of Ni ($58.693u$) and of O ($15.999u$), and assuming the Ni/O ratio to be equal to 1, the apparent density ϱ_{app} of the deposited NiO films can be calculated:

$$\varrho_{app} = 5.4 \frac{g}{cm^3}. \tag{5.2}$$

Compared with the reported value of $\varrho = 6.67 \frac{g}{cm^3}$ for the density of NiO [1], we can conclude that these NiO thin films are quite porous and exhibit many grain boundaries and voids between the grains. This is also supported by the SEM images shown below in chapter 5.4.

5.2 X-ray diffraction

To investigate the crystallographic structure and the preferred orientation of the crystallites of NiO films grown with RF sputtering, *X-ray diffraction* (XRD) measurements are performed. Because the crystallinity of these films is rather low and the irradiated volume of the thin films is very small, the *grazing incident diffraction* (GID) method as described in chapter 3.2 is used. Figure 5.4(a) shows the GID spectrum obtained for a micro device with a 200 nm thick NiO film.

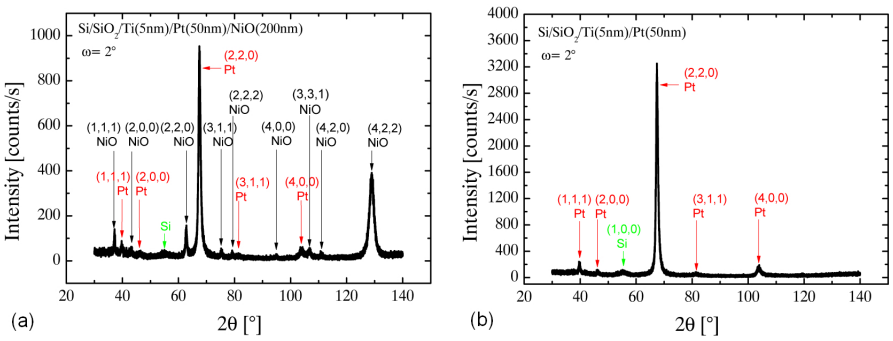

Figure 5.4: (a) A GID spectrum of a 200 nm thick NiO film, sputtered by RF sputtering from a stoichiometric NiO target, deposited on a 50 nm Pt bottom layer, using an oxidized silicon wafer with 400 nm native oxide and a 5 nm Ti adhesion layer on top of it as a substrate. (b) A GID spectrum of the same wafer without the NiO film on top of it. Subtraction of this spectrum from the one shown in (a) gives the spectrum of NiO.

Figure 5.4(b) shows the GID spectrum of the oxidized Si wafer with the Pt film and Ti adhesion layer on top of it, without the NiO film, to clarify the origin of diffraction peaks that do not have their origin in NiO. To identify the diffraction peaks the measured diffractograms are compared with the reference powder diffractograms from the *International Centre for Diffraction Data* (JCPDS). The numbers in figure 5.4(a) and (b) indicate the corresponding Bragg refections

for the particular crystal structure. The outcome of this analysis shows that Pt sputtered on the oxidized Si (100) wafer has a simple cubic structure with a lattice parameter of $a = 0.3923$ nm. The additional peaks that appear in figure 5.4(a) compared with the ones shown in figure 5.4(b) can all be identified to result from cubic NiO with a lattice parameter $a = 0.4177$ nm.

On the other hand, the NiO rhombohedral structure, which represents a distorted cubic structure, would yield almost the same diffractogram apart from the splitting of some Bragg reflections. However, the splitting is so small that it cannot be resolved by the instrument used for the measurements. Therefore, it can also be assumed that the deposited NiO has a *rhombohedral* structure with a lattice parameter $a = 0.2955$ nm, as mentioned in chapter 2.2.1.

5.3 Transmission electron microscopy

Transmission electron microscopy (TEM) is used to gain information about the morphology and structure of the films, e.g., the grain size and the distribution of the grain sizes, the homogeneity of the grains and the lattice constant.

By adjusting the magnetic lenses, discussed in chapter 3.5, such that the back focal plane of the lens rather than the imaging plane is placed on the imaging apparatus a *diffraction pattern* can be generated. For thin crystalline samples, this produces an image that consists of a pattern of dots in the case of a single crystalline, or a series of rings in the case of a polycrystalline material. Figure 5.5(c) shows such an image for a 50 nm NiO_x film sputtered onto the in chapter 4.4 described TEM substrate (see figure 5.5(d)). From this image it is confirmed that the film is polycrystalline, because of the clearly distinguishable diffraction rings with some crystalline spots. By measuring the radius of the rings the distance between the Bragg planes can be calculated by the relation

$$|\vec{g}| = \frac{1}{d_{hkl}}, \tag{5.3}$$

where $|\vec{g}|$ is the reciprocal lattice vector and d_{hkl} the distance between the crystal planes in real space. The calculated d-spacings and the corresponding lattice planes for the orthorhombic and the cubic crystal structure are displayed in the table in figure 5.5. From this analysis, the measured d-spacings would be in line with both the orthorhombic and the cubic crystal structure.

Additionally, if a CCD camera is placed in the imaging plane, one obtains a real image of the morphological features of the thin NiO film. Figure 5.5(a) and (b) show corresponding pictures obtained at a magnification of 100000 and 480000 using an acceleration voltage of 200 kV. The variations in contrast are due to NiO grains with different crystallographic orientation. The grain sizes vary between 10 nm and 30 nm in the film with 50 nm thickness.

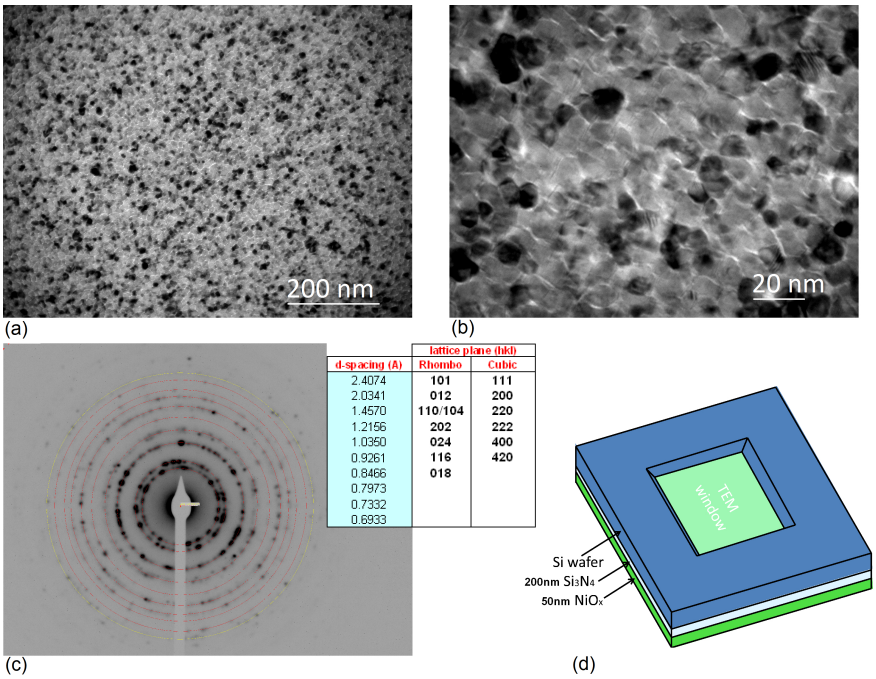

Figure 5.5: TEM images of a 50 nm thick NiO film, deposited on a Si wafer with special Si_3N_4 window for TEM imaging magnified by a factor of 100000 (a) and 480000 (b). Figure (c) shows the TEM diffraction pattern originating from the polycrystalline NiO film. To enable electron transmission through the sample a special substrate with amorphous Si_3N_4 window is used, which does not produce additional crystalline diffraction (d).

5.4 Thickness dependence of NiO film properties

In order to investigate the scaling potential of resistive switching cells, micro devices as described in chapter 4.3 are fabricated, with film thicknesses ranging from 25 nm to 300 nm, by varying the sputter time from $t = 862$ s to $t = 10344$ s, respectively (see figure 5.7).

To determine the morphology of the NiO films SEM and AFM measurements are performed. Figure 5.7(a) shows top view and (b) tilted view SEM images of the NiO films both taken with a magnification factor of 100000 and a acceleration voltage of $V = 10$ kV and $V = 5$ kV, respectively. At film thicknesses of 25 - 50 nm the grain sizes are quite small and a granular structure can be observed. At 100 nm film thickness, the diameter of the grains increases up to about 50 nm and the formation of a columnar structure can be observed. Finally, the

200 nm and 300 nm thick NiO films show a clear columnar structure in the tilted view and the diameter of the grains increases to about 100 nm.

Film thickness [nm]	Maximum Height Difference [nm]	Root Mean Square [nm]
25	3.37	0.39
50	4.14	0.46
100	13.85	1.24
200	22.12	2.38
300	26.83	3.45

Table 5.1: The results of AFM scans on NiO films of different thicknesses.

A more precise determination of the grain sizes and surface roughnesses is possible by AFM measurements as shown by the data in table 5.1. The line scan and 3D projection of 5 μm $\times$ 5 μm AFM measurements on the NiO films which are presented in figure 5.7(c) and (d) support the results from the SEM study that the morphology clearly changes with increasing film thickness. The 25 nm and 50 nm NiO films show very smooth surfaces with a root mean square (RMS) roughness of 0.39 nm and 0.46 nm, respectively. At 100 nm the RMS increases considerably to 1.24 nm which is consistent with a prevailing crystallization into columnar grains. This trend continues when the film thicknesses are above 100 nm.

To investigate the electrical properties of these thin films, the resistances between top and bottom electrodes ($R_{Pristine}$) using micro devices (see chapter 4.3) are measured. These are compared with the sheet resistances (R_{Sheet}) of NiO films directly sputtered on the Si/SiO_2 substrate. To determine the R_{Sheet}, a four point measurement as described in chapter 5.1 is performed. R_{Sheet} is then determined by

$$R_{Sheet} = \frac{\pi}{\ln 2}\frac{U}{I}, \tag{5.4}$$

where I is the sourced current through the two outer contacts and U is the measured voltage between the two inner contacts. The resulting R_{Sheet} as a function of the NiO film thickness are shown in figure 5.6(a). According to

$$R_{Sheet} = \frac{\overline{\rho}_{Sheet}}{d}, \tag{5.5}$$

with $\overline{\rho}_{Sheet}$ the average lateral resistivity of the NiO film and d the film thickness, the R_{Sheet} should scale linearly with the reciprocal thickness of the NiO film.

However, from figure 5.6(a) one can distinguish between three different regions. In the first region up to 100 nm film thickness (blue line) there is indeed a linear dependence, as well as in the third region above 200 nm thick NiO films (green line). In between, there is a transition from one linear dependence into the other linear dependence with increasing reciprocal film thickness.

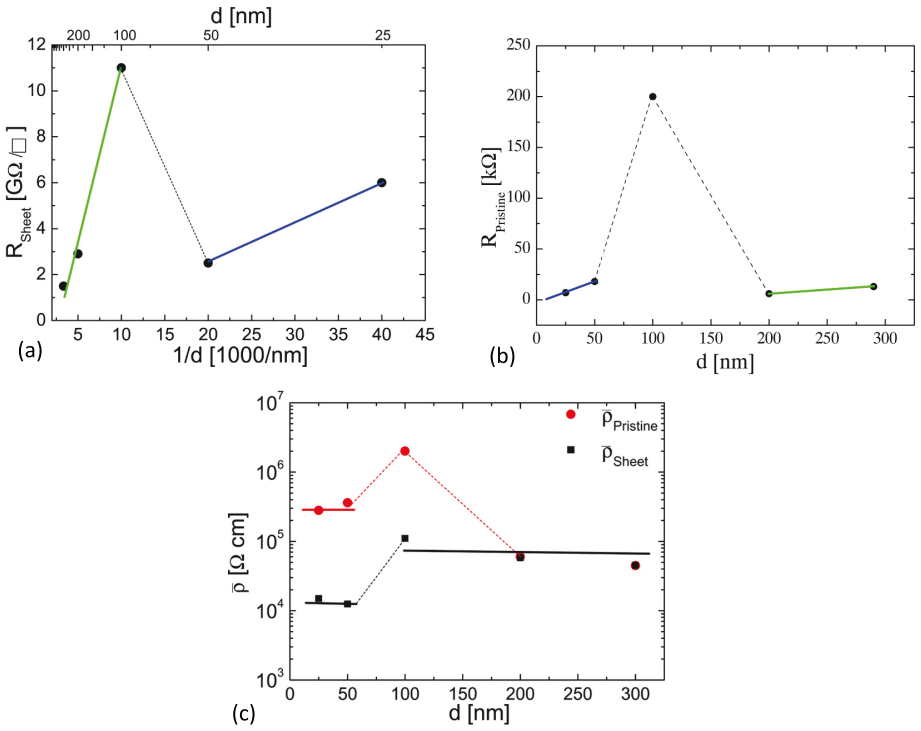

Figure 5.6: (a) The sheet resistance R_{Sheet} as a function of the reciprocal NiO film thickness. (b) The resistance of the pristine device $R_{Pristine}$ as a function of the NiO film thickness. (c) The average resistivity in lateral ($\overline{\rho}_{Sheet}$) and "top to bottom" ($\overline{\rho}_{Pristine}$) direction as a function of the NiO film thickness.

The thickness dependence for the resistance of the micro devices in the pristine state ($R_{Pristine}$), measured between 100 μm $\times$ 100 μm top electrodes and the bottom electrode, should obey

$$R_{Pristine} = \overline{\rho}_{Pristine} \frac{d}{A}, \tag{5.6}$$

with $\overline{\rho}_{Pristine}$ the average "top to bottom" resistivity, d the film thickness and $A = 100$ μm $\times$ 100 μm the pad area. However, also this "top to bottom resistance" shows similar behaviour with increasing NiO film thickness (figure 5.6(b)).

For the thin NiO films up to 50 nm the $R_{Pristine}$ follows the linear dependence as predicted by equation (5.6). Than a steep increase followed by a sharp drop in the $R_{Pristine}$ with increasing thickness is observed. Above a film thickness of 200 nm a linear increase with NiO film thickness can be observed. To get more insight in these dependencies, also the electrical resistivities in the lateral ($\overline{\rho}_{Sheet}$) and in the "top to bottom" direction ($\overline{\rho}_{Pristine}$) are shown in figure 5.6(c).

The behaviour of the lateral resistance R_{Sheet} as well as the "top to bottom" resistance $R_{Pristine}$ can be explained by an increase of crystallinity during the NiO film growth, as reported by the group of *Chen* et al. [33]. A possible scenario is sketched in figure 5.7(e). In very thin films up to 50 nm crystallinity is very poor and the morphology of the films is granular. Therefore, the density of the granular grains is very high and homogeneous. R_{Sheet} and $R_{Pristine}$ follow the linear increase predicted by equations (5.5) and (5.6). $\overline{\rho}_{Sheet}$ as well as $\overline{\rho}_{Pristine}$ are approximately constant, which also is in agreement with a constant density in grains and grain boundaries in lateral as well as "top down" direction.

For film thicknesses between 50 nm and 200 nm, a transition between the granular into columnar grains is observed. Above a film thickness of 200 nm the columnar grains are full-grown and again a linear increase of $R_{initial}$ with increasing film thickness and a linear increase of R_{Sheet} with an increase of the reciprocal film thickness is observed. Also the nearly constant $\overline{\rho}_{Sheet}$ and $\overline{\rho}_{Pristine}$ coincides with this.

The fact that $\overline{\rho}_{Sheet}$ is an order of magnitude smaller than $\overline{\rho}_{Pristine}$ for films below 50 nm may be attributed to the formation of stoichiometric NiO at the NiO-Pt interface induced by the sputtering of the Pt top electrodes in the micro devices used for the $\overline{\rho}_{Pristine}$ measurements. In thicker films the NiO is already crystallized into the columnar crystal structure, which results in almost identical values for $\overline{\rho}_{Sheet}$ and $\overline{\rho}_{Pristine}$ for film thicknesses above 200 nm.

These complicated dependencies of the *lateral resistance* R_{Sheet} as well as the *"top to bottom resistance"* $R_{initial}$ on the film thickness makes it very complicated to investigate the *thickness scaling* of the forming as well as the switching properties of sputtered NiO thin films.

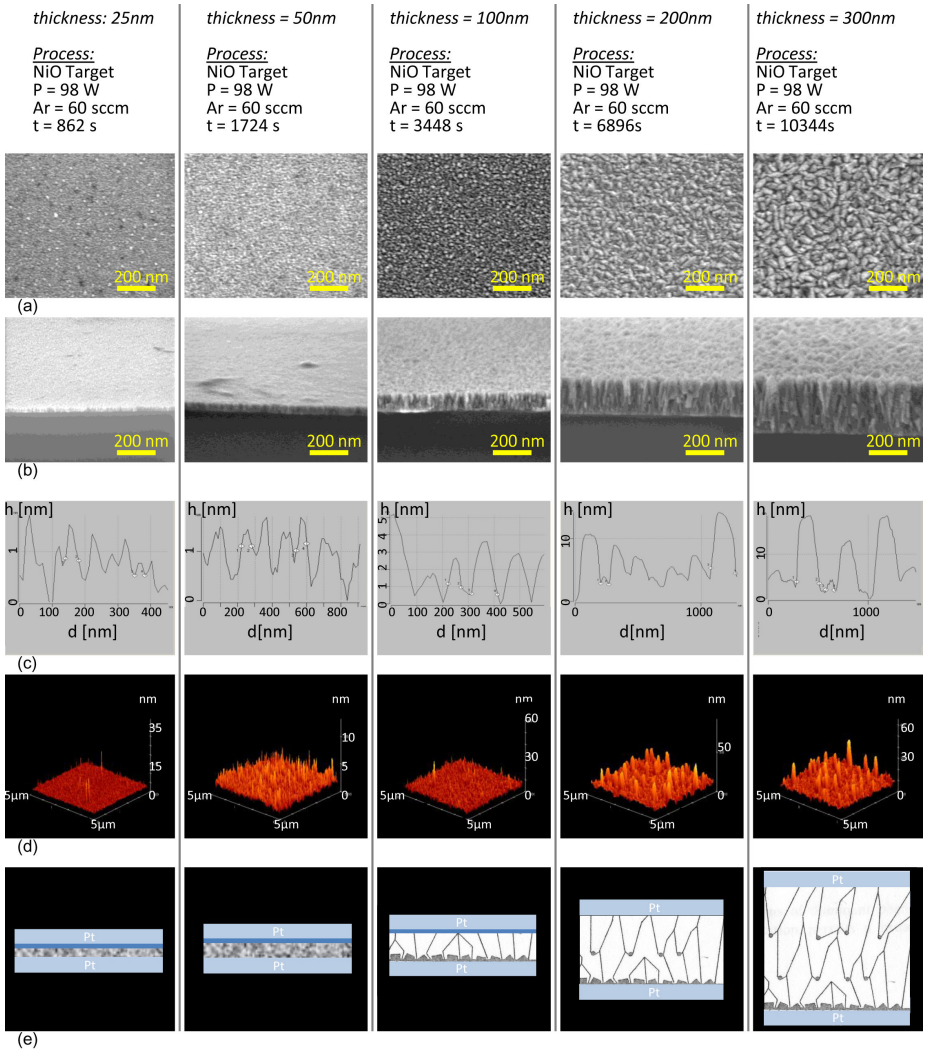

Figure 5.7: (a) Top view and (b) tilted view SEM images showing the formation of the columnar morphology with growing film thickness. (c) Line scans and (d) 3D projection of AFM measurements on NiO films of different thicknesses, showing the morphological changes of the surface during film growth. (e) Schematic representation of the formation of columnar grains in micro devices with increasing film thickness, that can account for the electrical and morphological changes with increasing film thickness [169].

6 Resistive Switching

This chapter attempts to verify the resistive switching behaviour and the associated critical physical quantities and values that trigger the transitions between the pristine state, the LRS and the HRS. Therefore, it is first clarified whether the major voltage drop during voltage stress is at the interfaces between the electrodes and the NiO_x films or across the bulk. This is done by comparison of leakage current measurements with theoretical predictions of models that describe interface- or bulk-limited conduction. To substantiate these results, impedance measurements are performed on devices in LRS, HRS and on pristine devices. Further, the influence of the oxygen content in the NiO_x films on the resistive switching is elucidated, which might have an effect on the local resistance changes during the resistive switching. Finally, the resistive switching behaviour of stoichiometric NiO is investigated more in detail, using quasi-static and fast pulse measurements, with regard to the physical nature and dimensions of the different resistance states, as well as to the performance of the resistive switching devices, e.g. endurance, retention and temperature stability.

6.1 Conduction mechanism

One of the issues that may shed some light on the mechanisms behind the resistive switching phenomena is the understanding of the conduction mechanism of the memory device in the pristine state. To understand, whether the main voltage drop is at the electrode/oxide interface or across the bulk of the oxide film may give a clue for the understanding of the first change of the resistance of the device, commonly named *electroforming*, which turns the capacitor structure into a resistive switching memory device. Therefore, the conductivity of the micro devices described in chapter 4.3 with 100 μm $\times$ 100 μm top electrodes as well as the conductivity of the 100 nm $\times$ 100 nm nano crossbar devices described in chapter 4.2 are measured at different voltages and different temperatures as shown in figure 6.1. The NiO film thickness is 25nm in both cases. The micro as well as the nano devices show both a typical semiconductor

temperature activated conductivity and a symmetric non-linear current-voltage characteristic. This indicates that the interfaces at the bottom and top electrodes are symmetrical and/or that the overall resistance mainly results from the bulk resistivity of the NiO.

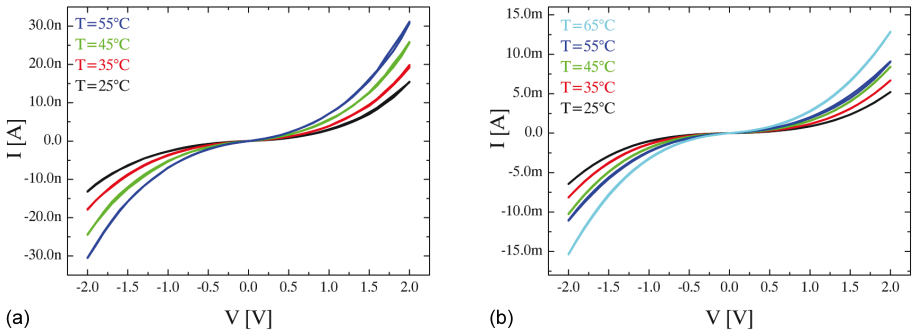

Figure 6.1: Leakage current measurements on pristine 100nm × 100nm nano crossbar devices (a) and on pristine 100μm × 100μm micro devices (b). To investigate the conduction mechanism the conductivity is measured at different voltages and different temperatures.

6.1.1 Interface between electrode and oxide

From an estimation of the energy levels, there should be neither a Schottky barrier at a Pt/NiO nor at a Ni/NiO interface, as shown in figure 6.2. When the metal electrode and the semiconducting NiO are brought into contact charge transfer between the electrode and the semiconductor will prevail until the Fermi levels of the electrode and the semiconductor are aligned to the same height. Depending on the values of the work function of the metal ϕ_m and the energy difference between vacuum and the Fermi level of the semiconductor ϕ_s there can be a blocking, a neutral or an ohmic contact.

The work function ϕ_m for Pt is equal to 5.3 eV [153] and the work function ϕ_s in NiO is equal to 5.0 eV [67, 94]. So in the case of an Pt/NiO contact the work function of the metal exceeds the energy difference between the vacuum and the Fermi level in NiO ($\phi_m > \phi_s$). This implies an accumulation of free carriers, holes in the case of p-type NiO, at and in the vicinity of the contact. Therefore the impedance of the contact should be negligibly small in comparison with the series impedance of the bulk of the NiO and the conduction should be ohmic at low fields. Hence, a Pt/NiO interface should form an *ohmic* contact.

The work function of Ni is equal to 5.0 eV [59, 14]. Therefore, in the case of a Ni/NiO contact, the work function of the metal is equal to the energy difference between the vacuum level and the Fermi level in the semiconductor ($\phi_m = \phi_s$).

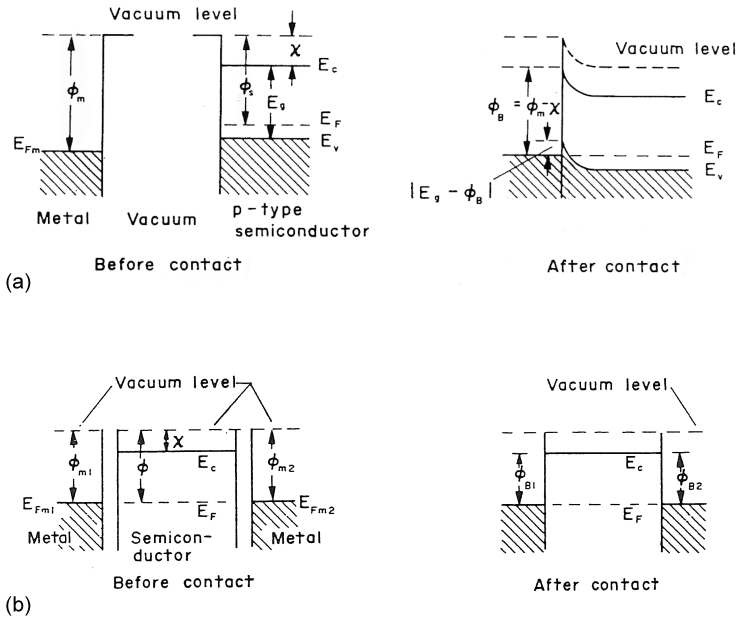

Figure 6.2: (a) Energy level diagrams for a hole ohmic contact between a metal and an extrinsic p-type semiconductor. (b) Energy level diagrams for a neutral contact between a metal and a semiconductor [74].

These kind of contacts are called *neutral*, which implies that the probability for electrons or holes to flow from the metal to the semiconductor is equal to the probability for the charge carriers to flow in the reverse direction. Thus, no space charge region will exist on both sides of the contact, no band bending will be present within the semiconductor and the conduction is ohmic when a d.c. voltage is applied. A condition like this is also referred to as the flat band condition (figure 6.2(b)).

An experimental indication for ohmic contacts in the micro as well as in the nano crossbar devices is the slope of their $\ln(I)$ versus $\ln(V)$ plots. If the contacts are ohmic the IV characteristics should follow the relation

$$I = \frac{V}{R} \Rightarrow \ln(I) = \ln(V) - \ln(R). \tag{6.1}$$

For very low voltages the slopes $\frac{d\ln(I)}{d\ln(V)}$, taken from the IV characteristics shown in figure 6.1 for the micro as well as for the nano crossbar devices, are both close to 1 (1.04 for the nano crossbar devices and 1.07 for the micro devices). Therefore, the contacts in the micro as well as in the nano crossbar devices seem to be ohmic. The voltage drops at the Pt/NiO and Ni/NiO interfaces are

negligible and resistance switching behaviour in these MIM structures with NiO as oxide films is probably not caused by Schottky barrier deformation.

Another strong indication for bulk limited conduction is the linear thickness dependence of the resistance of the pristine samples for thicknesses below 100 nm and above 200 nm, as shown in figure 5.6 in the previous chapter 5.4. Hence, at *low voltages* conductivity is described by the bulk related conduction mechanisms as discussed in chapter 2.2.3. At *higher voltages* additional effects like the *Poole-Frenkel conduction* have to be taken into account.

6.1.2 The Poole-Frenkel effect

The Poole-Frenkel [49] effect results from the lowering of Coulomb potential barriers in the bulk of a material by an applied electric field, as schematically pictured in figure 6.3. Donor sites, acceptor sites, as well as traps experience the Poole-Frenkel effect. For a trap to experience the effect, it must be neutral when filled and charged oppositely to the charge carrier when empty. A trap that is neutral when empty and charged when filled will not experience the effect because of the absence of the Coulomb potential. According to the Poole-Frenkel model [182, 159], when the concentration of donor levels is small compared to the density of acceptor levels (e.g. nickel vacancies) and itinerant holes, the current density j for a p-type semiconductor as a function of the electrical field E and the temperature T is equal to

$$j = \sigma_0 E \, \exp\left[\frac{-q\phi_{PF}}{2k_B T}\right] \, \exp\left[\frac{1}{2k_B T} \cdot \sqrt{\frac{q^3 E}{\pi \varepsilon_0 \varepsilon_r}}\right], \tag{6.2}$$

where ε_0 is the permittivity of free space, ε_r is the high-frequency relative dielectric constant, k_B is the Boltzmann constant, and $\sigma_0 = q\mu\sqrt{N_v N_t}$ is a pre-exponential factor where μ is the mobility of the charge carriers and N_v and N_t represent the density of states at the top of the valence band and the density of traps in the bandgap, respectively. ϕ_{PF} is the energy difference between the emission site and the top of the valence band in the case of p-type semiconductors (see figure 6.3)).

If the conduction is dominated by the Poole-Frenkel mechanism according to equation (6.2), a plot of $\ln(j/V)$ versus $\sqrt{V}$ of the measured IV curves shown in figure 6.1 should result in a straight line for high voltages,

$$\ln(j/V) = \beta_1 \cdot \sqrt{V} + \ln(\alpha_1), AFM \tag{6.3}$$

with a slope β_1

$$\beta_1 = \frac{1}{2k_B T}\sqrt{\frac{q^3}{\pi \varepsilon_0 \varepsilon_r d}}, \tag{6.4}$$

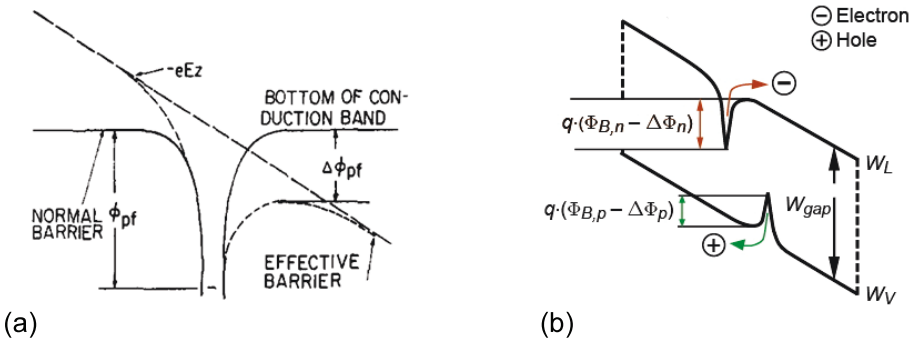

Figure 6.3: (a) Schematic representation of the Poole-Frenkel mechanism for electron conduction, showing the lowering of the Coulomb barrier by an applied electric field E [182]. (b) In a p-type semiconductor the lowering of the barrier for holes in the valence band is significant for the conductivity at high fields [55].

where d is the NiO film thickness. The point of intersection with the axis of ordinate α_1 is equal to

$$\alpha_1 = \frac{\sigma_0}{d} \exp\left[\frac{-q\phi_{PF}}{2k_BT}\right]. \tag{6.5}$$

Figure 6.4 shows $\ln(j/V)$ versus $\sqrt{V}$ plots for the 100 nm $\times$ 100 nm nano crossbar structures (a) and for the micro structures with a pad size of 100 μm $\times$ 100 μm (b) at different temperatures. From the slope β_1 of these plots the high-frequency relative dielectric constant ε_r of the NiO films can be obtained:

$$\varepsilon_r = \frac{q^3}{\pi\varepsilon_0 d(2\beta_1 k_B T)^2}. \tag{6.6}$$

The in this way determined high-frequency relative dielectric constant are $\varepsilon_r = 16 \pm 0.9$ and $\varepsilon_r = 13 \pm 1.6$ for the nano crossbar devices and micro devices, respectively. These values are in good agreement with literature values of $\varepsilon_r = 17$ [103] and $\varepsilon_r = 11.9$ [142] for poly crystalline and single crystalline NiO, respectively.

Figure 6.5 shows the temperature dependence of the current density j plotted as $\ln(j)$ versus the inverse temperature $\frac{1}{T}$ measured at high voltage e.g. $V = 2$ V for the micro as well as the nano crossbar structures. According to equation (6.2) this should also result in a straight line,

$$\ln(j) = \beta_2 \cdot \frac{1}{T} + \ln(\alpha_2), \tag{6.7}$$

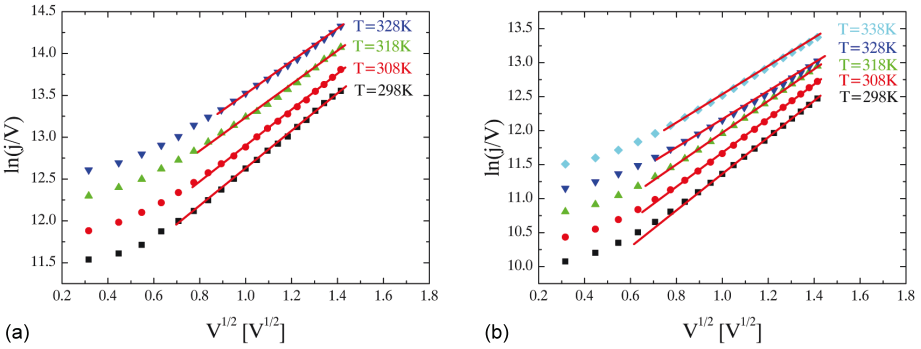

Figure 6.4: Poole Frenkel plots of 100 nm × 100 nm nano crossbar devices (a) and of 100 μm × 100 μm micro devices (b) at different temperatures. From the slope of these Poole-Frenkel plots the high-frequency relative dielectric constant of the NiO thin films can be determined.

with slope β_2

$$\beta_2 = \frac{1}{2k_B}\left(\sqrt{\frac{q^3E}{\pi\varepsilon_0\varepsilon_r}} - q\phi_{PF}\right), \tag{6.8}$$

and with the point of intersection with the axis of ordinate α_2

$$\alpha_2 = \sigma_0 \cdot E. \tag{6.9}$$

The slope of the lines plotted in figure 6.5 are determined to $\beta_2 = -2531$ K and $\beta_2 = -2265$ K for the nano crossbar and the micro devices, respectively. This yields an energy difference ϕ_{PF} between the valnence band and trap energy

$$\phi_{PF} = \frac{1}{q}\left(-2k_B\beta_2 + \sqrt{\frac{q^3E}{\pi\varepsilon_0\varepsilon_r}}\right), \tag{6.10}$$

of $\phi_{PF} = 609$ meV and $\phi_{PF} = 586$ meV for the nano crossbar devices and the micro devices, respectively.

Using equation (6.9), from the intersection with the axis of ordinate α_2 σ_0 can be determined, with

$$\sigma_0 = q\mu n_0, \tag{6.11}$$

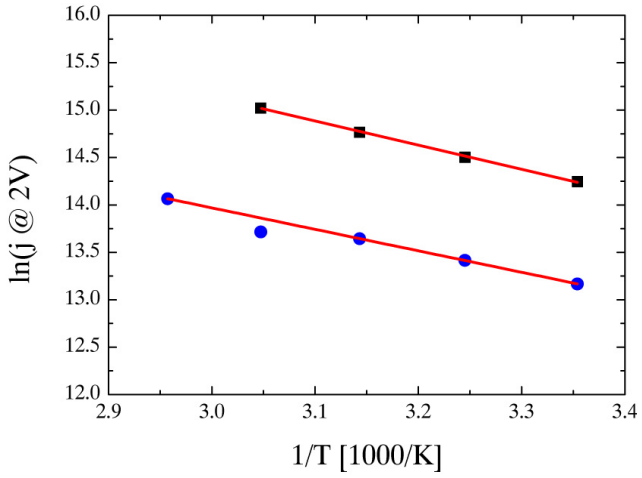

Figure 6.5: Temperature dependence of the current density measured at $V = 2$ V in the 100 nm $\times$ 100 nm nano crossbar devices (black squares) and in the 100 μm $\times$ 100 μm micro devices (blue circles). Plotting the natural logarithm of the current density against the inverse temperature at which the current density is measured, results in a straight line. The trap energy level with respect to the valence band is determined from the slope of this line. The charge carrier density can be derived from the point of intersection with the axis of ordinate.

where q is the charge of an electron, $\mu = 4 \cdot 10^{-5}\mathrm{m^2V^{-1}s^{-1}}$ is the mobility of the charge carriers (see chapter 2.2.4) and $n_0 = \sqrt{N_v N_t}$ where N_v and N_t represents the density of states at the top of the valence band and the density of traps, respectively.

Evaluation of the plots in figure 6.5 yields $\alpha_2 = 7.43 \cdot 10^9$ and $\alpha_2 = 1.04 \cdot 10^9$ which results in $n_0 = 1.45 \cdot 10^{25}$ m^{-3} and $n_0 = 2.03 \cdot 10^{24}$ m^{-3} using the previously determined ε_r for the nano crossbar devices and the micro devices, respectively. This gives a charge carrier density

$$n(V = 0\mathrm{V},\ T = 298\mathrm{K}) = n_0\ \exp\left[\frac{-q\phi_{PF}}{2k_BT}\right] \tag{6.12}$$

for $V \to 0$ V and at room temperature of $n = 1.03 \cdot 10^{20}$ m^{-3} and $n = 2.25 \cdot 10^{19}$ m^{-3} for the nano crossbar devices and the micro devices, respectively.

This is in good agreement with literature values of $n = 2.6 \cdot 10^{22}$ m^{-3} and $n = 2.0 \cdot 10^{24}$ m^{-3} for sputtered NiO_x films annealed at 500°C and at 600°C, respectively [94] and a value of $n = 1.2 \cdot 10^{19}$ m^{-3} for single crystal NiO [5].

6.2 Impedance measurements

Frequency-dependent impedance spectroscopy provides valuable information on the physical origins of electrical and dielectric properties, e.g. separation of bulk-based from electrode-related effects, along with the simultaneous measurement of material constants such as conductivity and dielectric constants.

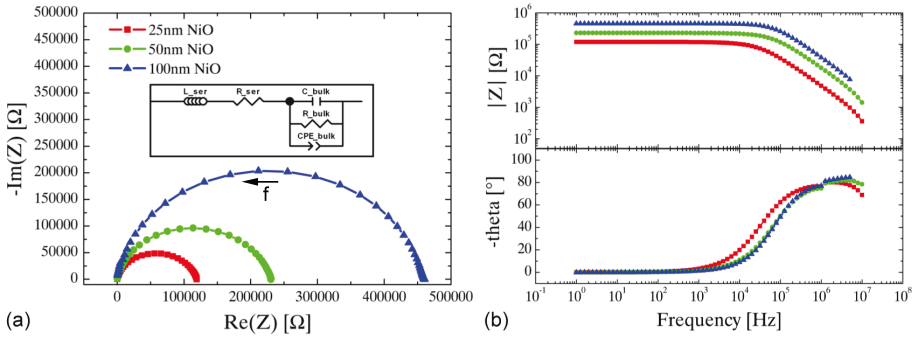

Figure 6.6: (a) The complex impedance plane plots of pristine micro samples with 25 nm, 50 nm and 100 nm NiO film thickness and 50 μm $\times$ 50 μm top electrode size. (b) The Bode plots of the magnitude of the impedance $|Z|$ and the phase as a function of frequency.

6.2.1 Thickness dependence of the device properties

Figure 6.6(a) shows the complex impedance plane plots of pristine micro samples with 25nm, 50nm and 100nm NiO film thickness measured on 50 μm $\times$ 50 μm top electrodes. As shown in the inset, the equivalent circuit for the pristine devices can be described by the parallel combination of a resistance R_{bulk} representing the DC resistance of the NiO layers, a capacitance C_{bulk} representing the capacitance of the NiO layers and a constant phase element CPE_{bulk}. The CPE's impedance is given by $Z_{CPE} = \frac{1}{Q_0(\omega i)^n}$, with $Q_0 = \frac{1}{|Z|}$ at $\omega = 1$ rad/s. The CPE is used to describe the typical frequency dependence of the resistivity of NiO films, possibly due to correlated barrier hopping [101]. This also accounts for the arc depression in the complex plane, shown in figure 6.6(a). At higher frequencies, the real part of the conductivity is a power function of the frequency f with an exponent n of about 0.75 (see table 6.1), as reported in NiO films obtained by high-temperature oxidation of Ni [103] and in NiO nanoparticles [18, 19, 142].

Additionally, the contributions of the lead wires are described by a serial connection of an inductor $L_{ser} = 3.179 \cdot 10^{-6}$ H and a resistor $R_{ser} = 28.52\ \Omega$,

which are fixed for all simulations. Their values are determined by analyzing the closed circuit impedance of the setup, as represented by the green squares in figure 6.8(b). The values of the R_{bulk}, C_{bulk} and CPE_{bulk} obtained from the impedance spectra for different NiO thicknesses can be found in table 6.1.

Thickness	C_{bulk}	R_{bulk}	CPE_{bulk}
25 nm	$1.563 \cdot 10^{-11}$ F	119 kΩ	$Q_0 = 2.443 \cdot 10^{-10}$ and $n = 0.831$
50 nm	$6.294 \cdot 10^{-12}$ F	230 kΩ	$Q_0 = 1.253 \cdot 10^{-10}$ and $n = 0.755$
100 nm	$2.836 \cdot 10^{-13}$ F	459 kΩ	$Q_0 = 2.167 \cdot 10^{-11}$ and $n = 0.820$

Table 6.1: Summary of the equivalent circuit parameters obtained by fitting the impedance spectra shown in figure 6.6 for samples with different NiO film thicknesses.

Clearly, a linear increase of R_{bulk} with the NiO film thickness and a linear increase of C_{bulk} with the reciprocal NiO film thickness is obtained. Therefore, the arcs observed in the complex impedance plots must originate from bulk-limited conduction according to

$$R_{bulk} = \rho \frac{d}{A} \text{ and } C_{bulk} = \varepsilon_0 \varepsilon_r \frac{A}{d}, \tag{6.13}$$

where ρ is the resistivity of the NiO film, ε_0 the permittivity of free space, ε_r the relative dielectric constant of NiO, A the electrode area and d the NiO film thickness. If the complex impedance plane plots in figure 6.6 would be interface-related, they would not scale with NiO film thickness. These dependencies, in addition to the fact that no second arc can be identified in the complex impedance plane plots, are additional strong indications for bulk-limited conduction and negligible interface contributions in pristine devices.

6.2.2 Electrode area dependence of the device properties

The inset of figure 6.7(b) shows the impedance spectra for different electrode sizes, measured on micro devices with 50 nm NiO film thickness. Using the equivalent circuit shown in the inset of figure 6.6(a) the DC resistance R_{bulk} and the DC capacitance C_{bulk} are determined. From R_{bulk} the DC conductivity $\bar{\sigma}$ is determined: $\bar{\sigma} = \frac{1}{\bar{\rho}} = \frac{d}{R_{bulk} \cdot A}$, where $d = 50$ nm is the film thickness and A is the electrode area. When the NiO film is homogeneous, $\bar{\sigma}$ is expected to be constant. However, as shown in figure 6.7(a), $\bar{\sigma}$ depends on the length L of the concerning square electrode. Obviously, the mean conductivity $\bar{\sigma}$ for smaller electrodes is higher than for larger electrodes. This can be explained by the formation of stoichiometric NiO under the center of the top electrodes induced

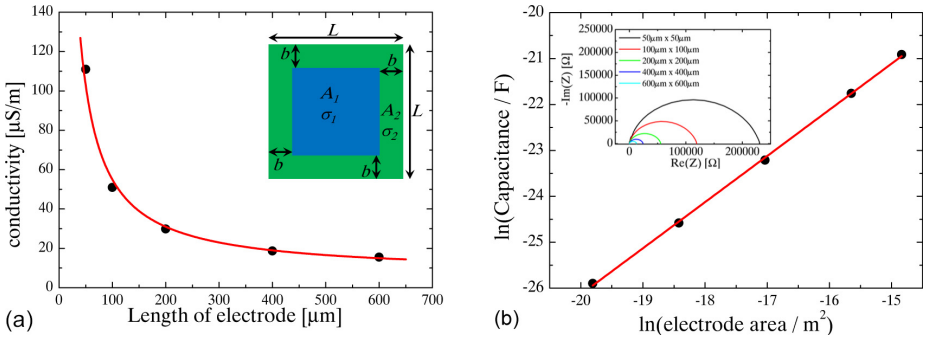

Figure 6.7: (a) The natural logarithm of the conductance and (b) the natural logarithm of the capacitance as a function of the natural logarithm of the electrode area of a micro sample with a NiO film thickness of 50 nm.

by the heat during the sputter deposition of the Pt, as mentioned before in chapter 5.4. However, the NiO under the edges of the Pt top electrodes might not reach the temperature necessary to form stoichiometric NiO, because the surrounding NiO is shielded by photoresist during the deposition process. This results in top electrodes having well conducting edges of width b (see inset of figure 6.7(a)) compared with the center of the electrodes. However, the area A_1 of the stoichiometric NiO increases with increasing top electrode area L^2. Therefore, the well conducting edges dominate for smaller electrodes and the high resistive stoichiometric area A_1 dominates for larger electrodes, resulting in the observed dependence.

Using the sketch drawn in the inset of figure 6.7(a) the dependence of the mean conductivity $\bar{\sigma}$ on the length L of the electrode is derived:

$$\bar{\sigma} = G_{tot} \cdot \frac{d}{L^2} = (G_1 + G_2) \cdot \frac{d}{L^2}, \tag{6.14}$$

where

$$G_1 = \sigma_1 \cdot \frac{A_1}{d} = \frac{\sigma_1}{d} \cdot (L - 2b)^2 \tag{6.15}$$

is the conductance in the stoichiometric area A_1 and

$$G_2 = \sigma_2 \cdot \frac{A_2}{d} = \frac{\sigma_2}{d} \cdot 4\,(L - b)\,b \tag{6.16}$$

is the conductance in the well conducting area A_2. σ_1 and σ_2 are the conductivities of area A_1 and A_2, respectively, $d = 50$ nm is the NiO film thickness and b is the width of the well conducting edges.

From equations (6.14), (6.15) and (6.16) follows for the mean conductivity $\bar{\sigma}$

$$\bar{\sigma} = \frac{\sigma_1 \cdot (L-2b)^2 + \sigma_2 \cdot 4b\,(L-b)}{L^2}. \tag{6.17}$$

The fit of this equation on the measured data is shown by the red line in figure 6.7(a). A width of $b = 90$ nm is found for the well conducting edges of the electrodes. Further the conductivity for the high resistive area $\sigma_1 = 7$ μS/m is found, which is still well above the conductivity $\sigma_{stoich} < 10^{-11}$ S/m of stoichiometric NiO reported in literature [122]. For the conductivity of the well conducting edge $\sigma_2 = 14$ mS/m is found. This value is comparable with the values found by R_{Sheet} measurements (see chapter 5.4).

Figure 6.7(b) shows the natural logarithm of the capacitance as a function of the natural logarithm of the electrode area of a micro sample with a NiO film thickness of 50 nm. This yields a linear dependence with a slope equal to 1 as expected from equation (6.13).

Additionally the relative dielectric constant ε_r of NiO is calculated from the determined capacitance and the related NiO film thickness: $\varepsilon_r = 12.39 \pm 0.55$. This is in good agreement with reported bulk values of $\varepsilon_r = 17$ [103] and $\varepsilon_r = 11.9$ [142] for polycrystalline and single crystalline NiO, respectively.

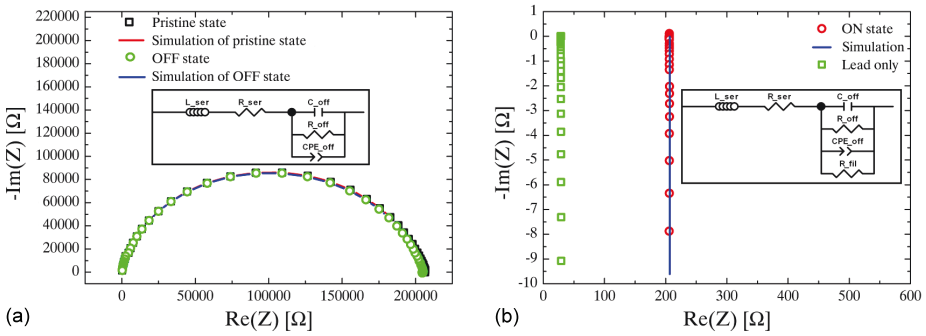

Figure 6.8: (a) The complex impedance plane plot of a pristine (black squares) and a OFF state (green circles) measured on a micro device with 50 nm NiO film thickness and a top electrode size of 50 μm $\times$ 50 μm. The inset shows the equivalent circuit used to simulate the two resistance states. (b) The complex impedance plane plot of a short circuit measurement (green squares) and of an ON state (red circles) measured on a micro device with 50 nm NiO film thickness and a top electrode size of 50 μm $\times$ 50 μm. The insets show the equivalent circuits used to simulate the corresponding resistance states.

Figure 6.8(a) shows the complex impedance plane plot of a device in the pristine

state and of a device in an OFF state measured on a micro device with 50 nm NiO film thickness and a top electrode size of 50 μm $\times$ 50 μm. By using the equivalent circuit shown in the inset of figure 6.8(a) it is found, that the capacitance of the device in the pristine state $C_{pristine} = 4.765 \cdot 10^{-12}$ F has an almost identical value as the capacitance of the device in the OFF state $C_{off} = 4.766 \cdot 10^{-12}$ F. This shows that the NiO layer is only locally changed by the forming and switching operations.

The complex impedance plane plot of the device in the ON state is shown in figure 6.8(b). It is simulated by and additional resistance $R_{fil} = 177.6\Omega$ parallel to the bulk contributions as shown in the inset. This suggests that the ON state consists of percolated interconnections of highly conducting components between the two electrodes embedded into the insulation NiO layer. The result of the simulation is represented by the blue line in figure 6.8(b), which matches the experimental data quite well.

In summary, use of impedance measurements on devices in the pristine, OFF and ON state shows that there is no interface contribution to the overall impedance, i.e., there is nothing like deformation of a Schottky barrier depletion layer involved in the resistive switching processes in the case of NiO in combination with the here used electrode materials. The ON state can be modeled by a parallel resistance that shortcuts the bulk impedance. This, in addition to the identical capacitance of devices in the pristine and off state indicates that the switching behaviour in NiO thin films originates from local, filamentary changes in conductivity, embedded in an almost unchanged NiO matrix.

6.3 Influence of oxygen content in the NiO_x film

In order to investigate the influence of different oxygen content in the NiO_x film on the resistive switching behaviour, plug devices as described in chapter 4.1 are fabricated with different O/Ni ratios of 1.0, 1.15, 1.20 and 1.25. The stoichiometric sample is sputtered by RF magnetron sputtering from a stoichiometric NiO target with a sputter power of $P = 98$ W and an Argon flow rate of 60 sccm resulting in a pressure during the sputtering process of $p = 1.41 \cdot 10^{-2}$ mbar. The non-stoichiometric samples are deposited by DC reactive sputtering from a metallic Ni target with a sputter power of $P = 300$ W and Ar/O_2 mixtures of 54 sccm / 6 sccm, 52 sccm / 8 sccm and 50 sccm / 10 sccm resulting at a total gas pressure during sputtering of about $p = 2 \cdot 10^{-2}$ mbar. The oxygen content is determined by RBS measurements as discussed in chapter 5.1.

To examine the impact of the O content in the NiO_x films on the typical resistive switching behaviour, devices with the same NiO_x film thickness of 30nm, Pt top electrodes of 50nm thickness and square plugs of 280 nm $\times$ 280 nm are compared with each other. Figure 6.10 shows the typical unipolar current-voltage and the corresponding resistance-voltage curves for the different NiO_x films during resistive switching. For all measurements the voltage step and the

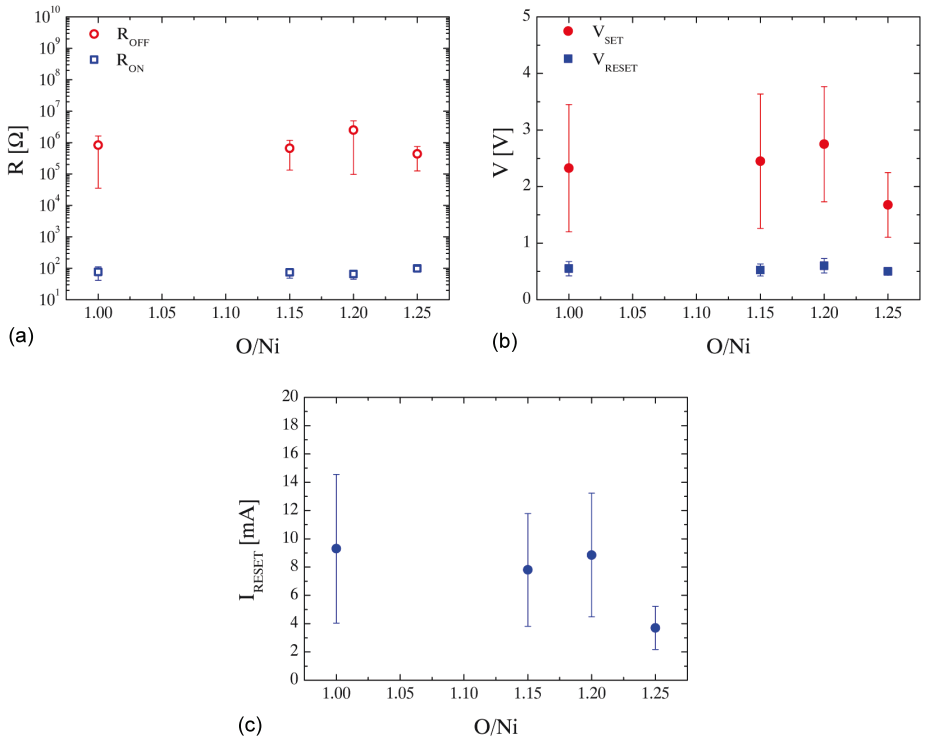

Figure 6.9: The influence of the oxygen content in the NiO_x films on the typical LRS and HRS resistances (a), on the SET and RESET voltages (b) and on the RESET current (c). For all samples the current compliance is set to $I_{CC} = 3$mA, the voltage step and the delay time are set to 25 mV and 250 ms, respectively, while the voltage sweeps are performed from 0 V to 5 V to 0 V for all forming and from 0 V to 4 V to 0 V for all SET and from 0 V to 1 V to 0 V for all RESET operations.

delay time are set to 25 mV and 250 ms, respectively, while the voltage sweeps are performed from 0V to 5V to 0V for the forming, from 0V to 4V to 0V for the SET operations and from 0 V to 1 V to 0 V for the RESET operations.

The typical SET (and forming) operation starts in a high resistance state (HRS) which is identified by the low current, which increases with increasing voltage. When the SET voltage (V_{SET}) is reached, an abrupt decrease in the resistance and a corresponding increase of the current is observed. To prevent the device from permanent breakdown a current compliance is set to a value of $I_{CC} = 3$ mA for all devices, which limits the current during the SET and forming operation. After the SET process, the device is in a low resistance state (LRS). Because in the LRS the programmed voltage V, displayed on the x-axis, would cause a current exceeding the current compliance, the voltage over the device V_{DUT} is decreased to a voltage value $V_{DUT} = R_{LRS} \cdot I_{CC}$ where R_{LRS} is the

actual resistance in the LRS. This is represented by the horizontal line (I_{CC}) in the current-voltage and by the corresponding steadily increasing line in the resistance-voltage plots. This condition is kept, until the programmed voltage V decreases to a value corresponding to a current below the compliance current. The duration of this condition is determined by the programmed voltage step size and the programmed delay time between each voltage step. When the current evoked by the decreasing programmed voltage V does not exceed the compliance current any more, a linear decrease with the decreasing voltage is observed until zero voltage.

During a typical RESET operation the device is initially in a LRS and the current increases linearly with the voltage. When the programmed voltage reaches the RESET voltage (V_{RESET}), the current gradually decreases with increasing voltage, until the HRS is reached again.

What first strikes the eye is the wide spread of SET voltages and RESET currents for all films (see figure 6.9). The wide distribution in SET voltages could be explained by the wide spread of the resistance of the HRS. The higher the HRS resistance, the thinner are the leftovers of the filament after the RESET process (see chapter 6.4.1). The thinner the remains of the filament, the higher is the voltage (V_{SET}) to restore the filament during the SET operation.

The wide distribution in the RESET currents can be explained by the wide range of LRS resistances. A lower the LRS resistance means a larger cross-sectional area of the filament (see chapter 6.4.1). Thus, more Joule power is needed to dissolve or reoxidize the filament (see chapter 2.1.2, figure 2.5).

The reason for this large spread in the LRS resistances is found in the experimental setup. The standard setups used for resistive switching have a "dead time" of about 100 μs before the current compliance reacts to the abrupt increase in current during the SET and forming operation. This results in a current overshoot during the first 100 μs which cannot be controlled, so that the maximum current operating during this "dead time" is unknown [83, 62, 170].

Because of these wide distributions in V_{SET} and I_{RESET} in addition to the fact that the V_{RESET} varies much less but is located between 500 mV and 750 mV for all films, no clear dependence of the switching parameters on the oxygen content is found. Only the film with the highest O/Ni ratio of 1.25 shows a different behaviour. For these samples lower V_{SET} and I_{RESET} values are observed. This is in agreement with less stable switching, because of less stable ON and OFF states, or even threshold switching (see chapter 2.1.2) at higher oxygen contents as reported by *Seo et al.* [155] and *Park et al.* [137].Therefore, further more detailed studies were performed on devices with nearly stoichiometric NiO.

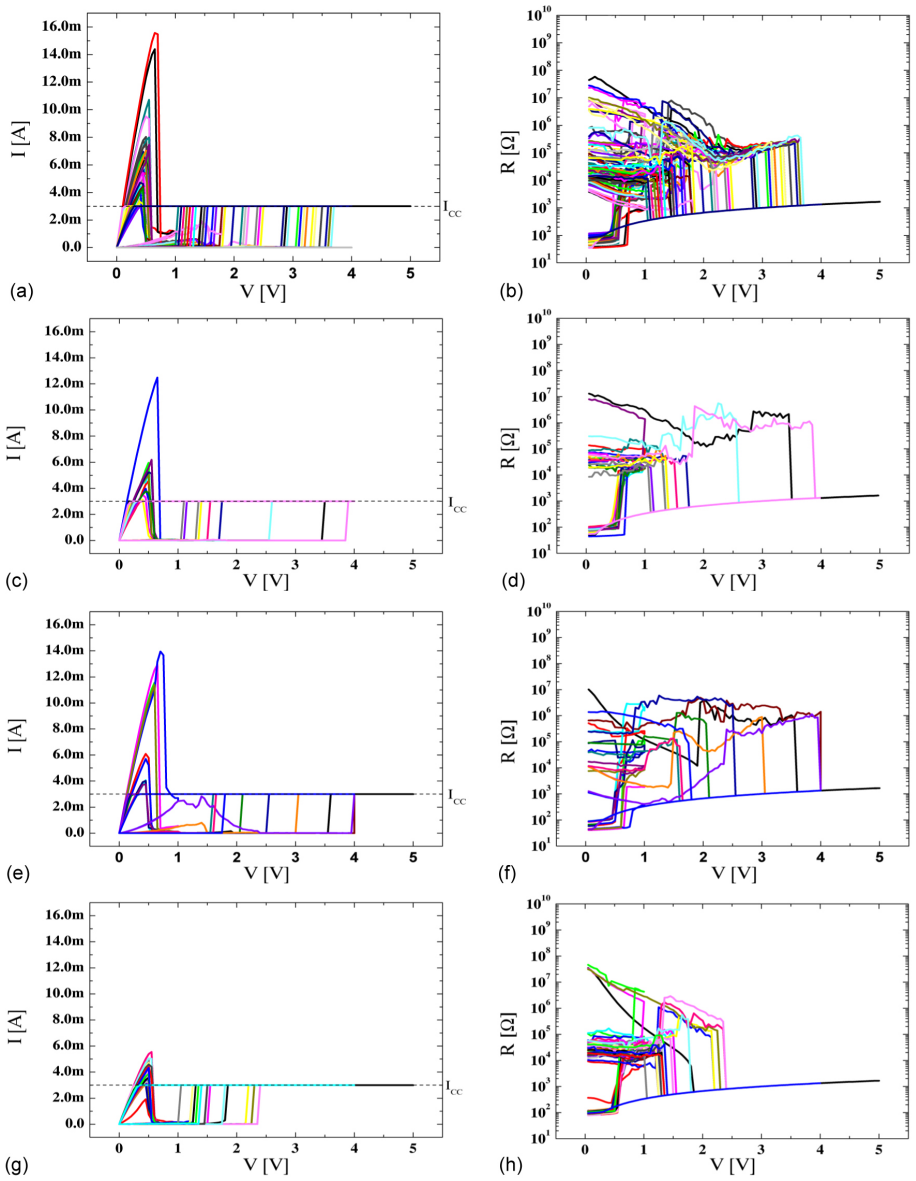

Figure 6.10: Current-voltage and resistance-voltage plots of the forming operation (black lines) and several SET and RESET operations for NiO_x films of O/Ni ratios of 1 (a) (b), 1.15 (c) (d), 1.20 (e) (f) and 1.25 (g) (h). The stoichiometric NiO films are sputtered by RF magnetron sputtering from a stoichiometric NiO target, while the non-stoichiometric films are deposited by DC reactive magnetron sputtering from a metallic Ni target.

6.4 Switching behaviour of stoichiometric NiO films

The resistive switching behaviour of stoichiometric NiO films in plug devices is investigated in more detail for the first 60 switching cycles to ensure that no wear out phenomena influence the behaviour. The NiO films are deposited by RF sputtering from a stoichiometric NiO target with pure Argon as sputter gas at a flow rate of 60 sccm and a sputter power of $P = 98$ W. The NiO film thickness is 30 nm and the Pt top electrode thickness is 50 nm, while the bottom plug has a cell size of 280 nm $\times$ 280 nm.

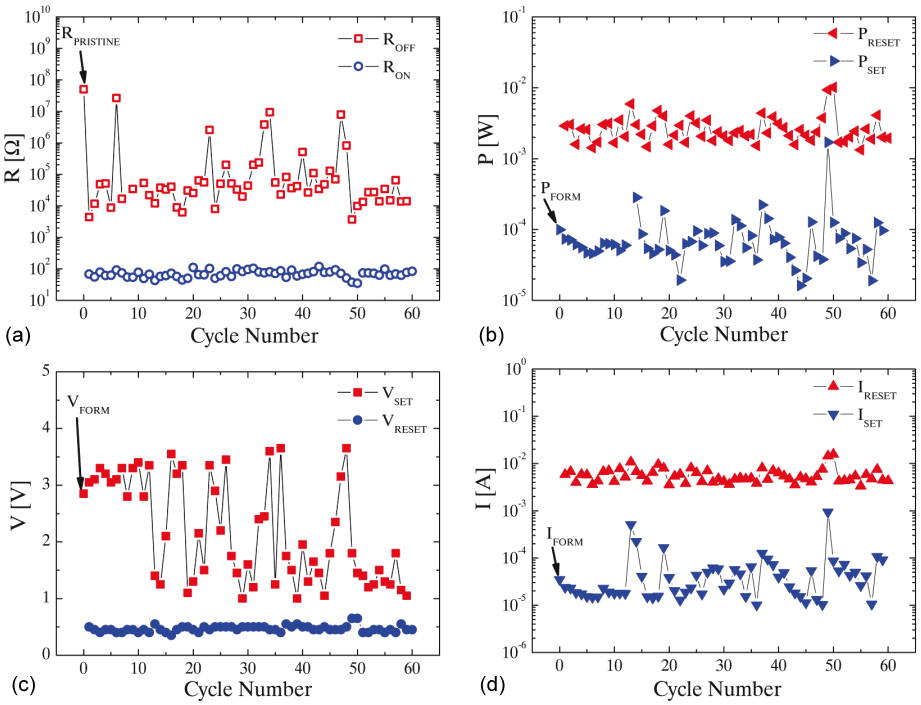

Figure 6.11: (a) The resistance of the LRS (R_{ON}) and HRS (R_{OFF}) as a function of the cycle number. The first value of the R_{OFF} curve represents the resistance of the pristine sample. (b) The released power during the RESET and SET processes as a function of the cycle number. The first value of the P_{SET} curve represents the power released during the forming process. (c) The SET and RESET voltage and (d) the SET and RESET current as a function of the cycle number. The first value of the V_{SET} curve represents the forming voltage and the first value of the I_{SET} curve represents the forming current.

Figure 6.11(a) shows the resistance in the LRS (R_{ON}) and HRS (R_{OFF}) as a function of the cycle number. The first cycle of the HRS curve represents the

resistance of the pristine sample ($R_{Pristine}$). After forming, the HRS resistances do not reach the resistance of the pristine state any more. This is in agreement with the statement of *Jung et al.* [72] that the HRS consists of metallic remains of the filament embedded in the semiconducting NiO film (see chapter 2.1.2). The values of the HRS resistances show a broad distribution between several kΩ and several tens of MΩ. According to *Jung et al.* [72] this corresponds to thinner or thicker cross-sectional area of the remains of the filament. The values of the LRS resistances show a much narrower distribution. Overall, a wide window between the LRS and HRS resistances, which is needed for a clear assignment of the resistance states, and no trend or degradation in the resistance states can be identified.

The SET- and RESET voltages as well as the SET- and RESET currents as a function of the cycle number are shown in figure 6.11(c) and (d), respectively. Clearly visible is the broader distribution in the SET voltages as well as in the SET currents compared to the RESET voltages and RESET currents. The first value in the SET voltage and -current curves represents the forming voltage (V_{FORM}) and -current (I_{FORM}), respectively. The value of the forming voltage is in the range of the other SET voltages and the value of the forming current is in the range of the other SET currents, while the sweep rate and the current compliance are the same for the forming as well as the subsequent SET processes. This means that no different treatment from the "normal" SET procedure is needed for the forming of a filament and therefore these samples with a NiO film thickness of 30 nm are called *forming free*.

Figure 6.11(b) shows the power $P = V \cdot I$ dissipated by *Joule heating* at the initiation of the SET process (P_{SET}) and the RESET process (P_{RESET}). The power needed for the forming process (P_{FORM}), represented by the first value of the P_{SET} curve, is in the range of the other values. This is in agreement with the previous statement of *forming free* devices. What additionally catches the eye is the fact that the heat production due to Joule heating at the onset of the RESET process is much higher than that produced at the onset of the SET process. Particularly, when the dimension of the filament to be broken during the RESET process is taken into account, it becomes clear that this filament, which carries the main part of the current, becomes much hotter than the whole NiO film during the SET process.

If the LRS is assumed to consist of a cylindrical metallic nickel filament embedded in a semiconducting NiO film as pictured in figure 6.12(d) with a length equal to the NiO film thickness $d = 30$ nm, its cross-sectional area A_{CF} can be estimated from the R_{ON} of the filament in question according to

$$R_{ON} = \rho_{Ni} \cdot \frac{d}{A_{CF}} \tag{6.18}$$

where $\rho_{Ni} = 6.93 \cdot 10^{-8}$ Ωm is the electrical resistivity of nickel [99]. With 40 Ω $< R_{ON} <$ 120 Ω a cross-sectional area $1.73{\cdot}10^{-17}$ m^2 $< A_{CF} < 5.20{\cdot}10^{-17}$ m^2 and a corresponding filament radius of 2.35 nm $< r_{CF} <$ 4.07 nm is obtained.

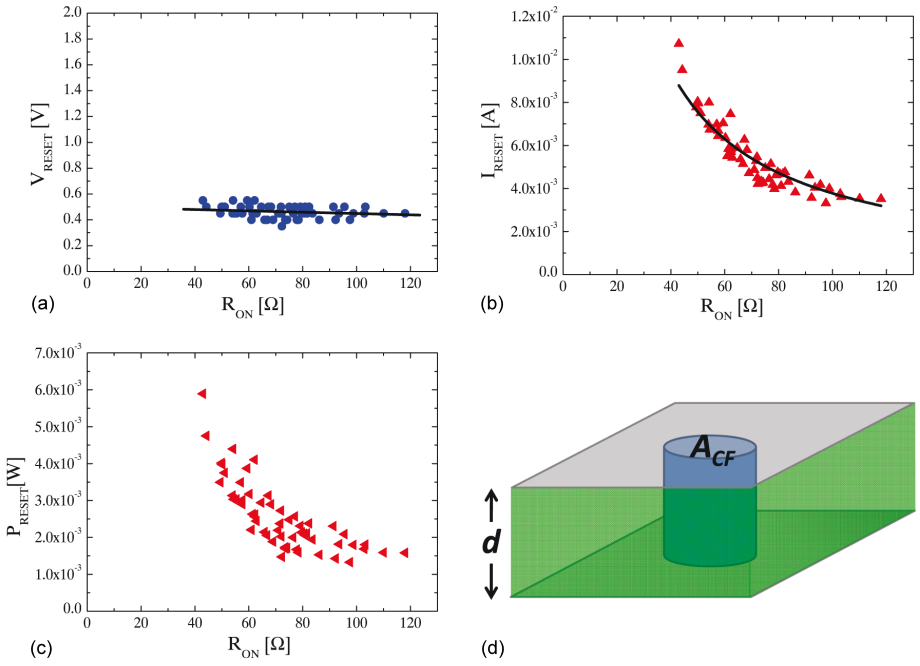

Figure 6.12: The dependencies of (a) V_{RESET}, (b) I_{RESET} and (c) $P_{RESET} = V_{RESET} \cdot I_{RESET}$ on the prevailing LRS resistance of the device. (d) A simple model of a conducting cylindrical filament embedded in a semiconducting NiO film.

According to the filament model (see chapter 2.1.2) the distribution of the RESET parameters, e.g. V_{RESET} and I_{RESET}, should be related to the radius of the existing cylindrical filament to be ruptured by the subsequent RESET process. Therefore, in figure 6.12(a) and (b) V_{RESET} and I_{RESET} are plotted as a function of the prior R_{ON}, respectively. The RESET voltage appears to be almost independent on the resistance R_{ON} in the previous ON state and has a value of about $V_{RESET} = 0.4$ V.

The RESET current, on the other hand, shows a clear dependence on R_{ON}. A fit of the I_{RESET} as a function of R_{ON} (represented by the black line in figure 6.12(b)) with

$$I_{RESET} = C \cdot \frac{1}{R_{ON}} \tag{6.19}$$

yields $C = V_{RESET} = 0.38 \pm 0.005$V. This is in good agreement with the measured value of V_{RESET} determined from figure 6.12(a). The dissipated Joule

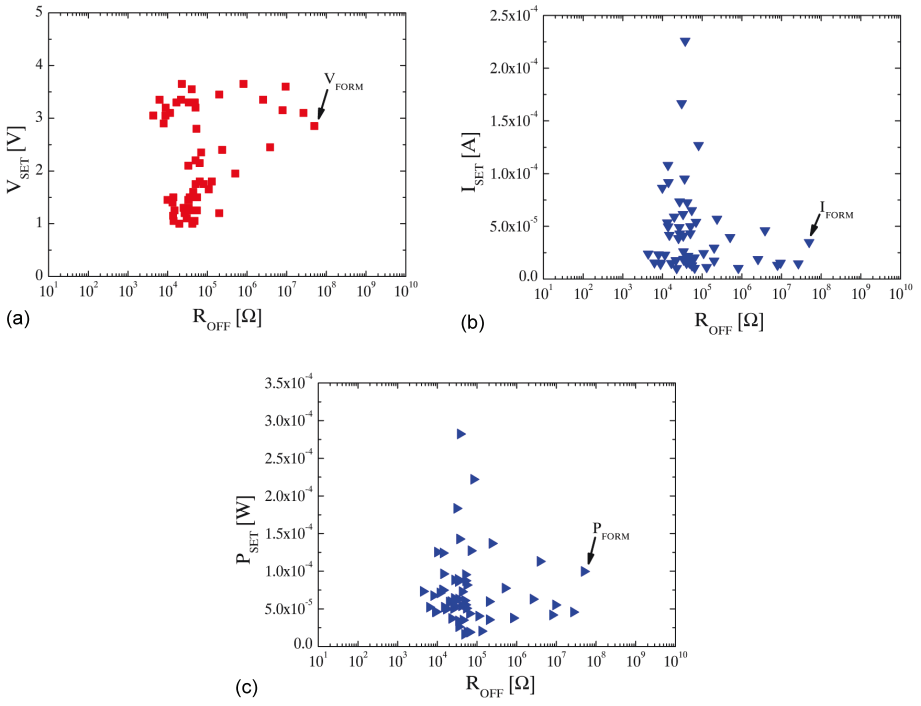

Figure 6.13: The dependencies of (a) V_{SET}, (b) I_{SET} and (c) $P_{SET} = V_{SET} \cdot I_{SET}$ on the prevailing HRS of the device before the SET process in question. The forming voltage, current and power are indicated by V_{FORM}, I_{FORM} and P_{FORM}, respectively.

heating ($P_{RESET} = V_{RESET} \cdot I_{RESET}$) (shown in figure 6.12(c)) at the onset of the RESET process has therefore a similar dependence as the RESET current.

The observed behaviour can be interpreted using the model proposed by *D. Ielmini et al.* [147, 65, 63]. In this model the RESET process is described by a *thermally activated dissolution* of a conducting cylindrical filament embedded in a semiconducting NiO film as pictured in figure 6.12(d). According to this model, during the application of a voltage sweep or pulse, the temperature within the filament increases due to Joule heating, which increases the probability of reoxidation of the filament. *Atomistically*, this can be understood in the way that the dissipated Joule heating within the filament enhances the mobility of the excess metallic Ni, constituting the conductive filament, and of the excess O in the surrounding NiO, originating from the forming of the filament. The excess Ni will then diffuse away from the hot filament into the surrounding NiO, and the excess O in the NiO toward the filament, because of the temperature and concentration gradients. This thermochemical process is

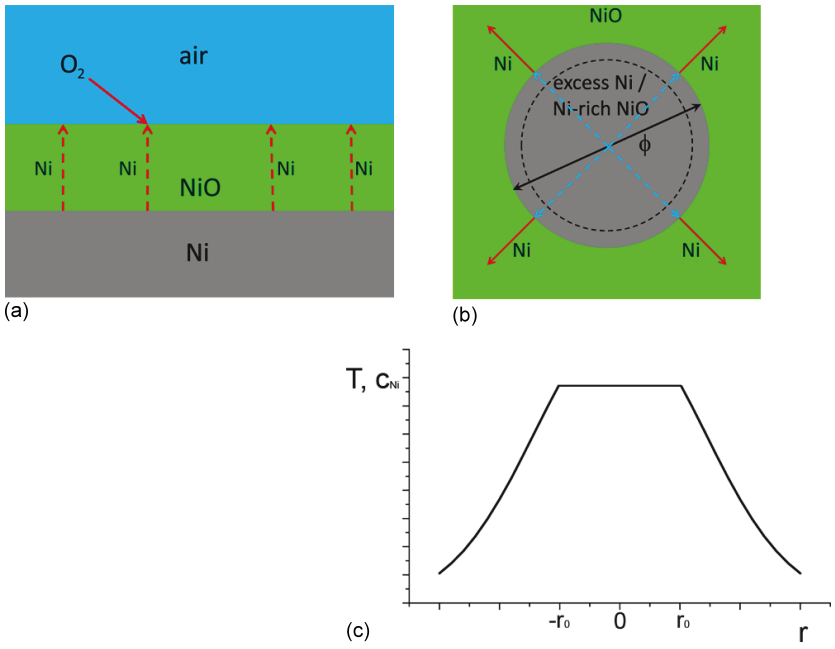

Figure 6.14: (b) Possible RESET process according to the filament dissolution model, based on the oxidation of Ni thin films shown in (a) [93]. (c) Presumable Ni concentration c_{Ni} and temperature T as a function of distance r to the center of the filament.

believed to be mediated by the outward diffusion of the excess Ni into NiO (possibly enhanced by grain boundary diffusion [95]), because of the much higher mobility of Ni in NiO [119, 93, 43, 11]. A similar mechanism is observed for the oxidation of metallic Ni thin films [93] (see figure 6.14). Thus, based on the *Einstein-Smoluchowski-Equation* describing the mean square displacement λ_x of (random walk) diffusing particles during time t in one dimension [45]

$$\lambda_x = \sqrt{\bar{x}^2} = \sqrt{2Dt} \tag{6.20}$$

the RESET time τ_{RESET} can be estimated as the time for radial diffusion through a distance r equal to the half of the filament diameter ϕ, namely [64]

$$\tau_{RESET} = \frac{\phi^2}{D} = \frac{\phi^2}{D_0} \cdot e^{\frac{E_A}{kT}} \tag{6.21}$$

where T is the maximum temperature within the filament, k the Boltzmann constant, D the diffusion constant given by the Arrhenius law using a preexpo-

nential constant D_0 and the activation energy for diffusion E_A. Equation (6.21) finds physical basis in the well-known Arrhenius dependence of both diffusion and chemical reactions, which is consistent with the observed temperature dependence of RESET parameters [148, 147]. The measured activation energy obtained from *Kissinger analysis* of RESET and retention experiments is equal to 1.4 eV [65, 29]. This value is also comparable to the calculated activation energy of about 1.5 eV for Ni self-diffusion along grain boundaries in NiO [75] and the measured activation energy of about 1.2 eV [179] for Ni self-diffusion along grain boundaries in Ni, supporting the key role of *nickel diffusion* as the limiting step in the RESET process.

The RESET voltage V_{RESET} needed to raise the local filament temperature to the critical value T_{RESET} is calculated from the steady-state solution of the Fourier equation for Joule heating, that is [147, 63]

$$V_{RESET} = \sqrt{\frac{R}{R_{th}} \left(T_{RESET} - T_0\right)} \tag{6.22}$$

where R_{th} is an effective thermal resistance of the conductive filament. For a metallic filament at T_{RESET}, the ratio between R and R_{th} can be given by the Wiedemann-Franz law yielding [147]

$$\frac{R}{R_{th}} = \frac{8\kappa_{th}}{\sigma} = 8LT_{RESET} \tag{6.23}$$

where κ_{th} is the thermal conductivity, σ is the electrical conductivity and $L = 2.48 \cdot 10^{-8}$ $\mathrm{V^2K^{-2}}$ is the Lorenz constant [64]. The factor 8 in equation (6.23) comes from the steady-state solution of the Fourier equation during RESET in the conductive filament and is due to the uniform Joule dissipation and the heat conduction toward the top and bottom electrode, which act as heat sinks [147, 63].

Therefore, in the case of a metallic filament at $T = T_{RESET}$ equation (6.22) can be written as

$$V_{RESET} = \sqrt{8LT_{RESET}\left(T_{RESET} - T_0\right)}. \tag{6.24}$$

For a constant V_{RESET} (as shown in figure 6.12(a)) and a constant ambient temperature T_0 a constant T_{RESET} is found. According to this model, a $T_{RESET} = 1126\mathrm{K}$ is required for the RESET operation in the plug devices used for the resistive switching experiments described in this chapter, assuming $T_0 = 300$ K and $V_{RESET} = 0.4$ V. This means that T_{RESET} is well below the melting temperatures of metallic Ni ($T_{Ni,melt} = 1728\mathrm{K}$), Pt ($T_{Pt,melt} = 2041\mathrm{K}$) and NiO ($T_{NiO,melt} = 2257\mathrm{K}$) [29], which supports the model of thermally activated diffusion of nickel away from the conductive filament into the surrounding NiO. Therefore, melting of the filaments can probably be discarded as the responsible mechanism for the RESET process.

Considering the fact that the current is predominantly carried by the conductive filament, the current density in the conductive filament at the onset of the RESET process can be estimated. From equation (6.18) and with

$$I_{RESET} = j_{CF} \cdot A_{CF} \tag{6.25}$$

one gets the current density in the filaments needed to initiate the RESET process

$$j_{CF} = \frac{R_{ON} \cdot I_{RESET}}{\rho_{Ni} \cdot d} = \frac{V_{RESET}}{\rho_{Ni} \cdot d} = 2.07 \cdot 10^{14} \mathrm{Am}^{-2}. \tag{6.26}$$

Summarized, this means that for the initiation of the RESET process measured on the described plug devices a $V_{RESET} = 0.4$ V and a $j_{CF} = 2.07 \cdot 10^{14}$ Am^{-2} are required, *independently* of the particular R_{ON}. In the plots of the SET parameters as a function of the prevailing HRS resistance as shown in figure 6.13 on the other hand, no clear dependence on the preceding HRS resistance can be identified.

6.4.1 Scaling

For the future application of resistive switching memory devices, the effect of the electrode size and the active film thickness on the switching properties is of great interest. Therefore, micro devices as described in chapter 4.3 with 150 nm NiO film thickness and square pads of 50 μm × 50 μm, 100 μm × 100 μm, 200 μm × 200 μm and 400 μm × 400 μm are compared with each other. The forming and resistive switching is performed using $I(V)$ sweeps with a sweep rate of 200 mV/s. For the forming and SET process a current compliance of 600 μA is set. The voltage is swept from 0 V to 3.5 V to 0 V for the SET process and from 0 V to 1 V to 0 V for the RESET process. The resistances of the different states, measured at a low voltage of 100 mV, are shown in figure 6.15(a).

The log-log-plot of the resistances of pristine cells ($R_{Pristine}$) as a function of the electrode area A shows a slope of nearly -1 in agreement with the expected pad size scaling according to

$$R_{Pristine} = \rho_{NiO} \cdot \frac{d}{A}, \tag{6.27}$$

where ρ_{NiO} is the resistivity of NiO and d is the NiO film thickness. This means, that in the pristine state there is a uniform current density through the NiO film over the whole electrode area.

The log-log-plot of the LRS resistance (R_{ON}) however shows no major change by variation of the electrode area A. Therefore, the current can not be distributed uniformly over the whole electrode area but must be concentrated in an area

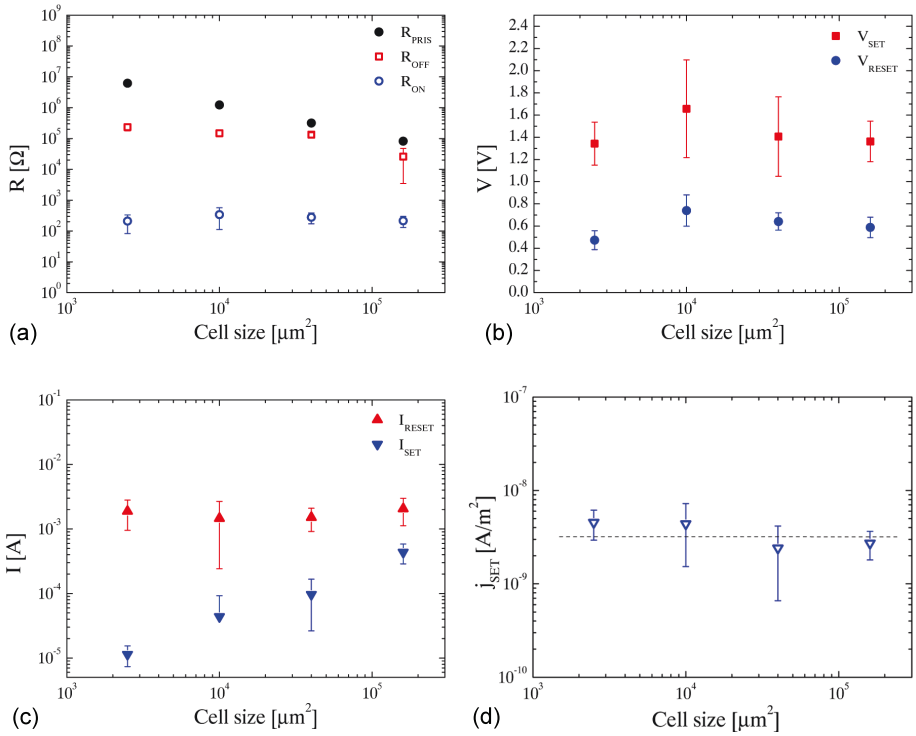

Figure 6.15: Cell size dependence of $R_{Pristine}$, R_{ON} and R_{OFF} determined at 100 mV (a), V_{SET} and V_{RESET} (b), I_{RESET} and I_{SET} (c) and j_{SET} (d) measured on a micro devices with a 150 nm NiO active layer.

smaller than the smallest electrode area used in this experiment. This supports the model of a single filament, or one or a few dominating filaments for the LRS as described in chapter 2.1.2.

Also the HRS resistance (R_{OFF}) shows no major change by variation of the electrode area A. Therefore, also the current density in the HRS can not be distributed uniformly over the whole electrode area, although the total current in the HRS is 2 - 3 orders of magnitude smaller than that measured in the LRS at the same voltage stress. The combination of these two facts makes it plausible, that some kind of filamentary conduction is still present in the HRS.

Often a local rupture somewhere along the filament is discussed to explain the HRS behaviour. Using the scaling behaviour of $R_{Pristine}$ and R_{OFF} and assuming a single cylindrical Ni filament in the LRS, as proposed by *Russo et al.* [148], the size of the ruptured part of the filament in the HRS can be estimated (see figure 6.16). First, the resistivity of the NiO film is determined by

$$\rho_{NiO} = R_{Pristine} \cdot \frac{A}{d} \approx 8.94 \cdot 10^4 \ \Omega\text{m}, \tag{6.28}$$

where $R_{Pristine}$ are the resistances of the pristine samples with the corresponding electrode area A, taken from figure 6.15(a) ,and $d = 150$ nm is the NiO film thickness.

Using the electrode dependence of the resistance R_{ON} in the LRS , which can be expressed as

$$\frac{1}{R_{ON}} = \frac{1}{R_{fil}} + \frac{1}{R_{rest}} = \frac{1}{\rho_{Ni} \cdot \frac{d}{A_{cf}}} + \frac{1}{\rho_{NiO} \cdot \frac{d}{A - A_{cf}}}, \tag{6.29}$$

the cross-section of the conductive filament A_{cf} can be calculated according to

$$A_{cf} = \frac{\rho_{Ni}\rho_{NiO}d - R_{ON}A\rho_{Ni}}{R_{ON}(\rho_{NiO} - \rho_{Ni})} \approx 4 \cdot 10^{-17} \ \text{m}^2, \tag{6.30}$$

where $\rho_{Ni} = 6.93 \cdot 10^{-8}$ Ωm is the resistivity of Ni, ρ_{NiO} is the resistivity of the semiconducting matrix of the cell as determined above, $d = 150$ nm is the NiO film thickness and R_{ON} and A are the values for the resistances of the ON states and the cell area, respectively, taken from figure 6.15(a). $R_{rest} = \rho_{NiO} \cdot \frac{d}{A - A_{cf}}$ represents the resistance of the undisturbed part of the cell. The value of A_{cf} in these micro samples is in good agreement with the A_{cf} determined in chapter 6.4 for the plug devices and corresponds to a radius of the cylindrical filament of $r_{cf} = 3.57$ nm.

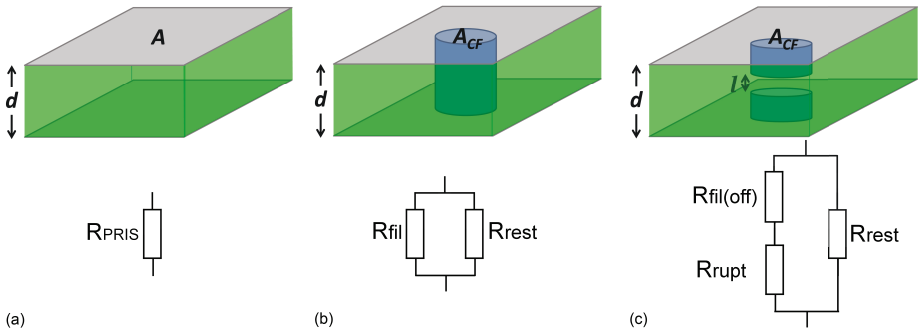

Figure 6.16: A simple model of the pristine cell (a), of the LRS (ON state) (b) and a putative model of the HRS (OFF state) (c) and their equivalent circuits.

Both the resistances of the LRS (R_{ON}) and of the HRS (R_{OFF}) are independent of the electrode area. Therefore, it is assumed that the resistances of the HRS are mainly determined by the resistance of the remains of the conductive filament, $R_{fil(off)} = \rho_{Ni} \cdot \frac{d-l}{A_{cf}}$, connected in series with the resistance of the ruptured part $R_{rupt} = \rho_{NiO} \cdot \frac{l}{A_{cf}}$. Here, l represents the size of the assumed gap in the filament in the HRS (see figure 6.16(c)). Nevertheless, there also exists a small additional parallel leakage current through the rest of the cell, which is responsible for some possible minor scaling of the R_{OFF} with the electrode area A. The resistance of the HRS (R_{OFF}) can therefore be written as

$$\frac{1}{R_{OFF}} = \frac{1}{R_{fil(off)} + R_{rupt}} + \frac{1}{R_{rest}}, \tag{6.31}$$

where $R_{rest} = \rho_{NiO} \cdot \frac{d}{A-A_{cf}}$ represents the resistance of the undisturbed rest of the cell. From this, the size l of the ruptured part of the filament can be estimated:

$$\begin{aligned} l &= \frac{d\,(-\rho_{Ni} d \rho_{NiO} + R_{OFF} A_{cf} \rho_{NiO} + R_{OFF} \rho_{Ni} (A - A_{cf}))}{-\rho_{Ni} d \rho_{NiO} + \rho_{NiO}^2 d + R_{OFF} (\rho_{Ni} - \rho_{NiO})(A - A_{cf})} \\ &\approx 8 \cdot 10^{-17}\ \text{m}. \end{aligned} \tag{6.32}$$

Since this value is physically unreasonable, the assumption that the ruptured part of the filament consists of NiO, with a resistivity equal to the resistivity of the NiO of the pristine cell (ρ_{NiO}), must be revised. Therefore it is likely that the ruptured part rather consists of a mixture of NiO and metallic Ni. Also the assumption of a simple cylindrical shape of the filament may be needed to be revised. It is likely that the cross-section of the filament near the ruptured site is much smaller than it was in the LRS. This would result in a larger, and thus physically more reasonable value for l.

The model of a ruptured filament also contradicts the metallic conduction in the OFF state at very low temperatures found by *Jung et al.* [72] as discussed in chapter 2.1.2, because in the case of a ruptured filament, the semiconducting ruptured part of the filament would dominate, especially for low temperatures. Additionally, the distribution of the current density would be distributed uniformly over the whole electrode area, which contradicts the findings shown in figure 6.15(a).

Therefore a more plausible model for the HRS behaviour, is a conducting filament with a much smaller radius than in the LRS. In this case, the current density is localized as in the LRS, but the conduction (at room temperature) is mainly dominated by the semiconducting NiO surrounding the filament, in agreement with the measurements done by *Jung et al.* [72].

To estimate the cross-section of the filament in the HRS, the scaling behaviour of R_{OFF} together with equation (6.30) are used:

$$A_{cf} = \frac{\rho_{Ni}\rho_{NiO}d - R_{OFF}A\rho_{Ni}}{R_{OFF}(\rho_{NiO} - \rho_{Ni})} \approx 1 \cdot 10^{-19}\ \mathrm{m}^2, \tag{6.33}$$

Assuming a cylindrical filament this results in a filament diameter of $d_{cf} \approx 4 \cdot 10^{-10}$ m. This is approximately equal to the lattice parameter of metallic Ni $a_{Ni} = 3.52 \cdot 10^{-10}$ m.

Also a filament shape as would result from percolation, as discussed in chapter 2.1.2, with a HRS consisting of only some broken connections, but also still connected filaments, would explain the result discussed above.

Taking the above findings into account, the following scenario for the RESET process is plausible. When the current density within the conducting filament rises, the thermally activated dissolution of Ni into the surrounding NiO increases, as proposed by *Russo et al.* [148]. This will cause a rise in resistivity and temperature within the conducting filament. Because of the metallic conduction, the rise of temperature will increase the resistivity of the filament even more, such that the current will distribute over the whole film. This will cause a gradual drop in the total current, as typically observed in RESET IV curves (see figure 6.10). The filament(s) will cool down and a HRS with very thin metallic conductive filament(s) embedded in a NiO matrix remain(s) (see figure 6.14 and 6.17).

Apart from the scaling behaviour of the resistances of cells in the LRS, the HRS and in the pristine state, also the scaling behaviour of the *switching parameters* V_{SET}, I_{SET}, V_{RESET} and I_{RESET} are studied. Therefore, voltage sweeps as described above are performed on cells with different electrode areas and the voltage at which the SET processes (V_{SET}) and RESET processes (V_{RESET}) occur and the corresponding currents I_{SET} and I_{RESET} are read, as shown in figure 6.15(b) and (c).

For the RESET voltage (V_{RESET}) as well for the RESET current (I_{RESET}) no clear dependence on the electrode area can be observed. Because the LRS resistance is also constant for different electrode areas, there should exist a *critical voltage* and/or a critical current (or *critical current density* inside the conductive filament), which triggers the RESET process. This is in good agreement with the previous findings in chapter 6.4, where the dependencies of V_{RESET} and I_{RESET} on the R_{ON} are discussed.

Also for the SET process no clear dependence of the SET voltage V_{SET} on the electrode area is observed. The SET current I_{SET}, on the other hand, does show a significant dependence on the electrode area. However, if the SET current I_{SET} is divided by the corresponding electrode area a constant set current density j_{SET} is obtained, as shown in figure 6.15(d). This indicates the existence of a *critical SET current density* j_{SET} independent of the electrode area, which is needed to trigger the SET process (see figure 6.17). This will be studied in more detail in chapter 7.4

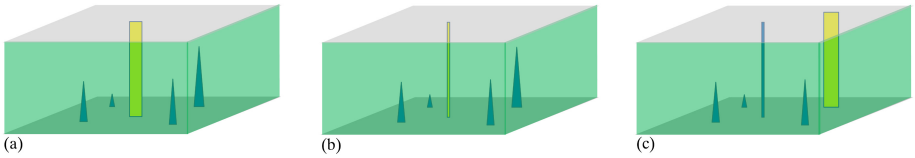

Figure 6.17: (a) LRS (ON state): the electrical properties are determined by one (or a few) dominating filament(s), (b) HRS (OFF state): after the RESET process (triggered by a critical current density through the dominating filament(s) (see chapter 6.4)) the main part of the total current at low voltages is carried by the very thin remains of the dominating filament(s), (c) Subsequent LRS: because of the metallic nature of the remains of the filament(s) in the HRS and the semiconducting nature of the surrounding NiO matrix, the current is distributed over the whole electrode at higher voltages (and temperatures). A new dominating filament(s) is (are) formed, triggered by a critical current density over the whole electrode.

To elucidate whether there exists a critical SET voltage V_{SET} to trigger the SET process, could be studied by similar experiments as described above on cells with different NiO film thicknesses. However, the rather complicated non-linear dependence of the resistance of the pristine cells $R_{Pristine}$ on the NiO film thickness, as described in chapter 5.4, makes it expendable to do so.

6.4.2 Pulsed resistive switching

For memory applications the dynamic switching properties are essential [90]. Therefore, fast resistive switching measurements, by means of fast voltage pulses are performed on the plug devices described in chapter 4.1 with a NiO film thickness of 10 nm and a round bottom plug with a diameter of 150 nm, in the configuration shown in figure 6.18(c). The device is connected in series to an external transistor to control the current flow through the device. Parasitic capacitances restrict the speed of the setup to SET- and RESET pulse lengths of 300 ns. The current through the device is measured by a oscilloscope (TDS 540C) which is connected parallel to the device.

Figure 6.18(a) presents a fast SET operation with a subsequent reading pulse. First, a voltage of 2.5 V is applied to the bit line (BL). The transistor is then opened for 300 ns by applying a voltage pulse to the word line (WL). The current rises instantly as indicated by the write current. The negative current peaks are due to parasitic effects caused by charging and discharging the BL and transistor capacities. With the subsequent read pulse the transistor is opened again and the loaded BL ($V = 0.1$ V) is discharged over the memory cell, which leads to a constant current of about 70 μA indicating that the cell is in the LRS

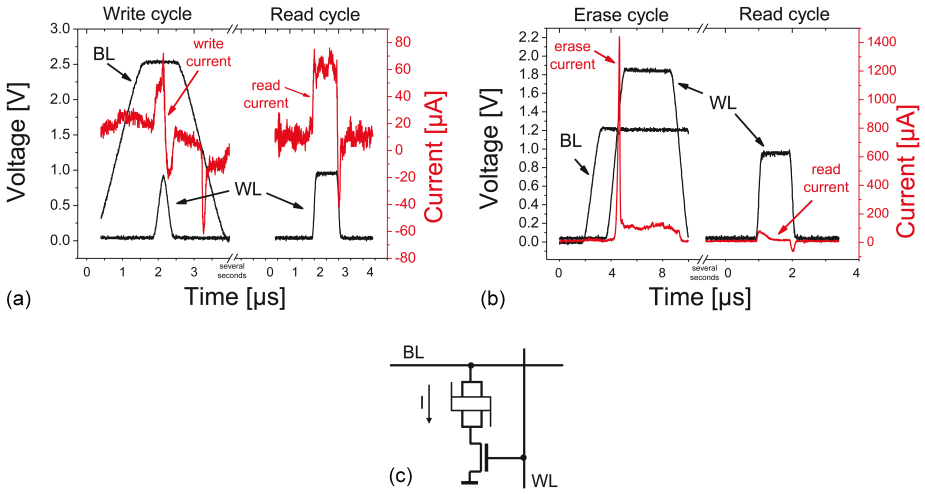

Figure 6.18: (a) Fast SET operation (Write cycle) with a subsequent reading pulse (Read cycle). (b) Fast RESET operation (Erase cycle) with a subsequent reading pulse (Read cycle). (c) The setup for fast pulse measurements [90].

with resistance value lower than 1 kΩ.

Figure 6.18(b) presents a fast RESET operation with a subsequent reading pulse. Now the BL is charged with 1.2 V. By applying a pulse to the WL the transistor is opened, leading to a very sharp current peak with a half width of 150 ns. Proof of switching is given by the following read pulse. The measured current is below the noise level of 10 μA indicating a resistance of the cell larger than 10 kΩ. The observed switching speeds for SET and RESET are within the limits of the setup. Preliminary results utilizing an advanced low-parasitic setup indicate the capability of much faster operation even in the ns-range. This is consistent with data published by other groups [4, 13].

Filament scaling

By varying the pulse amplitudes used for the SET processes, the filament size can be scaled. This has an effect on the resistance of the LRS. To elucidate this dependence, rectangular SET pulses of 3 V are applied for 3 ns. Afterwards, the resistance of the cell is read with a pulse of 100 mV. If the cell is still in the HRS, a pulse of 3.1 V is applied for 3 ns and the resistance of the cell is read again. In this way, the SET pulse amplitudes are stepwise increased by 100 mV until the cell switches from a HRS $>$ 10 kΩ to a LRS $<$ 1 kΩ.

Figure 6.19(a) shows the dependence of the resistance of the LRS (R_{ON}) on the current amplitude during the final SET pulse, represented by box-plots.

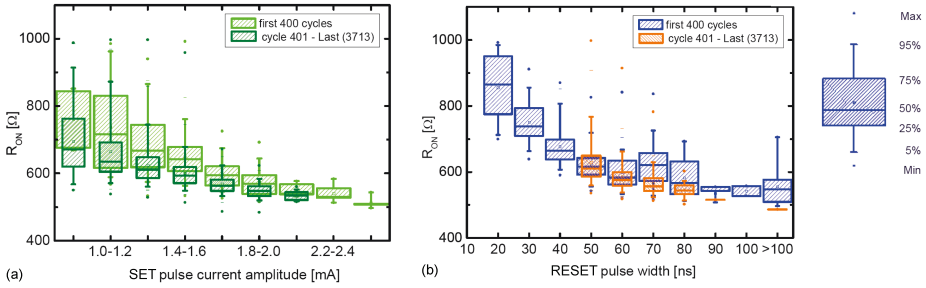

Figure 6.19: (a) The dependence of the resistance of the LRS (R_{ON}) on the current amplitude of the preceding SET pulse. (b) RESET pulse width needed to reset a cell with varying LRS resistances R_{ON}.

The resulting R_{ON} increases with a decrease of the current amplitude during the SET pulse. This is in agreement with experiments performed by *Nardi et al.* [123], who used an integrated "on chip" transistor in series with the resistive switching cell to control the current during the SET pulses. In this publication, it is claimed that the formation of a conducting filament is preceded by a purely electronic conducting path during the SET process. The cross-section of this electronic ON state (A_{ef}) is assumed to be proportional to the current during the SET pulse (I_{SET}). Subsequently, this electronic ON state is converted into the conducting filament by the oxygen vacancy concentration or increasing the Ni content. Therefore, the cross-section of the conductive filament (A_{cf}) is assumed to be close to the cross-section of the purely electronic conducting path. Hence the following correlations are obtained [123]:

$$R_{ON} \propto \frac{1}{A_{cf}} \sim \frac{1}{A_{ef}} \propto \frac{1}{I_{SET}}, \tag{6.34}$$

which accounts for the observed relation between I_{SET} and the resulting R_{ON}.

The filament cross-sections (A_{cf}) corresponding to different R_{ON} have an effect on the pulse width needed to switch the cell back to the HRS again. To elucidate this dependence, rectangular RESET pulses of 1.4 V are applied for 10 ns. Afterwards, the resistance of the cell is read with a pulse of 100 mV. If the cell is still in the LRS, a pulse of 1.4 V is applied for 20 ns and the resistance of the cell is read again. In this way, the RESET pulse widths are stepwise increased by 10 ns until the cell switches from a LRS < 1 kΩ to a HRS > 10 kΩ. The resulting relation between the preceding R_{ON} and the finally required RESET pulse width is shown in the box-plot in figure 6.19(b). Apparently, the RESET pulse width needed to switch the LRS to the HRS increases with decreasing R_{ON}. *Cagli et al.* [29] explains this behaviour by the RESET model earlier described in chapter6.4. Using equation (6.21) giving the relation between the

RESET time τ_{RESET} and the filament diameter ϕ the following relation is obtained:

$$R_{ON} \propto \frac{1}{\phi^2} \propto \frac{1}{\tau_{RESET}}. \tag{6.35}$$

Endurance and retention

In order to address the reliability topics, measurements of the switching and retention stability at room temperature as well as at elevated temperatures are performed. Figure 6.20(a) shows the resistive switching of a device which is switched 1000 times. While the bottom plug is grounded, unipolar switching pulses of $V_{SET} = 2.5$ V and $V_{RESET} = 1.2$ V were applied on the top electrode for 0.5 μs and 5 μs, respectively, to switch the cell between the LRS and the HRS. The resistance is subsequently read with $V_{read} = 0.1$ V. The result shows no significant influence of the switching pulses on the resistances of the LRS and only some variations on the resistances of the HRS at a higher number of cycles. Very important for the application is a clear resistance window between the LRS and HRS enabling a clear identification of the resistance states. Here, R_{OFF}/R_{ON} ratios ≥ 40 are found.

In addition to the endurance measurements the retention after cycling (RAC) is investigated. Therefore, the cycling procedure between LRS and HRS, as described above, is interrupted after the 500^{th} cycle with the cell in HRS. Subsequently, the resistance is repeatedly read for more than 0.5 hours. After that, the cell is switched back to the LRS and read again for more than 0.5 hours. As can be seen in figure 6.20(b) the resistances in both HRS and LRS remain stable. Subsequently, at least 500 additional switching cycles could be performed resulting in the same resistance states as observed before.

Furthermore, accelerated retention tests were conducted for more than 10^4 seconds at different temperatures from room temperature up to 110 °C. Six different test runs performed on the same cell are plotted in figure 6.20(c). Reprogramming was done for each test-run using the same voltage pulse scheme as for the endurance tests described above. The LRS exhibits a very good stability over time, also at elevated temperatures. The resistance increases with increasing temperature, showing the metallic conductivity of the LRS. The HRS also exhibits an acceptable stability in time and temperature. No drift is observed and a sufficient R_{OFF}/R_{ON} ratio of more than 100 remains even for long retention times.

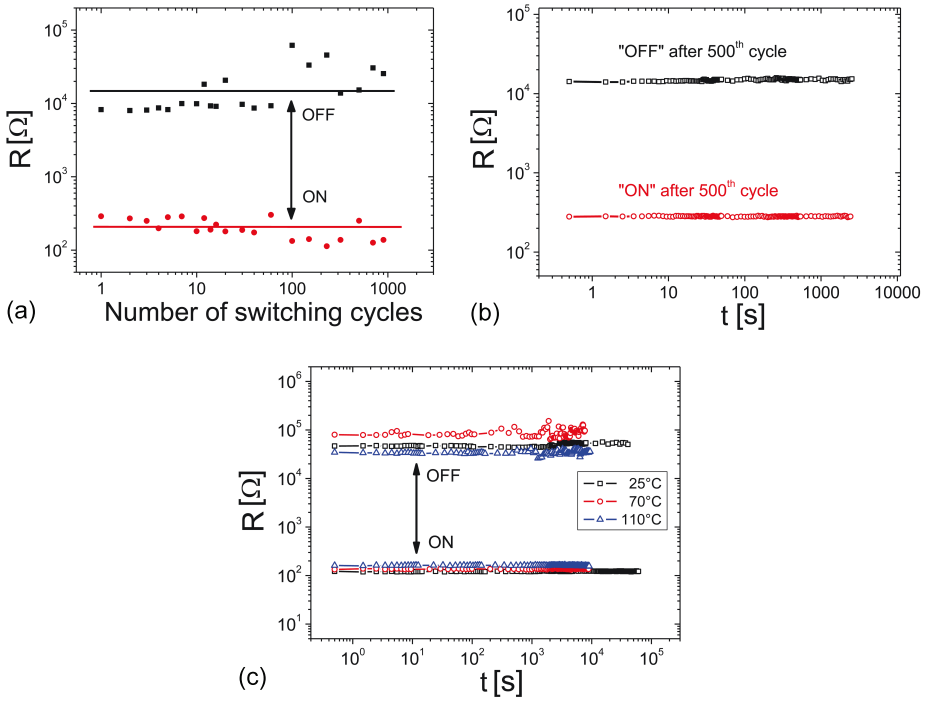

Figure 6.20: (a) Endurance measurement of a NiO cell with 1000 switching cycles. (b) The procedure was interrupted after 500 switching cycles for a retention measurement, where first the HRS is read for 2400 s, second the cell is switched to LRS and read for 2400 s. Finally the switching procedure could be continued for at least another 500 cycles. (c) Retention measurements of the HRS and LRS at 25 °C, 70 °C and 110 °C [90].

7

Potentiostatic breakdown analysis

Before NiO-based resistive switching devices exhibit the ability of switching between a HRS and LRS, a preceeding *forming process* is needed. During this forming process a high voltage is applied to the device, which results in its first dielectric breakdown. To prevent destruction of the device (hard dielectric breakdown), an appropriate current compliance is set. Therefore the forming process is also referred to as *soft dielectric breakdown*. During this process presumably the first filament(s) are formed and the device is "converted" from a leaky capacitor into a resistive switching device. In order to get a better insight into the resistive switching mechanism, it is essential to study this first soft dielectric breakdown in detail to understand the formation and the physical nature of the filament(s), which are presumably responsible for the resistive switching phenomena described in the previous chapter.
In this chapter the detailed characterization and analysis of the forming process in Pt/(Ni)/NiO/Pt memory devices under constant voltage stress and at elevated temperature conditions are discussed. Statistical dielectric breakdown analysis is a widespread testing approach in industrial studies to achieve lifetime predictions and material comparison for devices, e.g., capacitors and transistors [27, 171, 57]. Simultaneously, the scientific community developed numerous physical statistical models to understand the mechanisms of dielectric breakdown [28, 40, 167].
In the first paragraph, general statistical concepts of breakdown phenomena are discussed. Then, breakdown (forming) in the nano devices under constant voltage stress conditions and at different elevated temperatures are discussed, followed by equivalent studies performed on micro devices. Finally, the results on both device types are compared with each other and interpreted.

7.1 Reliability analysis

The intention of the electroforming experiments performed in this chapter is to correlate the experimentally determined statistical breakdown parameters

with possible models for dielectric breakdown. The understanding of the physical mechanisms behind the breakdown process and the physical (and chemical) nature of the formed filament(s) are essential for the understanding of the resistive switching phenomena. The *time-to-breakdown* (or *forming time*) measured on devices under constant voltage stress conditions is generally a statistically distributed quantity [28, 40, 167]. To obtain the characteristic breakdown parameters on base of such experiments, usually an analysis by means of *Weibull statistics* is carried out.

The Weibull distribution is a continuous probability distribution first applied by *Rosin and Rammler* in 1933 to describe the size distribution of particles [146]. The probability density function of a Weibull random variable t is given by

$$f(t;\tau,\beta) = \begin{cases} \dfrac{\beta}{\tau}\left(\dfrac{t}{\tau}\right)^{\beta-1} e^{-\left(\frac{t}{\tau}\right)^{\beta}} & t \geq 0, \quad (7.1) \\ 0 & t < 0, \quad (7.2) \end{cases}$$

where $\tau > 0$ is the scale parameter and $\beta > 0$ is the shape parameter, which describes the statistical spread of the distribution. The Weibull distribution describes a number of other probability distributions, e.g., the exponential distribution with $\beta = 1$ and the Rayleigh distribution with $\beta = 2$.

The cumulative Weibull distribution function is given by

$$F(t;\tau,\beta) = \begin{cases} 1 - e^{-\left(\frac{t}{\tau}\right)^{\beta}} & t \geq 0, \quad (7.3) \\ 0 & t < 0, \quad (7.4) \end{cases}$$

with breakdown rate h given by

$$h(t;\tau,\beta) = \begin{cases} \dfrac{\beta}{\tau}\left(\dfrac{t}{\tau}\right)^{\beta-1} & t \geq 0, \quad (7.5) \\ 0 & t < 0, \quad (7.6) \end{cases}$$

In the studies performed in this work the variable t stands for a *time to breakdown* or *forming time* and $F(t;\tau,\beta)$ describes a function of the device population in which dielectric breakdown occurred before the time t. The shape parameter β can then be interpreted as follows:

- $\beta < 1$ indicates that the breakdown rate is decreasing with time. This happens if the defective items experience breakdown early and are weeded out of the population in the beginning and after that the breakdown rate decreases over time. This suggests extrinsic breakdown causes, e.g. process-induced defects causing "weak spots" in the oxide.
- $\beta = 1$ indicates a constant breakdown rate with time. This suggests that the devices experience breakdown caused by random events.

- $\beta > 1$ indicates that the breakdown rate increases with time. This means that the devices are more likely to fail with time because of a "wear out" process, e.g., an increasing defect density during the voltage stress conditions.

The scale parameter τ represents a *characteristic breakdown time* or *characteristic forming time* in this case and stands for the time after which 63.2 % of the devices have experienced dielectric breakdown.

To determine the Weibull parameters mentioned above, commonly the *Weibull plot* is used. Here $\ln(-\ln(1-F))$ is plotted versus $\ln(t)$ which yields a straight line with slope β.

$$\ln(-\ln(1-F)) = \beta \ln(t) - \beta \ln(\tau) \tag{7.7}$$

τ is then determined by the point of intersection with the x-axis.

7.2 Forming in nano devices

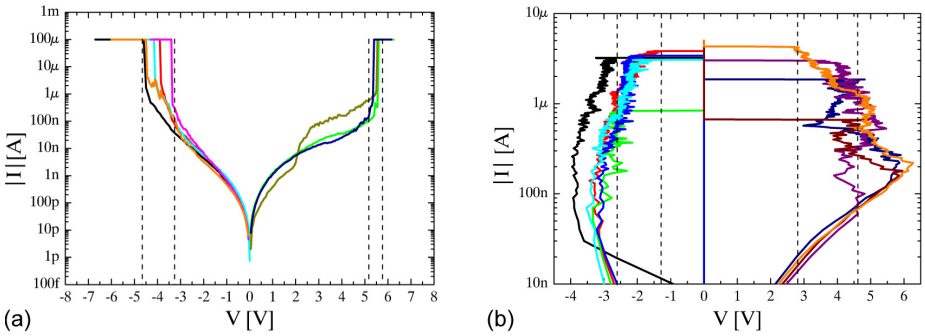

Figure 7.1: The forming of 8 nano devices with 25 nm NiO film thickness in the voltage-controlled (a) and of 8 nano devices with 25 nm NiO film thickness in the current-controlled mode (b). For comparison both are plotted with current $|I|$ on the ordinate and voltage V on the axis of abscissa.

Forming can be performed in a voltage-controlled or a current-controlled mode, as shown for nano devices with 25 nm NiO film thickness (see chapter 4.2) in figure 7.1(a) and (b), respectively. In the voltage-controlled mode, the voltage is swept from 0 V up to the required forming voltage with a voltage step size of 50 mV and a delay time of 250 ms, while the current response is measured simultaneously. To prevent permanent breakdown a current compliance of 100 μA is set. This is done for positive as well as negative voltage polarity on the top electrode. The bottom electrode is always kept on ground. All measurements are performed at room temperature in air. What stands out is the fact, that

for positive polarity higher forming voltages and/or longer forming times are needed to accomplish forming than for negative polarity.

In the current-controlled mode (figure 7.1(b)), current is swept from 10 nA up to the required forming current with a current step size of 10 nA and a delay time of 500 ms, while the voltage drop over the device is measured simultaneously. During the forming process the resistance of the device drops abruptly, which causes the abrupt voltage decrease. Also in the current-controlled mode it is observed that higher voltages and/or longer times are required for the forming process at positive polarities in contrast to negative polarities.

Comparing both modes, no significantly different characteristic is observed whether the voltage- or the current-controlled mode is chosen for forming.

The disadvantage of voltage- or current *sweeps* for physical investigations is the fact, that while the voltage or current is changed also the time during the forming process is progressing, so that two parameters are changing simultaneously. To get more physical insight into the polarity dependence of the forming process, forming experiments with constant voltage stress are performed and the current responses over time are measured.

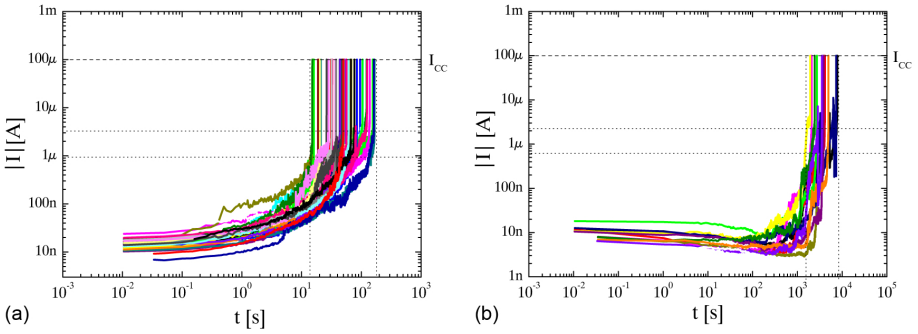

Figure 7.2: (a) The current responses of a number of nano devices with 100 nm x 100 nm top electrodes and a NiO film thickness $d = 25$ nm to a constant voltage stress of $V = -3$ V (a) and $V = +3$ V (b) measured over time t. All measurements are performed at room temperature in air.

Figure 7.2(a) and (b) show the current responses of a number of nano devices with 100 nm x 100 nm top electrodes and a NiO film thickness $d = 25$ nm to a constant voltage stress of $V = -3$ V and $V = +3$ V, respectively, measured over time t. All measurements are performed at room temperature in air. To prevent permanent breakdown a compliance current of $I_{CC} = 100$ μA is set in both cases. It can be clearly seen that on average the *forming times* at $V = +3$ V (figure 7.2(a)) are about two orders of magnitude longer than those needed at $V = -3$ V (figure 7.2(b)).

Furthermore, not only the forming times differ for the both polarities, but also the *forming characteristic* is different depending on the voltage polarity. Im-

mediately after the application of the negative voltage stress the currents start rising, as expected, indicating a stress induced degradation of the devices until degradation reaches a critical point at which the devices experience a soft dielectric breakdown. On the other hand, after the application of positive voltage stress the current first *decreases* before degradation and soft dielectric breakdown at a critical point is observed again, as in the case of negative voltage stress. This might indicate, that there exist different forming mechanisms for negative and positive polarity, or the interference of various processes which can occur under stress conditions, e.g., redistribution of mobile ions and degradation. This will be investigated more deeply in chapter 8.

Further, a wide spread in forming times is observed. To analyze this stochastic behaviour the Weibull statistic, as described in chapter 7.1 is used. Figure 7.3(a) shows the *Weibull plots* (see chapter 7.1) for the forming times for $V = -2$ V, -2.25 V, -2.5 V, -2.75 V, -3 V and figure 7.3(b) for $V = +3$ V, +4 V, +4.5 V, +5 V, measured in air at room temperature on nano devices with a NiO film thickness of 25 nm and 100 nm x 100 nm top electrodes.

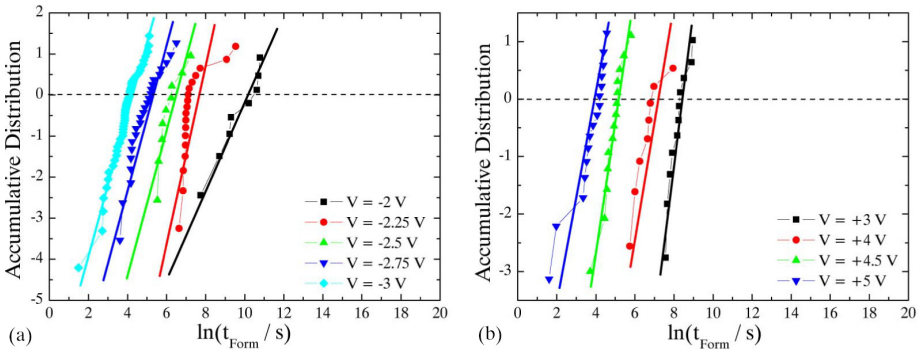

Figure 7.3: Weibull plots of the forming times of nano devices with a NiO film thickness of 25 nm and 100 nm x 100 nm top electrodes under negative voltage stresses (a) and positive voltage stresses (b). The measured forming times are represented by the symbols, the linear fits are represented by the solid lines. All measurements are performed in air at room temperature.

The slopes of the Weibull plots are 1.1, 3.5, 1.7, 1.5, 1.7 for the forming at negative voltages and 2.2, 1.4, 2.3, 1.6 for the positive voltages, respectively. Both the slopes for the negative as well as the slopes for the positive voltages are all larger than 1. This means, that the forming in the nano crossbar devices for both negative as well as positive voltages is an intrinsic process. According to the results discussed in chapter 6, the voltage in the pristine samples mainly drops across the bulk NiO rather than at the interfaces between the electrodes and NiO film. Therefore, forming in nano crossbar devices is mainly related to the degradation properties of the NiO film.

The *characteristic forming times* (see chapter 7.1) for each voltage stress are

found by the point of intersection of the linear fit of the measured forming times with the axis of abscissa. The characteristic times found are 68 s, 194 s, 622 s, 1492 s and 26588 s, for -3 V, -2.75 V, -2.5 V, -2.25 V and -2 V, respectively for negative voltage stresses, and 63 s, 170 s, 1266 s and 5008 s for +5 V, +4.5 V, +4 V and +3 V, respectively for positive voltage stresses. Clearly visible is the trend of shorter characteristic forming times for higher voltage stress for negative as well as positive voltages.

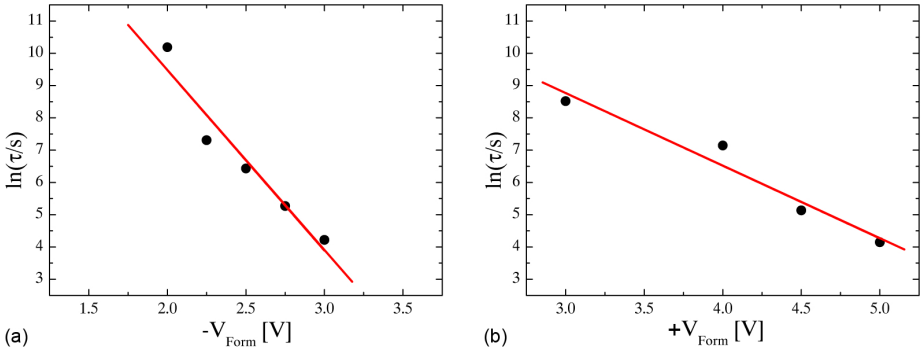

Figure 7.4: The characteristic forming times as a function of the applied voltage stresses for negative voltages (a) and positive voltages (b).

The relation between applied voltage stress and characteristic forming time for negative as well as positive voltages is shown in figure 7.4. Apparently, the characteristic forming time depends exponentially on the applied voltage stress. For negative and positive voltage stress a slope of -5.6 and -2.2 are found, respectively.

The difference of more than a factor of two between negative and positive voltage stress indicates a different forming mechanism for negative and positive voltages, or a superposition of two or more forming mechanisms, e.g., ion migration in the bulk [166, 165] and/or at grain boundaries [135], bond breaking [106, 108, 107], decomposition [68] by means of solid state electrolysis [134], redistribution of defects in the high electric field [110, 121, 183], evolution of gases at interfaces [164], that in case of negative voltage polarity support each other while they counteract the degradation at positive polarity.

Another reason for this asymmetry could also be found in the Ni adhesion layer used at the top electrode of the nano devices. This layer could enhance or suppress the growth (or nucleation) of a filament from the top electrode to the bottom electrode or vice versa.

7.3 Forming in micro devices

To investigate the influence of the Ni adhesion layer in the nano devices on the electroforming process, the same constant voltage stress experiments as discussed in the previous paragraph are performed on micro devices without Ni adhesion layer (see chapter 4.3) in this chapter. The selected electrode size is 50 μm $\times$ 50 μm, while the NiO film thickness is 25 nm. The applied voltages are $V = -1.8$ V, -1.9 V, -2 V and -2.1 V for negative polarity and $V = +2.25$ V, +2.5 V, +2.75 V and +3 V for positive polarity. All measurements are performed at room temperature in air.

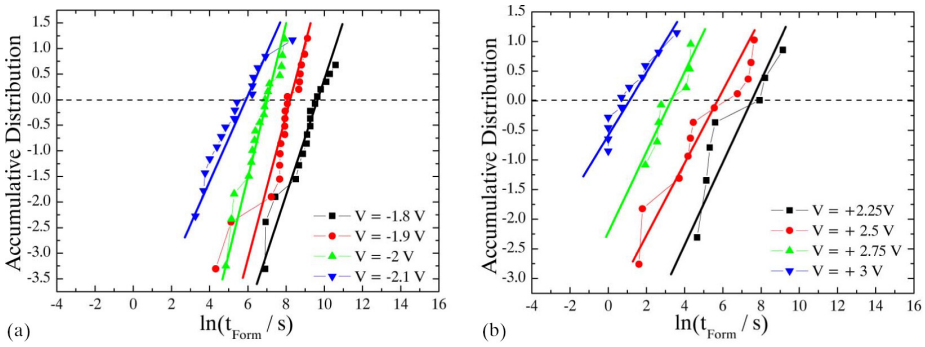

Figure 7.5: Weibull plots of the forming times of 50 μm $\times$ 50 μm micro devices under negative voltage stresses (a) and positive voltage stresses (b). All measurements are performed at room temperature in air. The measured forming times are represented by the symbols, the linear fits are represented by the solid lines.

Figure 7.5 shows the Weibull plots of these measurements. The found slopes of the Weibull plots are 0.98, 0.89, 1.25 and 0.68 for negative voltages, respectively, and 0.54, 0.50, 0.69 and 0.49 for positive voltages, respectively. Unlike the Weibull slopes for the nano devices, these Weibull slopes are around or even below 1. This means that the forming behaviour in micro devices is of *extrinsic* nature. This can be explained by the much bigger electrode size of a factor of 250000 compared with the electrode size of the nano devices. Therefore, the probability of finding a process induced weak spot, e.g., local chemical inhomogeneities in the NiO, macroscopic defects, local inhomogeneities in NiO film thickness that increase the effective field strength, is much higher in the micro devices, causing the extrinsic forming behaviour [40].

The *characteristic forming time* for each voltage stress is found by the point of intersection of the linear fit of the measured forming times with the axis of abscissa. The characteristic times found are 403 s, 1152 s, 4524 s and 17202 s, for -1.8 V, -1.9 V, -2.0 V and -2.1 V, respectively for negative voltage stresses, and 2.63 s, 27.9 s, 417 s and 1808 s for +3 V, +2.75 V, +2.5 V and +2.25 V,

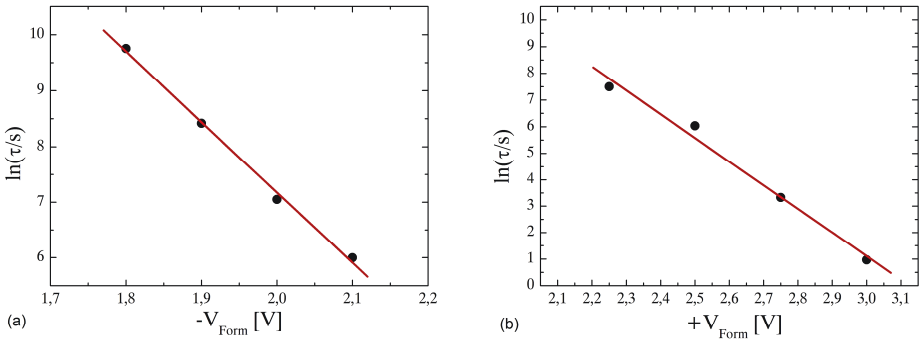

Figure 7.6: The characteristic forming times of the micro devices as a function of the applied voltage stresses for negative voltages (a) and positive voltages (b).

respectively for positive voltage stresses. Clearly visible is the trend of shorter characteristic forming times for higher voltage stress for negative as well as positive voltages.

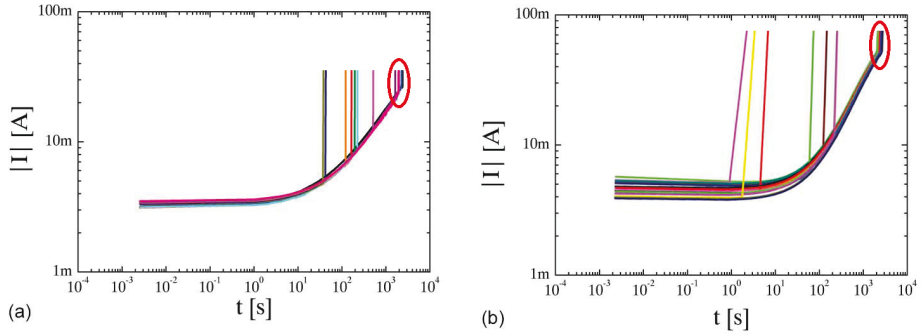

Figure 7.7: The forming characteristic of a number of micro devices under a constant voltage stress of $V = -1.5$ V at $T = 354$ K (a) and under a constant voltage stress of $V = +2.5$ V at $T = 340$ K (b).

The relation between applied voltage stress and characteristic forming time for negative as well as positive voltages is shown in figure 7.6. Apparently, the characteristic forming time depends exponentially on the applied voltage stress. For negative and positive voltage stress a slope of -12.6 and -8.9 are found, respectively. The difference in the slopes found for the nano- and micro devices can be explained by the fact that the characteristic times measured for the micro devices are related to extrinsic breakdown of the devices, in contrast to the intrinsic breakdown measured in the nano devices. Nevertheless, like in case of the nano devices, the slope found for the micro devices for negative voltage stress is much larger than the slope for positive voltage stress.

Also the difference in the *forming characteristic* during the forming process with negative and positive polarity, as shown in figure 7.7, are very similar to those observed in the forming characteristic of the nano devices with Ni adhesion layer: an immediate degradation of the resistance for negative voltages and a initial increase of the resistance followed by a degradation of the resistance for positive voltages. Therefore, the Ni adhesion layer in the nano devices can not be the (only) reason for the different forming behaviour for negative and positive voltages.

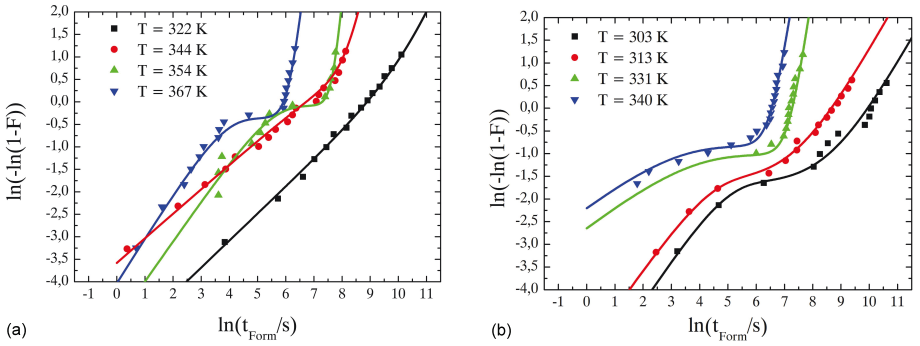

Figure 7.8: Weibull plots of the forming times of 50 μm $\times$ 50 μm micro devices under a constant negative voltage stress of $V = -1.5$ V at elevated temperatures (a) and a constant positive voltage stress of $V = +2.5$ V at elevated temperatures (b). The measured forming times are represented by the symbols, the fits are represented by the solid lines. Note the extrinsic regions with a shallow slope and the intrinsic regions with a steep slope.

What further catches the eye in figure 7.7 (a) and (b) is the fact that at *elevated temperatures* an extrinsic *and* an intrinsic behaviour is observed, identified by the occurrence of random forming events at shorter times and an agglomeration of forming events around the characteristic intrinsic forming times, as indicated by the red circles in figure 7.7 (a) and (b). This becomes more clear in the Weibull plots for forming at $V = -1.5$ V (figure 7.8 (a)) and $V = +2.5$ V (figure 7.8 (b)) at elevated temperatures. The extrinsic regions are identified by flat slopes at shorter forming times, followed by the intrinsic region identified by steep slopes at higher forming times.

To analyze these competing Weibull distributions, the following analytical formula for the probability lifetime density function $f(t)$ proposed by *Degraeve et al.* is used to fit such a bimodal distribution [40]:

$$f(t) = p \cdot f_e(t) \cdot R_i(t) + p \cdot f_i(t) \cdot R_e(t) + (1 - p) \cdot f_i(t), \tag{7.8}$$

with $R_i(t)$ and $R_e(t)$ the intrinsic and extrinsic reliability functions, respectively,

V [V]	T [K]	p [ ]	$\tau_{intrinsic}$ [s]	$\tau_{extrinsic}$ [s]	$\beta_{intrinsic}$ [ ]	$\beta_{extrinsic}$ [ ]
−1.5	322	0.8	18300	6400	1.5	0.6
−1.5	344	0.85	2977	500	3.0	0.55
−1.5	354	0.6	2150	130	6.5	0.9
−1.5	367	0.5	470	28	5.0	1.0
+2.5	303	0.17	25000	102	1.1	0.95
+2.5	313	0.18	7000	56	1.1	0.90
+2.5	331	0.3	1600	52	4.1	0.50
+2.5	340	0.35	800	8	3.9	0.50

Table 7.1: The results of the fitting of the bimodal cumulative Weibull distributions at elevated temperatures using the analytical formula for the probability lifetime density function $f(t)$ proposed by *Degraeve et al.* [40].

$$R_{i,e}(t) = 1 - F_{i,e}(t). \tag{7.9}$$

The reliability function gives the fraction of the population that survives after a certain stress time t. The factor p is the population fraction that can fail either extrinsically or intrinsically (defective part), while $(1 - p)$ is the population fraction that can only fail intrinsically (defect-free part).

The corresponding cumulative Weibull distribution function $F(t)$ is then given by

$$F(t) = \int f(t)dt = p \cdot R_i(t)F_e(t) + F_i(t), \tag{7.10}$$

with

$$F_{i,e}(t) = 1 - e^{-(\frac{t}{\tau_{i,e}})^{\beta_{i,e}}}. \tag{7.11}$$

The results of the fitting of $ln(-ln(1 - F(t)))$ vs $ln(t_{Form}/s)$ to the measured values are shown by the solid lines in figure 7.8 and the found parameters are summarized in table 7.1.

From the results summarized in table 7.1, clearly the trend for increasing forming times for decreasing forming temperatures is observed. This dependence is found to be exponential versus the inverse forming temperature, as shown in figure 7.9 for the extrinsic mode and in figure 7.10 for the intrinsic mode. Here, the natural logarithm of the characteristic forming times $\ln\tau_{i,e}$ found in table 7.1 are plotted against the inverse temperature $1/T$ at which the forming is performed.

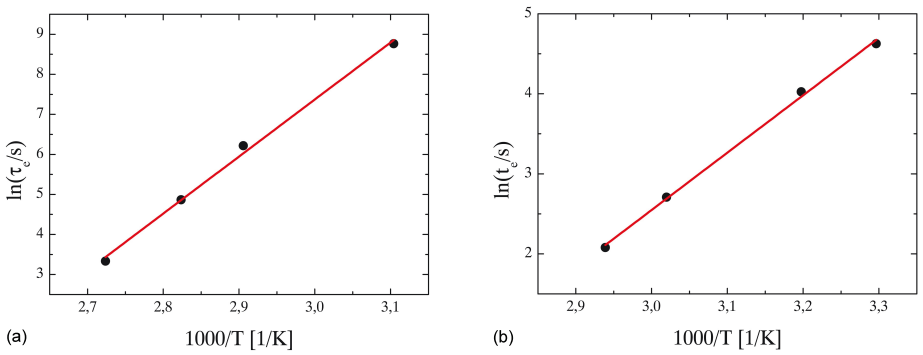

Figure 7.9: Arrhenius plots of the characteristic extrinsic forming times of the micro devices during a constant negative voltage stress of $V = -1.5$ V (a) and a positive voltage stress of $V = +2.5$ V (b).

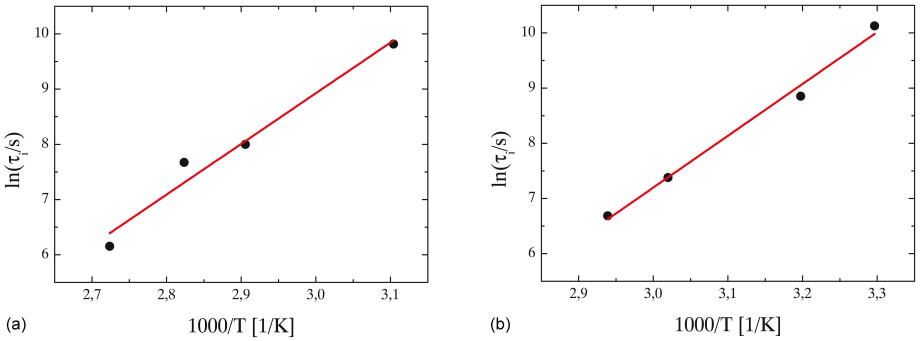

Figure 7.10: Arrhenius plots of the characteristic intrinsic forming times of the micro devices during a constant negative voltage stress of $V = -1.5$ V (a) and a positive voltage stress of $V = +2.5$ V (b).

The slopes determined for the extrinsic mode are $1.4 \cdot 10^4$ for negative voltage stress of $V = -1.5$V and $7.2 \cdot 10^3$ for positive voltage stress of $V = +2.5$V. For the intrinsic mode a slope of $9.2 \cdot 10^3$ is found for negative voltage stress of $V = -1.5$V and $9.4 \cdot 10^3$ for positive voltage stress of $V = +2.5$V. Apparently, the slopes of the intrinsic mode of the forming process are independent of the applied voltage stress polarity. On the other hand, the slope for the extrinsic mode at negative voltage stress is twice the value of the slope for the extrinsic mode at positive voltage stress. This indicates a different forming mechanism for negative and positive voltage stress in the extrinsic forming mode, or a different superposition of two or more forming mechanisms (see chapter 7.2).

7.4 Conclusions

The comparison between the Weibull slopes of the micro- and nano devices shows, that the nano devices show an intrinsic and the micro devices an extrinsic forming behaviour at room temperature. This is explained by the much bigger electrode area of the micro devices which increases the probability of fabrication-induced defects under the electrode area, that lead to the extrinsic behaviour.

At elevated temperatures the micro devices show extrinsic as well as intrinsic forming behaviour. The higher the temperature, the more dominant the intrinsic mode becomes. The intrinsic mode is found to be independent of the voltage polarity.

The determination of the slopes of the characteristic forming times as a function of the applied voltage stress reveals, that the forming processes at negative voltages have a much larger slope than the forming at positive voltages for the intrinsic mode and the extrinsic mode, as well as in the nano- and micro devices, respectively. Therefore, the Ni-adhesion, which is lacking in the micro devices, can not be the cause for the asymmetry in the forming voltage polarity, instead there must be a more general cause which the nano- and micro samples both have in common.

A possible scenario that explains this asymmetry involves the ambient atmosphere around the devices. By applying a negative voltage on the top electrode (see figure 7.11(a)) a strong electrical field is generated over the NiO film. This strong field leads to a drift of the Ni^{+2} ions towards the negative top electrode and of the nickel vacancies V''_{Ni} towards the bottom electrode. The result of these drifts is a Ni^{+2} enrichment at the top electrode and an Ni^{+2} depletion at the bottom electrode (red colour in figure 7.11(a)). Because NiO is naturally non-stoichiometric in favor of more oxygen than nickel (see chapter 2.2.4), the Ni^{+2} enrichment at the top electrode would result in a stoichiometric NiO layer at the top electrode with high resistivity.

However, for the description of the electroforming in air one has to consider that the polycrystalline Pt electrodes are permeable for oxygen [98]. Especially, Pt can decompose oxygen gas molecules into oxygen atoms by means of chemisorption of oxygen atoms on the surface [98]. Oxygen gas molecules can form the chemisorbed states by the following reaction:

$$\frac{1}{2}O_{2(g)} + V_{ad} \rightarrow O_{ad}, \tag{7.12}$$

where V_{ad} and O_{ad} are a vacant adatom site and an oxygen adatom, respectively. Then the oxygen adatoms can compensate the additional Ni^{+2} at the top electrode according to the following reaction:

$$O_{ad} \rightarrow O_O^{\times} + V_{ad}. \tag{7.13}$$

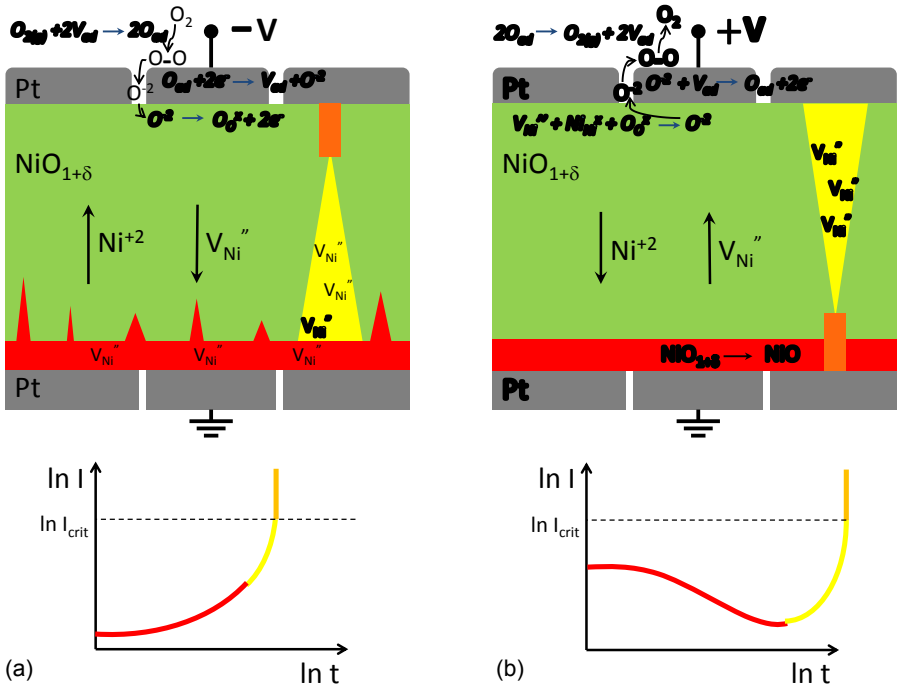

Figure 7.11: Schematic representation of the reactions and drifts of the particles involved in the forming process under negative voltage stress (a) and positive voltage stress (b). Below the affiliated forming characteristics are sketched. The colours in the forming characteristics represent the different stages of the forming processes and correspond to the formation of the layers in the device sketched in the same colour.

This incorporation of ambient oxygen results in a (partial) compensation of the Ni^{+2} enrichment and will therefore prevent the formation of a stoichiometric, high ohmic NiO layer at the top electrode.

The Ni^{+2} depletion at the bottom electrode will result in a highly oxygen-rich NiO layer with a very low resistivity, which can not be compensated by oxygen out of the ambient atmosphere. For the forming characteristic, this results in an immediate resistance degradation after the application of the negative voltage at the top electrode (red part of the forming characteristic in figure 7.11(a))

Because such a layer naturally exhibits irregularities, the spots in this Ni^{+2} depletion layer that are closer to the top electrode will experience a field enhancement, resulting in a faster growth in this spot. In this way a highly oxygen-rich NiO filament will grow from the bottom towards the top electrode (yellow colour in figure 7.11(a)).

The growth of the filament will continue, until the field between the tip of the

filament and the top electrode reaches the dielectric breakdown field strength of the NiO. Then dielectric (soft) breakdown (by, e.g., bond breakage [106], thermal breakdown due to an increasing conductance by Joule heating [38]) will occur, resulting in a sudden increase of the current (orange colour). To prevent hard dielectric breakdown, a current compliance has to be set.

By applying a positive voltage on the top electrode (see figure 7.11(b)) a strong electrical field in opposite direction is generated, causing a drift of Ni^{+2} ions towards the bottom electrode and of nickel vacancies $V_{Ni}^{''}$ towards to positive top electrode. These drifts result in a Ni^{+2} enrichment at the bottom electrode and an Ni^{+2} depletion at the top electrode (red colour in figure 7.11(b)).

In this case, the Ni^{+2} enrichment at the bottom electrode results in a stoichiometric NiO layer at the bottom electrode with high resistivity, because it can not be compensated by ambient O_2. This results in the increase of the resistance of the device indicated by the red part of the forming characteristic and in the longer forming time in respect to forming at negative voltage polarity.

The Ni^{+2} depletion at the top electrode will result in highly oxygen-rich NiO regions with a very low resistivity, which can be (partially) compensated by oxygen out of the ambient atmosphere, directly at the top electrode interface (red colour). In this case the oxygen adatoms can react with the additional $V_{Ni}^{''}$ at the top electrode according to the following reaction:

$$V_{Ni}^{''} + Ni_{Ni}^{\times} + O_O^{\times} + V_{ad} \rightarrow O_{ad} + 2e^{-}. \tag{7.14}$$

However, in the bulk of the NiO more towards the bottom electrode, these highly oxygen-rich regions will still form. Because of its irregular nature, the spots that are closer to the bottom electrode will experience a field enhancement, enhancing the bond-breakage that generates more nickel vacancies $V_{Ni}^{''}$, resulting in a faster growth of this spot, which again results in a higher field enhancement. In this way a highly oxygen-rich NiO filament will grow towards the bottom electrode (yellow colour in figure 7.11(b)).

The growth of the filament will continue, until the field between the tip of the filament and the top electrode reaches the dielectric breakdown field strength of the NiO. Then the final (soft) dielectric breakdown will occur, resulting in a sudden increase of the current (orange colour). To prevent hard dielectric breakdown, a current compliance has to be set.

This scenario inhibits three processes involved in the forming process, that all enhance the drop of resistance in case of negative polarity, while they counteract each other in case of positive polarity, as indicated by the results of the Weibull analysis earlier in this chapter. This would explain the different characteristic current-voltage characteristics as well as the different forming times of the devices formed with positive and negative polarity.

If this scenario is correct, the dielectric breakdown (orange colour) should happen at the same critical field strength for both polarities, the *dielectric break-*

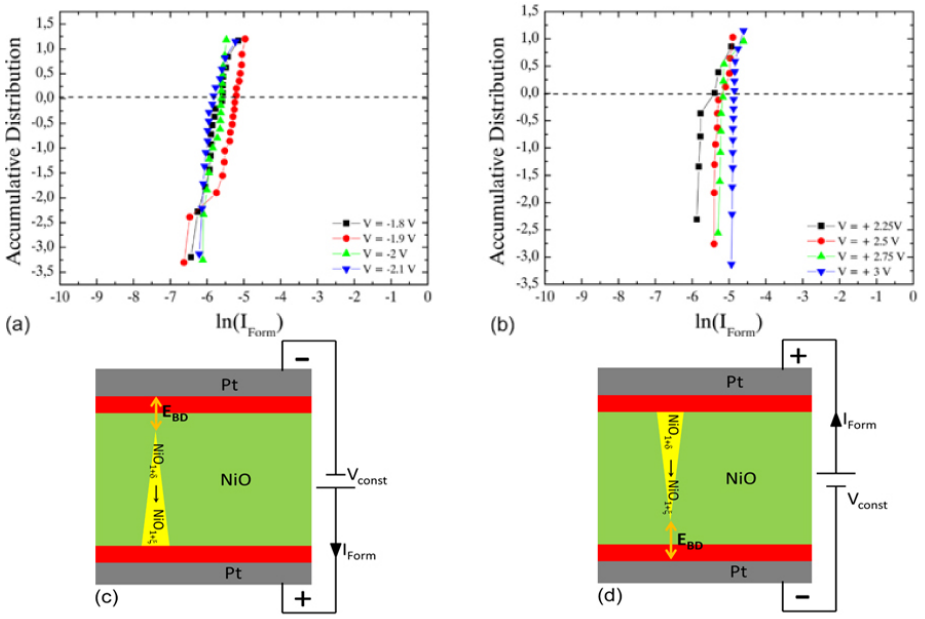

Figure 7.12: Weibull plots of the current I_{Form} at the moment of dielectric breakdown divided by the applied constant voltage V for negative voltages (a) and positive voltages (b) at room temperature. Note the voltage independent characteristic value for negative as well as positive voltages. (c) and (d) show a schematic representation of the resistive switching device under negative and positive voltage stress at the onset of the dielectric breakdown at which the steep increase in the forming characteristic takes place. Note the dielectric breakdown field strength E_{BD} between the tip of the conductive filament and the electrode.

down field strength of NiO. According to the Poole-Frenkel mechanism, which dominates the conductivity in NiO (see chapter 6.1.2), a constant electrical field is equivalent to a constant value for the current density j (see equation (6.2)). Figure 7.12 shows the Weibull plots of the current I_{Form} at the moment of dielectric breakdown for the different applied constant voltages V for negative (a) and positive polarities (b) at room temperature. Note the voltage independent characteristic value for $ln(I_{Form})$ for the negative as well as the positive voltages, which is in agreement with the above described scenario.

Using the forming currents I_{Form} found in figure 7.12 and taking the mean value for a conductive filament cross-sectional area $A_{CF} = 3.47 \cdot 10^{-17}$ m^2 found in chapter 6.4.1 yields an estimation for the current density j_{BD} between the conductive filament and the counter electrode at the onset of the steep increase in the forming characteristic:

$$j_{BD} = \frac{I_{Form}}{A_{CF}} \tag{7.15}$$

For the negative polarity a critical current density $j_{BD} = 1.15 \cdot 10^{14}$ A/m^2 and for positive polarity a critical current density $j_{BD} = 1.73 \cdot 10^{14}$ A/m^2 is found.

By the use of the Poole-Frenkel equation (6.2) mentioned in chapter 6.1.2 the dielectric breakdown field strength E_{BD} in these devices can be estimated:

$$j_{BD} = \sigma_0 E_{BD} \ \exp\left[\frac{-q\phi_{PF}}{2k_B T}\right] \ \exp\left[\frac{1}{2k_B T} \cdot \sqrt{\frac{q^3 E_{BD}}{\pi\varepsilon_0\varepsilon_r}}\right] \tag{7.16}$$

Inserting the values found in chapter 6.1.2 for micro devices; $\varepsilon_r = 13$, $\phi_{PF} = 600$ meV, $\sigma_0 = q\mu n_0 = 13$ A/V, and using the estimated values for j_{BD} yields a critical dielectric breakdown field strength of $E_{BD} = 5.4 \cdot 10^8$ V/m for negative and $E_{BD} = 5.8 \cdot 10^8$ V/m for positive polarities. These are in good agreement with the literature value of $E_{BD}^{NiO} = 6.6$ MV/cm for NiO ($\varepsilon_r = 13$) [106].

These E_{BD} correspond to a distance d_{BD} between the tip of the grown filament and the electrode of about $d_{BD} = V_{const}/E_{BD} = 4.3$ nm for an exemplary assumed applied constant voltage $V_{const} = 2.5$ V, which is plausible.

The small difference in E_{BD} between positive and negative polarity can be explained by the different stoichiometric composition at the interface at the top and bottom electrode, where the dielectric breakdown takes place.

Next to the different forming characteristics of the forming process induced by positive and negative voltage stress, which can be explained by this scenario, also the direction of the growth of the filaments in both cases should be noted. If the above described scenario is correct, an application of negative voltage stress on the top electrode results in a highly conductive filament growth from the bottom electrode towards the top electrode, which results in a dielectric breakdown of the NiO at the top electrode. Such a breakdown is always accompanied by heat generation which results in structural destruction of the crystal lattices, in this case at the top electrode. In case of application of positive voltage stress at the top electrode the dielectric breakdown and the accompanied structural destruction of the crystal lattices would take place at the bottom electrode.

Figure 7.13(a) and (c) show SEM images of the devices used for the Weibull analysis discussed earlier in this chapter. The devices formed with a positive voltage of $V = +2.25$ V on the top electrode figure 7.13(a) show a volcano-like structure of about 1 μm in diameter. These were found on 12 out of the 15 devices studied in SEM. The devices formed with a negative voltage of $V = -1.8$ V on the top electrode figure 7.13(c) show an elongated shaped structure of about 3 μm in length and 1 μm in width. These were found on all 15 out of the 15 devices formed under negative voltage studied in SEM.

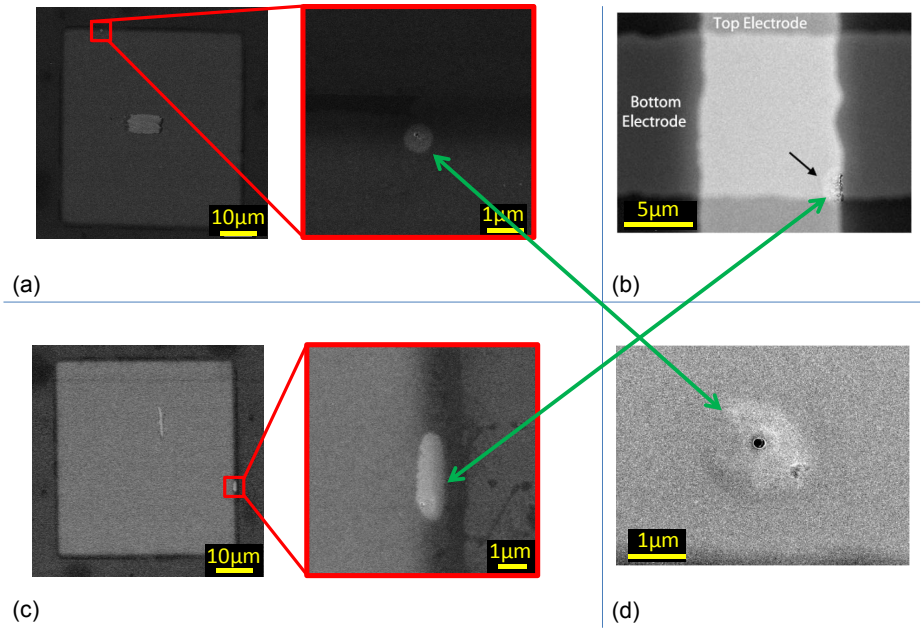

Figure 7.13: SEM images of Pt/NiO/Pt devices after forming with positive (a) and negative (c) voltage at the top electrodes used for the potentiostatic measurements described earlier in this work and SEM images of Pt/TiO_2/Pt devices formed with positive (b) and negative (d) polarity [164].

The group of *J. P. Strachnan et al.* [164] performed similar experiments on Pt/TiO_2/Pt devices. They observed very similar structures on their devices after forming with negative and positive voltage sweeps. But in contrast to the Pt/NiO/Pt devices studied in this work, the Pt/TiO_2/Pt devices show the volcano-like structures on the devices formed with negative voltage figure 7.13(d) and the elongated structures on the devices formed with positive voltage on the top electrode figure 7.13(b).

J. P. Strachnan et al. explain these structures by the localized electrochemical production of oxygen gas at one of the two TiO_2/metal interfaces. Taking into account, that NiO is a p-type material, which increases conductivity with increasing oxygen stoichiometry, while TiO_2 is a n-type material, which decreases conductivity with increasing oxygen stoichiometry, the conducting filaments which are assumed to grow in both materials during forming, would grow in *opposite* directions. In case of TiO_2 the filament is enriched with oxygen vacancies, while in case of NiO the filament is enriched with nickel vacancies or oxygen. This causes a dielectric breakdown and the accompanied structural destruction of the crystal lattices on the opposite electrodes if the same voltage

polarity is applied to a NiO- and TiO_2-based device. This scenario is in perfect agreement with the observed opposite behaviour of NiO and TiO_2.

All the observations and conclusions made in this chapter indicate a major influence of the ambient (air) atmosphere on the forming behaviour. Additionally, the fact that the volcano-like and the elongated structures are all observed at the edge of the electrodes, where the interaction with the ambient atmosphere is most likely, support this assumption. To elucidate this model, the influence of the ambient atmosphere on the forming process will be investigated in the next chapter. Especially, forming in oxygen conditions should be similar to the behaviour in air.

8

Influence of the ambient atmosphere

In the previous chapter it is found that the forming behaviour of the nano- as well as the micro devices exhibit an asymmetry depending on the polarity of the applied forming voltage. As discussed in the conclusions of the last chapter, this asymmetry might be explained by a superposition of the intrinsic forming mechanism in NiO with an interaction with the ambient air atmosphere at the top electrode. Therefore, in this chapter the influence of the ambient atmosphere on NiO resistive switching devices is investigated.

8.1 Potentiostatic forming in different ambient atmospheres

To verify the model proposed in the conclusions of the previous chapter, similar potentiostatic measurements as used for the Weibull statistics in the previous chapter are subsequently performed in vacuum, oxygen and air environment. In each ambient condition, new pristine samples are measured, to assure independent measurements. The measurements are performed on at least 5 samples per ambient condition and all showed qualitatively the same results. In figure 8.1 for each condition one example is shown.

Figure 8.1(a) and (d) show the forming characteristics of a 100 μm $\times$ 100 μm micro device with 25 nm NiO film thickness at $V = -1$ V and $V = +1$ V respectively under *vacuum* conditions ($p = 6.6 \cdot 10^{-7}$ mbar). Starting from the model proposed in the last chapter, forming in vacuum at positive constant voltage should result in the same forming characteristic as at positive voltage stress in air, because in both cases the outgassing of oxygen through the Pt top electrode is equally possible. On the other hand, figure 8.1(d) shows qualitatively the equal forming characteristic as of forming at negative voltage stress in air. The forming in vacuum conditions at *negative* constant voltage, shown in

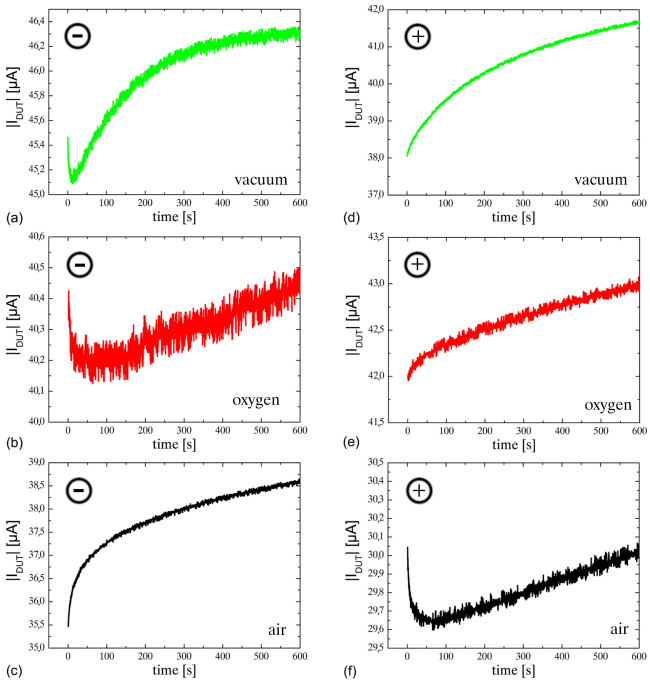

Figure 8.1: $I(t)$-plots of the forming behaviour of NiO cells in different ambient atmospheres at a constant voltage. The forming characteristics at a negative voltage of $V = -1$ V in vacuum ($p = 6.6 \cdot 10^{-7}$ mbar), in oxygen environment ($p(O_2) = 200$mbar) and in air are shown in (a), (b) and (c), respectively. The forming characteristics at a positive voltage of $V = +1$ V in vacuum, in oxygen environment ($p(O_2) = 200$ mbar) and in air are shown in (d), (e) and (f), respectively. The measurements are performed on micro devices with 100 μm $\times$ 100 μm electrode size and 25 nm NiO film thickness, at room temperature.

figure 8.1(a), shows the qualitatively same characteristic as the characteristic at *positive* constant voltage stress in air. In other words, the forming characteristics under negative and positive voltage stress in air are *mirrored*, when performed under vacuum conditions, which is not expected following the model proposed in the previous chapter.

Especially the forming characteristics under *oxygen* conditions ($p(O_2) = 200$ mbar) shown in figure 8.1(b) and (e) should qualitatively be equal to the forming characteristics in air, if the model proposed in the previous chapter is correct. According to this model, oxygen can be built into the device by application of negative voltage under both ambient conditions and oxygen can also be outgassed by application of positive voltage under both conditions. But, if figure 8.1(b) and (e) under oxygen conditions are compared with figure 8.1(c) and (f) in air,

again *mirrored* forming characteristics are observed.

Figure 8.1(c) and (f) show the forming characteristic at a constant voltage stress of $V = -1$ V and $V = +1$ V respectively, in *air*, after being in vacuum and oxygen conditions. Compared with the forming characteristics shown in the previous chapter for positive and negative constant voltage stress, similar forming characteristics are observed, as expected.

Therefore, the *oxygen* in the ambient atmosphere can *not* be held responsible for the differences in the forming characteristics at positive and negative constant voltage stress.

In another experiment, forming at negative and positive voltage stress was compared in vacuum, in water ambient atmosphere and in air, subsequently.

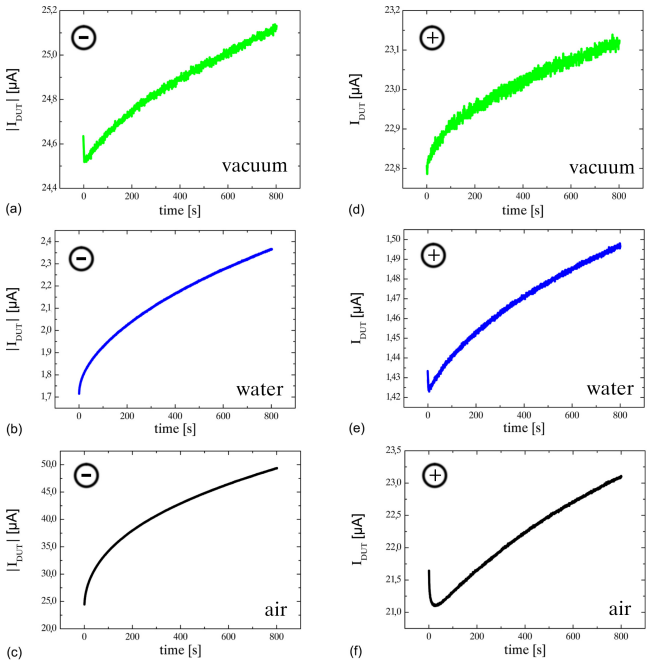

Figure 8.2: $I(t)$-plots of the forming behaviour of NiO cells in different ambient atmospheres at a constant voltage. The forming characteristics at a negative voltage of $V = -1.5$ V in vacuum ($p = 7.2 \cdot 10^{-7}$ mbar), at $V = -800$ mV in H_2O-environment ($p(H_2O) = 13$ mbar) and at $V = -1.5$ V in air are shown in (a), (b) and (c), respectively. The forming characteristics at a positive voltage of $V = +1.5$ V in vacuum ($p = 7.2 \cdot 10^{-7}$ mbar), at $V = +800$ mV in H_2O-environment ($p(H_2O) = 13$mbar) and at $V = +1.5$ V in air are shown in (d), (e) and (f), respectively. The measurements are performed on micro devices with 100 μm $\times$ 100 μm electrode size and 50 nm NiO film thickness, at room temperature.

Figure 8.2(a) and (d) show the forming characteristics of a 100 μm $\times$ 100 μm micro device with 50 nm NiO film thickness at $V = -1.5$ V and $V = +1.5$ V respectively under *vacuum* conditions ($p = 7.2 \cdot 10^{-7}$ mbar). As shown in the previous experiment, figure 8.2(d) shows qualitatively the equal forming characteristic as of forming at negative voltage stress in air. The forming in vacuum conditions at negative constant voltage, shown in figure 8.2(a), shows the qualitatively the same characteristic as the characteristic at positive constant voltage stress in air. Again, this is in contradiction to the predictions made by the model proposed in the previous chapter.

Figure 8.2(b) and (e) show the forming characteristics at a constant voltage stress of $V = -800$ mV and $V = +800$ mV respectively in *water* ambient atmosphere ($p(H_2O) = 13$ mbar). These forming characteristics show qualitatively equal dependencies on the applied constant voltage stress polarity as the forming characteristics in air, shown in figure 8.2(a) and (d). Therefore, it is likely that the *water* and not the oxygen in the air is responsible for different polarity dependent forming characteristics.

Figure 8.2(c) and (f) show the forming characteristic at a constant voltage stress of $V = -1.5$ V and $V = +1.5$ V respectively, in *air*, after being in vacuum and water ambient conditions. Compared with the forming characteristics shown in the previous experiment and previous chapter for positive and negative constant voltage stress, similar forming characteristics are observed, as expected.

Figure 8.3(a) shows the current responses to subsequently applied constant voltage pulses of $V = -1.5$ V with a pulse length of 100 seconds performed on a mirco device with 100 μm $\times$ 100 μm electrode size and 25 nm NiO thickness, at room temperature in *air*. The current response to the first voltage pulse is represented by the black curve. The current responses to the second, third, fourth, fifth and sixth voltage pulse are represented by the red, green, blue, light blue and pink curve, respectively. Between each voltage pulse there is no voltage applied for 120 seconds.

First it is noticeable, that the current response to the second voltage pulse starts at a *lower* current as the current response to the first voltage pulse after 100 seconds. This indicates a relaxation of the resistance during the time of 120 seconds between the applied voltage pulses. The characteristic strong *increase* of the current, observed at the start of the *second* current response (not only in the first pulse) indicates a relaxation of presumable charge carriers involved, between the applied voltage pulses. The fact that the same behaviour is observed for all following current responses supports this assumption.

Figure 8.3(b) shows the current responses to the same experiment as described in figure 8.3(a), with subsequently applied constant voltage pulses of $V = +1.5$ V. It is noticed, that the current response to the second voltage pulse starts at a *higher* current as the current response to the first voltage pulse after 100 seconds. This indicates a relaxation of the resistance during the time of 120 seconds between the applied voltage pulses. The characteristic strong *decrease* of the current, observed at the start of the second current response (not only

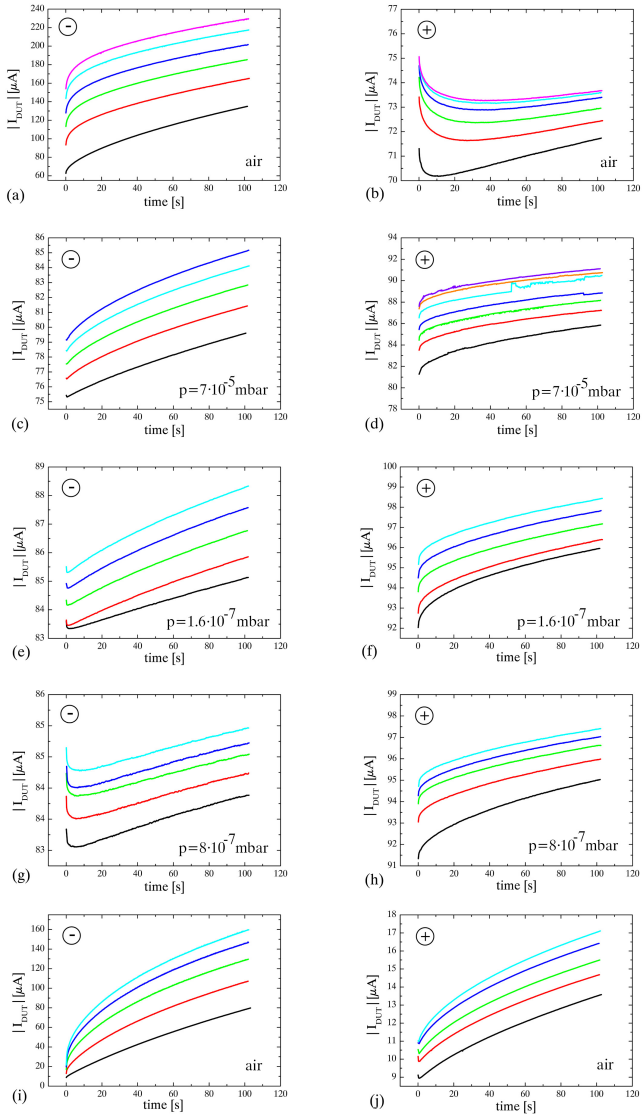

Figure 8.3: $I(t)$-plots of repeated forming pulses with a pulse length of 100 seconds NiO cells in different ambient atmospheres at a constant voltage. The forming characteristics at a negative voltage of $V = -1.5$ V subsequently performed in air, at $p = 7 \cdot 10^{-5}$ mbar, after 30 hours in vacuum conditions ($p = 8 \cdot 10^{-7}$ mbar), after 245 hours in vacuum conditions ($p = 1.6 \cdot 10^{-7}$ mbar) and 1 hour after exposure to air again are shown in (a), (c), (e), (g) and (h), respectively and for a positive voltage stress in (b), (d), (f), (h) and (j), respectively. The measurements are performed on micro devices with 100 μm $\times$ 100 μm electrode size and 25 nm NiO film thickness, at room temperature.

in the first pulse) indicates a relaxation of presumable charge carriers involved, presumably in the opposite direction as in figure 8.3(a). The fact that this behaviour is observed for all following current responses supports this indication.

Figure 8.3(c), (e) and (g) show the same experiment as described in figure 8.3(a), at a pressure $p = 7 \cdot 10^{-5}$ mbar during pumping, after 30 hours in vacuum conditions ($p = 8 \cdot 10^{-7}$ mbar) and after 245 hours in vacuum conditions ($p = 1.6 \cdot 10^{-7}$ mbar). As already discussed, shows the forming at negative constant voltage in vacuum the qualitatively same characteristic as the characteristic at positive constant voltage stress in air. However, when figure 8.3(c), (e) and (g) are compared with each other, it is observed that this characteristic becomes more and more prominent, the longer the devices are exposed to vacuum.

Figure 8.3(d), (f) and (h) show the same experiment as described in figure 8.3(b), at a pressure $p = 7 \cdot 10^{-5}$ mbar during pumping, after 30 hours in vacuum conditions ($p = 8 \cdot 10^{-7}$ mbar) and after 245 hours in vacuum conditions ($p = 1.6 \cdot 10^{-7}$ mbar). As observed before, shows the forming at positive constant voltage in vacuum the qualitatively same characteristic as the characteristic at positive constant voltage stress in air. However, when figure 8.3(d), (f) and (h) are compared with each other, it is observed that this characteristic becomes more and more prominent, the longer the devices are exposed to vacuum. This observation for positive, as well as for negative voltage stress, indicates that the properties of the NiO films are altered by rather slow processes, e.g., physisorption, chemisorption, physical desorption and/or chemical desorption, during the exposure to vacuum conditions.

Finally, figure 8.3(i) and (j) show the same experiment as described in figure 8.3(a) and (b), respectively, one hour after exposure to air again. The same forming characteristics as in figure 8.3(a) and (b) are observed again, as expected.

8.2 The effects of heating in air

If the assumption is correct, that the water in the air is responsible for the asymmetric forming characteristics in the NiO resistive switching devices, then removal of physisorbed water by heating should show a change in resistance of the device. Figure 8.4(c) shows the Arrhenius plot of the resistance of a 50 μm $\times$ 50 μm NiO cell in the pristine state during subsequent heating from 21°C up to 172°C and cooling down in air. The activation energy E_A of the conductivity of the pristine NiO device, measured at a small voltage of $V = 10$ mV, is determined by the relation:

$$R = R_0 \cdot e^{\frac{E_A}{k_B T}} \tag{8.1}$$

During heating from 21°C until about 76°C the Arrhenius plot shows a constant slope, correlating to a constant activation energy $E_A^{heat} = 331$ meV. Also during cooling down from 172°C to 25°C the Arrhenius plot shows a constant activation energy $E_A^{cool} = 394$ meV, which is in good agreement with literature values for NiO [103]. However, during heating from 76°C to about 119°C the resistance of the sample increasingly drops, with a non-constant activation energy. Apparently, in this temperature region, a transition between the previously mentioned conduction mechanisms with constant activation energies takes place. This temperature range could point to the desorption of physisorbed water out of the NiO device, reducing the resistance of the device, as similarly reported for the conductivity of CuO nanowires [97].

Figure 8.4(a) shows the Arrhenius plot of a 50 μm $\times$ 50 μm micro device with 50 nm NiO layer thickness in the OFF state. It shows a similar Arrhenius behaviour as the device in the pristine state (figure 8.4(c)). This can be explained by the dominating resistance of the semiconducting NiO surrounding the filament in the OFF state (see chapter 6.4.1). The transition during heating from 76°C to about 119°C is clearly visible. However, a NiO device in the ON state, as shown in figure 8.4(b), shows a metallic conduction and no clearly visible transition between two different activated conduction states.

Figure 8.4(d) shows the resistance of pristine devices before heating (black squares) and the resistances after the heating and subsequent cooling down experiment shown in figure 8.4(c) (red circles). 24 hours after the experiment shown in (c), the samples are measured once again (green triangles). Clearly visible is the recovery of the resistance of the measured devices, back towards the pristine resistance. 81 hours after the experiment shown in (c) the resistances of the devices are measured once more (blue triangles). A further increase of the resistances of the devices is observed. This means the drop in resistance caused by the heating experiment is (partially) *reversible* by exposure to air at room temperature.

This observation can be interpreted by the physisorption of water on the NiO

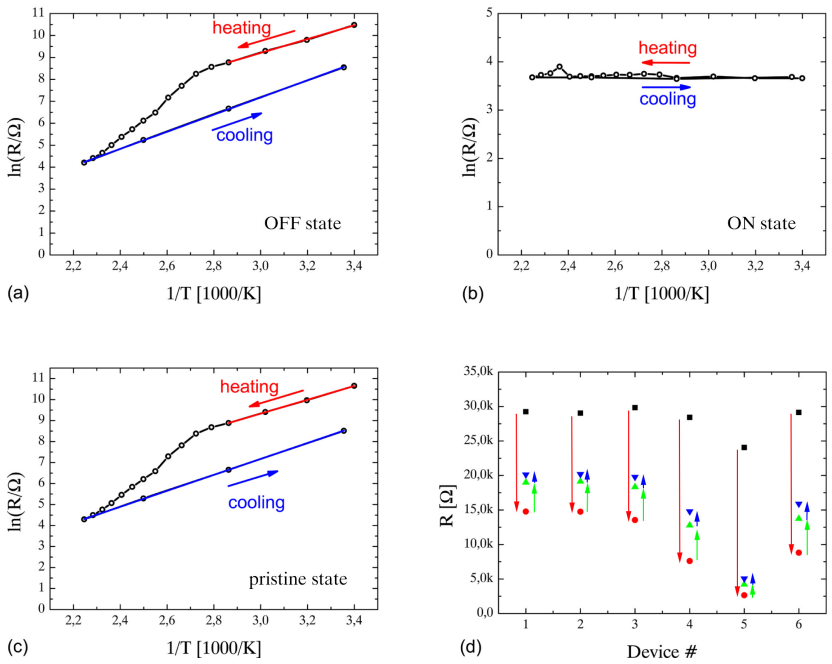

Figure 8.4: Arrhenius plots of the resistance of a 50 μm $\times$ 50 μm NiO cell in the OFF state (a), a cell in the ON state (b) and a cell in the pristine state (c) during subsequent heating and cooling down in air. The thickness of the NiO layer is 50 nm. The time between each resistance measurement is 10 minutes. (d) shows the resistance of pristine devices before heating (black squares), directly after the experiment shown in (c) (red circles), 24 hours after the experiment shown in (c) (green triangles) and 81 hours after the experiment shown in (c) (blue triangles). These measurements are performed at 30°C at 10 mV in air.

surface upon exposure to air at room temperature. Likewise, the decrease of resistivity upon heating indicates a physical desorption of water.

8.3 XPS analysis during heating in vacuum

To get a deeper atomistic insight into the observed (partially reversible) decrease in resistance upon heating the NiO resistive switching devices, XPS analysis are performed during heating a NiO thin film in ultra high vacuum (UHV). The preparation of this film is equal to the preparation of the resistive switching device used in the previous chapter 8.2, but without Pt top electrode.

Figure 8.5 shows the O1s XPS spectrum of the NiO surface at a detector angle of 22° (a) and 45° (b) from the sample surface. At an angle of 22° the detector

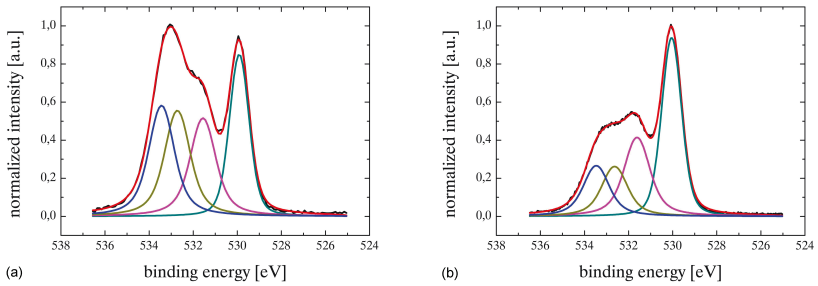

Figure 8.5: O1s XPS spectrum of a 50 nm NiO surface at a detector angle of 22° (a) and 45° (b). The black line represents the measured data. The red line represents the simulated curve, consisting of the addition of the green, pink, yellow and blue curve. These represent the spectrum of NiO, $Ni(OH)_2$ and adsorbates with their peaks at 530 eV, 531.7 eV, 532.6 eV and 533.4 eV, respectively.

will receive relatively more photoelectrons that originate from the NiO surface, while the detector will detect more bulk-originated photoelectrons at an angle of 45°. A comparison of the two spectra yields, that the intensities of the peaks at a binding energy of 530 eV, representing NiO and at 531.7 eV, representing $Ni(OH)_2$ [105, 124, 78, 129, 172] are relatively equal in both spectra. This allows the conclusion, that NiO and $Ni(OH)_2$ are present on the surface *and* in the bulk (at least until the mean free path of the escaping electrons of about 2 nm [16]) of pristine NiO films, after exposure to air.

The intensities of the peaks at binding energies of 532.6 eV and 533.4 eV in the spectrum detected at 22° are higher then the ones detected at 45° and therefore originate from adsorbates at the surface of the NiO film.

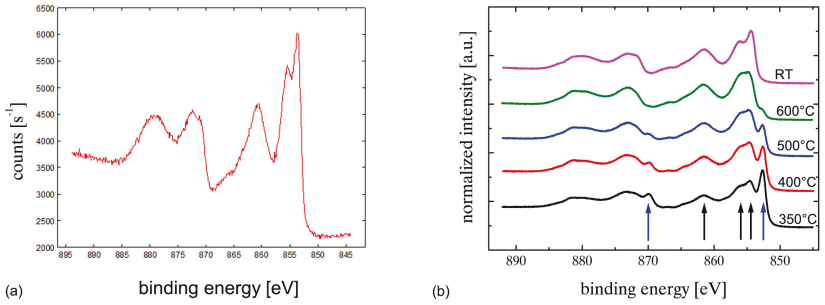

Figure 8.6: Ni2p XPS spectra of an untreated 50 nm NiO layer (a) and of the 50 nm NiO layer during subsequent heating in vacuum (b), measured at a detector angle of 45°. Clearly visible are the characteristic NiO peaks at 854.5 eV, 856.3 eV and 861.7 eV. During heating also the characteristic Ni peaks appear at 870 eV and 852.9 eV.

Figure 8.6(a) shows the Ni2p XPS spectrum, measured at a detector angle of 45°, of a pristine NiO layer with all expected electronic contributions of Ni in NiO (855 eV, 856.8 eV, 861.1 eV, 873 eV, 879.8 eV) [149, 124, 143]. Figure 8.6(b) shows the Ni2p spectra, measured at a detector angle of 45°, of a NiO layer during subsequent heating in UHV (b). The black arrows indicate the characteristic peaks of Ni in NiO at 854.5 eV, 856.3 eV and 861.7 eV. Comparison of the spectrum of the pristine layer (a) with the spectrum during heating (b) reveals, that after heating the sample up to 350°C additional peaks appear at 869.7 eV and 852.3 eV, indicated by the blue arrows. These peaks correspond to *metallic nickel* [175]. This means by heating a pristine NiO layer, that has been in air previously, up to 350°C in UHV metallic nickel appears at the NiO surface!

Comparing the relative intensities of the metallic nickel peaks during heating shows, that a further increase of the temperature reduces the amount of metallic nickel in the NiO layer again.

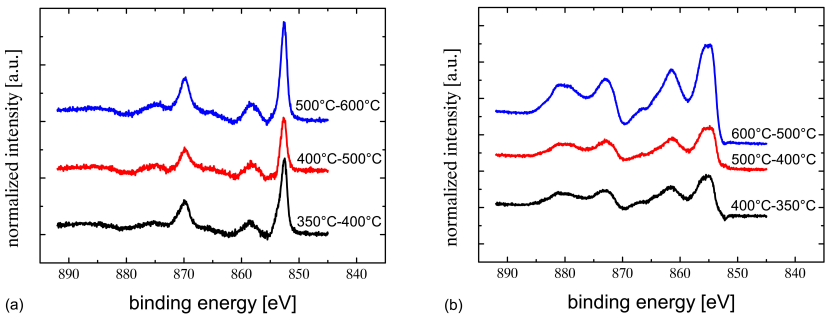

Figure 8.7: The differences of the Ni2p XPS spectra shown in figure 8.6 show the characteristic peaks of Ni, when a spectrum at higher temperature is subtracted from a spectrum at lower temperature (a). When a spectrum at lower temperature is subtracted from a spectrum at higher temperature the characteristic spectrum of NiO appears (b).

To verify this interpretation, the Ni2p XPS spectra at higher temperature are subtracted from the spectra at lower temperature (figure 8.7(a)). If the amount of metallic nickel is reduced again by heating beyond 350°C, the result of these subtractions should show the characteristic peaks of metallic Ni. Indeed, for the temperature steps at which the nickel concentration in the NiO film decreases, the characteristic Ni2p spectrum for metallic nickel appears.

Vice versa, when a spectrum at lower temperature is subtracted from a spectrum at higher temperature the characteristic spectrum of NiO appears (figure 8.7(b)).

The appearance of metallic nickel after heating in UHV should also be visible in the XPS spectrum of the valence band. Therefore, the XPS spectra of the valence band of a pristine NiO layer during subsequent heating in UHV is

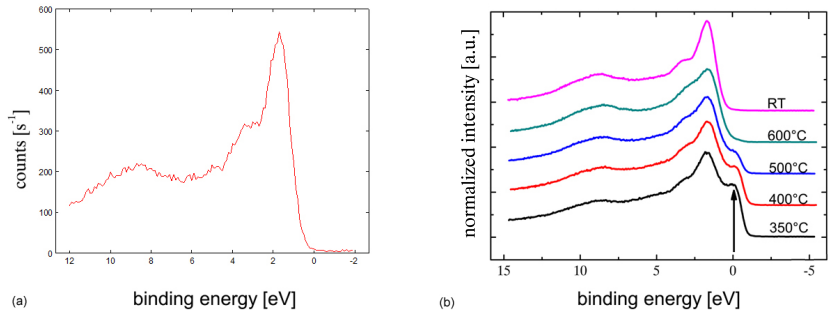

Figure 8.8: XPS spectra of the valence band of an untreated 50 nm NiO layer (a) and of the 50 nm NiO layer during subsequent heating in vacuum (b). Clearly visible are the characteristic metallic Ni peaks that appear at 350°C and disappears again with further heating in vacuum conditions.

shown in figure 8.8(b). Clearly visible is the characteristic metallic Ni peak in the bandgap, indicated by the arrow, that appears at 350°C and disappears again with further heating in vacuum conditions. As a reference, the XPS spectrum of the valence band of the pristine NiO layer before heating is shown in figure 8.8(a). Here, no metallic nickel peak in the bandgap is observed.

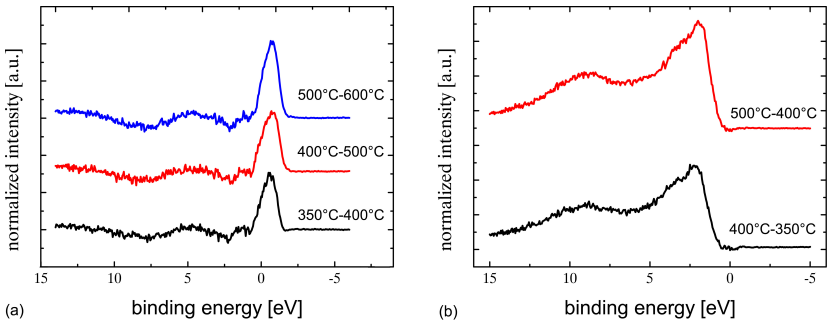

Figure 8.9: The differences of the XPS spectra of the valence band shown in figure 8.8 show the characteristic peak in the bandgap, when a spectrum at higher temperature is subtracted from a spectrum at lower temperature (a). When a spectrum at lower temperature is subtracted from a spectrum at higher temperature the characteristic spectrum of NiO appears (b).

Subtraction of the XPS spectra of the valence band at higher temperature from the spectra at lower temperature are shown in figure 8.9(a). If the amount of metallic nickel is reduced again by heating beyond 350°C, the result of these subtractions should show the characteristic peak in the bandgap, caused by metallic Ni. Indeed, for the temperature steps at which the nickel concentration in the NiO film decreases, the characteristic peak in the bandgap appears.

When a spectrum at lower temperature is subtracted from a spectrum at higher

temperature, the characteristic spectrum of NiO appears (figure 8.9(b)).

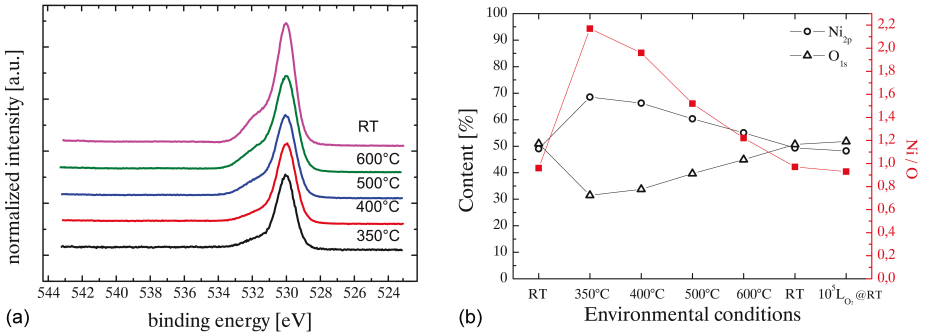

Figure 8.10: (a) The O1s spectra of a NiO layer during subsequent heating in UHV. (b) The Ni and O content (at the left) and the Ni/O ratio (at the right) in the NiO thin film in the different environmental conditions.

The appearance of metallic nickel upon heating up to 350°C should also have effect on the binding energies of oxygen in the NiO film. Therefore, in figure 8.10(a) the O1s XPS spectra of the NiO film during subsequent heating in UHV are shown, measured at a detector angle of 45°. Comparison with figure 8.5(b) shows that heating the NiO layer up to 350°C results in a major decrease of the relative intensity of the peak at $E_{Bind} = 531.7$ eV corresponding to Ni-OH bonds [105, 129, 172]. Apparently, OH is removed by heating up to 350°C, leaving metallic nickel behind. During further subsequent heating up to 600°C only the the O1s spectrum of NiO is observed as shown in figure 8.10(a).

Or in other words, at room temperature, exposure of NiO to air (or a water ambient atmosphere) triggers the formation of a high resistive $Ni(OH)_2$ at the NiO surface [105], which is removed by heating up to 350°C in UHV, leaving metallic nickel behind. This delivers a possible explanation for the major decrease in resistance of the resistive switching devices during heating shown in figure 8.4 and the increase in resistance after exposure to air (or a water ambient atmosphere) at room temperature.

Comparing the relative intensities of the Ni and O contributions in the XPS spectra measured at the different temperatures yields the Ni and O contents in the surface (2 nm) of the NiO film at the different temperatures, shown in figure 8.10(b). At room temperature the Ni/O ratio is almost stoichiometric. During heating up to 350°C in UHV a major increase in the nickel content is observed, as discussed. During further heating the nickel content decreases again until the initial almost stoichiometric composition is reached again, probably by reoxidation with oxygen from the bulk NiO.

8.4 The reduction and oxidation of NiO thin films

To confirm the findings of the previous section 8.3, the conductivity of a 50 nm NiO film on an oxidized Si substrate (400 nm SiO_2) is measured at temperatures up to 400°C in an oxygen ambient atmosphere and in vacuum conditions. To achieve this, the setup shown in figure 3.9 described in chapter 3.8.3 is used.

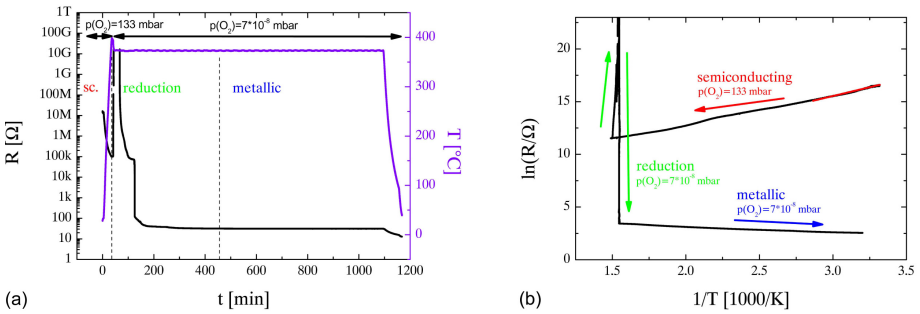

Figure 8.11: (a) Reduction of a 50 nm NiO film on an oxidized Si substrate (400 nm SiO_2) by a decrease of the oxygen partial pressure $p(O_2)$. The temperature T is shown by the right axis. (b) The Arrhenius plot of the semiconducting phase, the metallic phase and the transition between them. The resistance is measured at a constant voltage of $V = 10$ mV [168].

Figure 8.11(a) shows the resistance R (black curve), measured at $V = 10$ mV, and temperature T (purple curve) of the sample as a function of time t. Before the measurement starts, the glass vacuum tube is evacuated to a base pressure of $p = 3 \cdot 10^{-10}$ mbar. Then, oxygen (purity $\geq 99.999\%$) is let into the vacuum tube until a pressure of $p(O_2) = 133$ mbar is reached and all valves to the vacuum tube are closed. At $t = 0$ the resistance R of the sample is about $R = 20$ MΩ. During the subsequent heating up to $T = 400$°C the resistance decreases, because of the semiconducting properties of the NiO film. This is confirmed by the Arrhenius plot of the measurement shown in figure 8.11(b). An activation energy $E_A = 578$ meV is found [168].

When a temperature of $T = 400$°C is reached, the vacuum tube is pumped down to a pressure $p = 7 \cdot 10^{-8}$ mbar. First, a strong increase of the resistance R up to at least $R = 10$ GΩ is observed (measurement limit of the experimental setup), followed by a decrease to about $R = 50\ \Omega$. This can be interpreted by the reduction of the NiO film (at least at the contacted surface of the sample) which increases the Ni content in the film, resulting in a decrease of the resistance of the film [168].

NiO is known to be a p-type semiconductor with a higher oxygen than nickel content (see chapter 2.2.4). Therefore, during reduction of NiO first stoichiometric NiO is formed, before the Ni content exceeds the oxygen content. This results in the strong increase of the resistance observed at the beginning of the reduction

process [168].

When the resistance of the NiO film does not show any significant decrease any more at a pressure $p = 7 \cdot 10^{-8}$ mbar and temperature $T = 400°C$, the temperature is slowly decreased to room temperature. The decrease in resistance during cooling confirms the metallic conduction after the reduction process (see figure 8.11(b)). The presumable appearance of metallic nickel in vacuum ($p = 7 \cdot 10^{-8}$ mbar) at a temperature $T = 400°C$ supports the findings in the previous section 8.2.

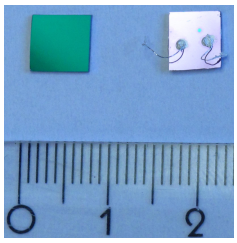

Figure 8.12: Picture of the untreated 50 nm NiO thin film on the left and the film after reduction by heating in vacuum on the right.

Figure 8.12 shows a picture of the untreated 50 nm NiO thin film on the left and the film after reduction by the previously described experiment on the right. The green colour of the untreated sample is typical for NiO thin films of 50 nm thickness and originates from the NiO film thickness. The metallic impression of the reduced sample on the right supports the interpretation of the appearance of metallic nickel during the previously described experiment.

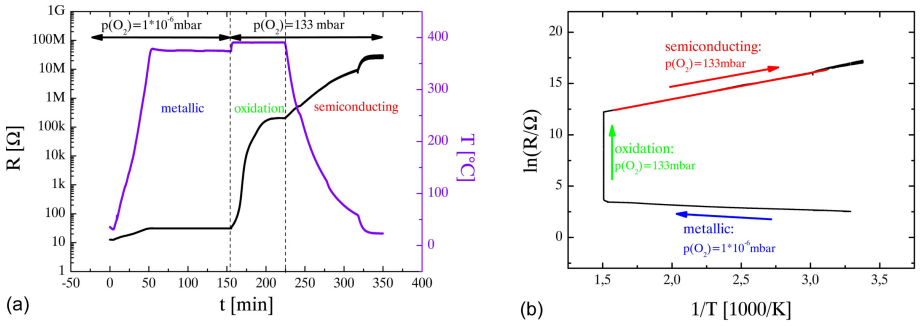

Figure 8.13: (a) The oxidation of the reduced 50 nm NiO film on an oxidized Si substrate (400 nm SiO_2) by an increase of the oxygen partial pressure $p(O_2)$ at $T = 400°C$. The temperature T is shown by the right axis. (b) The Arrhenius plot of the semiconducting phase, the metallic phase and the transition between the two phases. The resistance is measured at a constant voltage of $V = 10$ mV [168].

Figure 8.13(a) shows the resistance R (black curve), measured at $V = 10$ mV,

and temperature T (purple curve) of the NiO sample that is reduced in the previously described experiment, as a function of time t. Before the measurement starts, the glass vacuum tube is evacuated to a base pressure of $p = 4 \cdot 10^{-10}$ mbar. Then, oxygen (purity $\geq 99.999\%$) is let into the vacuum tube until a pressure of $p(O_2) = 1 \cdot 10^{-6}$ mbar is reached and all valves to the vacuum tube are closed. At $t = 0$ the resistance R of the sample is about $R = 15\ \Omega$. During the subsequent heating up to 400°C the resistance increases, because of the metallic properties of the reduced film. This is confirmed by the Arrhenius plot of the measurement shown in figure 8.13(b) [168].

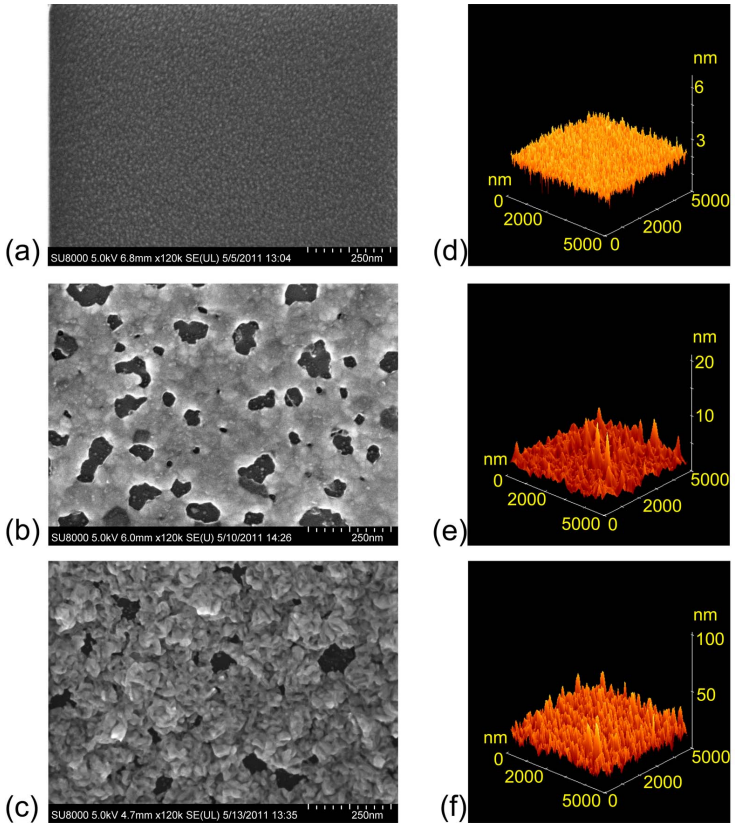

Figure 8.14: (a) SEM images of the pristine NiO sample, (b) the sample after reduction and (c) the sample after reoxidation. (d), (e) and (f) show three-dimensional AFM images of the pristine NiO sample, the sample after reduction and the sample after reoxidation, respectively.

When a temperature of 400°C is reached, oxygen (purity $\geq 99.999\%$) is let into the vacuum tube until a pressure of $p(O_2) = 133$ mbar is reached. A strong increase of the resistance R up to $R = 200\ \text{k}\Omega$ is observed. This can be interpreted by the oxidation of the reduced film, which increases the oxygen

content in the film, resulting in a increase of the resistance of the film [168].

When the resistance of the NiO film does not show any significant increase any more at a pressure $p = 133$ mbar and temperature $T = 400°C$, the temperature is slowly decreased to room temperature. The increase of the resistance during cooling confirms the semiconducting properties of the film after the reoxidation process (see figure 8.13(b)). An activation energy $E_A = 442$ meV is found, which is in good agreement with literature values for NiO [103].

Figure 8.14 shows SEM images and three-dimensional AFM images of the pristine sample, the sample after reduction and the sample after reoxidation. The SEM image of the reduced sample (figure 8.14(b)) shows a completely changed morphology of the film, compared to the SEM image of the pristine sample (figure 8.14(b)). Also the comparison of the AFM image of the reduced sample (figure 8.14(e)) with the AFM image of the pristine sample (figure 8.14(d)) indicates a strong increase of the roughness of the sample after the reduction of the film, supporting this finding. The reoxidation of the film further increases the roughness of the sample as shown in figure 8.14(f). This can be explained by the growth of the oxide on the reduced surface. The SEM image of the reoxidized film (figure 8.14(c)) supports this.

In summary, these images indicate a complete reduction and subsequent reoxidation of the sample during the previously described experiments at a temperature $T = 400°C$ and a oxygen partial pressure of $p(O_2) = 7 \cdot 10^{-8}$ mbar and $p(O_2) = 133$ mbar, respectively. However, according to the Ellingham Diagram (see figure 2.7 in chapter 2.1.2) bulk single crystalline NiO is expected to form/dissociate at an oxygen partial pressure $p(O_2) = 2.6 \cdot 10^{-25}$ mbar at a temperature $T = 400°C$. The findings in this section indicate, that the NiO thin films sputtered for the resistive switching devices investigated in this work must be very porous (as already found in chapter 5.1.1) and are therefore very assailable for ambient gas atmospheres.

8.5 Conclusions

The measurements discussed in chapter 8.1 point out, that the polarity dependence of the forming behaviour in *air* is qualitatively *not* equal to the forming behaviour in *oxygen* atmosphere, as predicted by the model in chapter 7.4. Instead, the polarity dependence of the forming in air is qualitatively equal to the forming behaviour in a *water* ambient atmosphere (see figure 8.1 and 8.2). The polarity dependence of the forming in *oxygen* ambient atmosphere is qualitatively equal to the forming behaviour in *vacuum* conditions. The measurements discussed in chapter 8.2 support these observations. Therefore the model proposed in chapter 7.4 has to be revised.

The formation of $Ni(OH)_2$ via the decomposition of water on NiO surfaces:

$$NiO + H_2O \rightleftharpoons Ni(OH)_2 \tag{8.2}$$

has been shown by a wide range of techniques, e.g., XPS analysis [79, 104], vibrational studies [85], SIMS characterization [23], ion scattering experiments [12], X-ray diffraction [181] and electron-energy loss spectroscopy [30].

The presence of $Ni(OH)_2$ on the surface of pristine samples studied in this work (after exposure to air) is confirmed by the findings in chapter 8.3. However, in chapter 8.3 it is found, that $Ni(OH)_2$ is not only present on the surface, but also in the bulk of the samples (at least within the measurement depth range). Taking the porosity of the investigated NiO films found in chapter 5.1.1 and chapter 8.4 into account, it is plausible to suppose that not only the NiO surface, but also the internal surfaces along grain boundaries in the NiO films exhibit formation of $Ni(OH)_2$, if the exposure time to a water ambient atmosphere (or air) is sufficient to form the $Ni(OH)_2$ [181].

Upon the application of a voltage stress $Ni(OH)_2$, well known for its electrochromic properties, will reversibly react by the following electrochromic reaction [2, 54, 3]:

$$Ni(OH)_2 \rightleftharpoons NiOOH + H^+ + e^- \tag{8.3}$$

The application of a negative electrical potential at the top electrode results in an electrical field that will cause a drift of protons (H^+ ions) towards the top electrode. According to the electrochromic reaction 8.3 this will cause the formation of excess low conductive $Ni(OH)_2$ (resistivity $\rho_{Ni(OH)_2} = 3 \cdot 10^4\ \Omega$ cm [181]) at the top electrode and an excess of highly conductive NiOOH (resistivity $\rho_{NiOOH} = 30\ \Omega$ cm [181]) at the bottom electrode. However, the excess $Ni(OH)_2$ at the top electrode is (partially) compensated by the desorption of water, as described by the chemical reaction 8.2 above (see figure 8.15(a)). Therefore, the resistance of the device decreases and the current will start to increase directly after the application of the negative voltage stress, as observed (see chapter 8.1

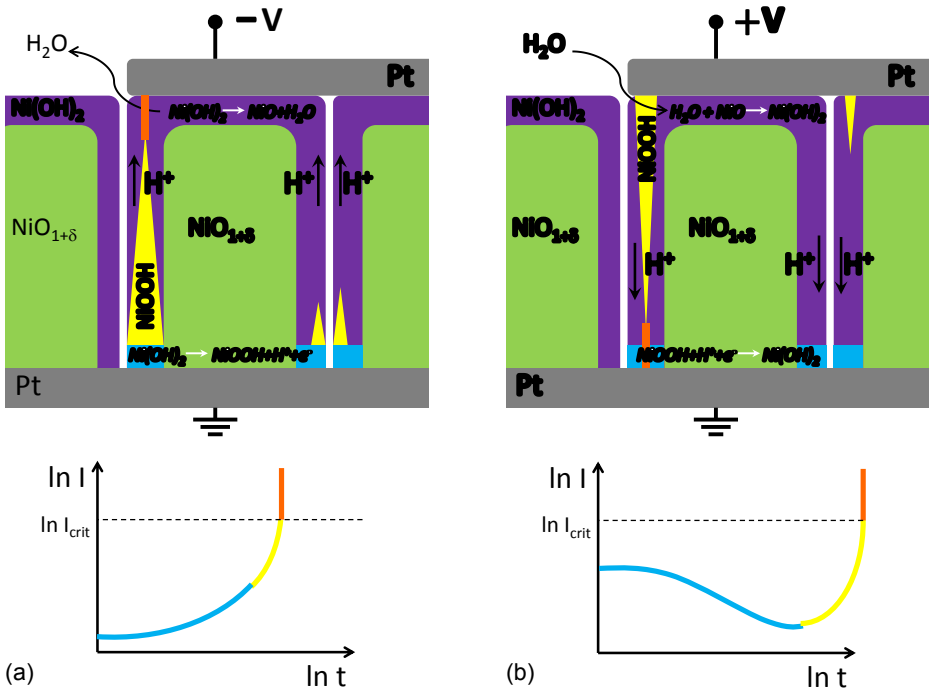

Figure 8.15: Schematic representation of the reactions and drifts of the particles involved in the forming process under negative voltage stress (a) and positive voltage stress (b) in air or water ambient atmosphere. Below the affiliated forming characteristics are sketched. The colours in the forming characteristics represent the different stages of the forming processes and correspond to the formation of the layers in the device sketched in the same colour.

and chapter 7). This is indicated by the blue part of the sketched characteristic I(t) curve for a constant negative voltage stress in air or water ambient environment in figure 8.15(a).

The enrichment of highly conductive NiOOH in the grain boundaries at the bottom electrode, naturally exhibits spots where the concentration of NiOOH is larger than at other spots. Regions with high concentration of NiOOH that are closer to the top electrode will experience a field enhancement, resulting in a faster growth in this spot. In this way a conductive NiOOH-rich filament will grow from the bottom electrode towards the top electrode inside the grain boundary (yellow colour in figure 8.15(a)).

The growth of the filament will continue, until the field between the tip of the filament and the top electrode reaches the dielectric breakdown field strength of $Ni(OH)_2$. Then dielectric (soft) breakdown (by, e.g., bond breakage [106], thermal breakdown due to an increasing conductance by Joule heating [38])

will occur, resulting in a sudden increase of the current (orange colour in figure 8.15(a)). To prevent hard dielectric breakdown, a current compliance has to be set.

An application of the opposite polarity will cause a drift of protons (H^+ ions) towards the bottom electrode. This causes the formation of excess low conductive $Ni(OH)_2$ at the bottom electrode and an excess of highly conductive NiOOH at the top electrode. However, the excess NiOOH (or depletion of $Ni(OH)_2$) at the top electrode is (partially) compensated by the absorption of water, as described by the chemical reaction 8.2 above (see figure 8.15(b)). Therefore, the resistance of the device increases and the current will start to decrease directly after the application of the positive voltage stress, as observed (see chapter 8.1 and chapter 7). This is indicated by the blue part of the sketched characteristic I(t) curve for a constant positive voltage stress in air or water ambient environment in figure 8.15(b).

Although the enrichment of highly conductive NiOOH in the grain boundaries at the top electrode is partially compensated, still an enrichment of NiOOH will occur. The enrichment of NiOOH exhibits a statistical spread, causing spots where the concentration of NiOOH is larger than at other spots. Regions with high concentration of NiOOH that are closer to the bottom electrode will experience a field enhancement, resulting in a faster growth in this spot. In this way a conductive NiOOH-rich filament will grow from the top electrode towards the bottom electrode inside the grain boundary (yellow colour in figure 8.15(b)).

The growth of the filament will continue, until the field between the tip of the filament and the bottom electrode reaches the dielectric breakdown field strength of the $Ni(OH)_2$/NiOOH. Then dielectric (soft) breakdown will occur, resulting in a sudden increase of the current (orange colour in figure 8.15(b)). To prevent hard dielectric breakdown, a current compliance has to be set.

The enhanced mobility in grain boundaries makes it plausible to suppose that NiOOH filaments in grain boundaries grow faster than filaments inside NiO grains (by the migration of other charge carriers, see below). Additionally, the contribution of the NiO grains for the conductivity is negligible, because of the high resistivity $\rho_{crys.NiO} = 10^{13}$ Ω cm [181] of crystalline NiO compared to the resistivity $\rho_{Ni(OH)_2} = 3 \cdot 10^4$ Ω cm [181] of $Ni(OH)_2$ and the resistivity $\rho_{NiOOH} = 30$ Ω cm [181] of NiOOH. The measured resistivity $\rho_{pris.NiO} =$ 300 kΩ cm of pristine NiO samples (after exposure to air) in chapter 5.4, which is well below the resistivity of crystalline NiO and above the resistivity of $Ni(OH)_2$ and NiOOH is therefore another indication for the presence of $Ni(OH)_2$/NiOOH in the grain boundaries.

The decrease in resistance at the bottom electrode during the application of negative voltage stress and the increase of the resistance during positive polarity can explain the shorter *forming times* at negative- and the longer forming times at positive voltage stress, discussed in chapter 7; a high resistive layer at the bottom interface causes a large voltage drop over this interface layer, which results in a lower effective voltage over the rest of the $Ni(OH)_2$/NiOOH layer,

resulting in a longer forming time. Vice versa, a low resistive NiOOH layer at the bottom electrode shortens the distance between the low resistive NiOOH and the top electrode, which yields a higher electrical field over the rest of the $Ni(OH)_2$/NiOOH layer, resulting in a shorter forming time.

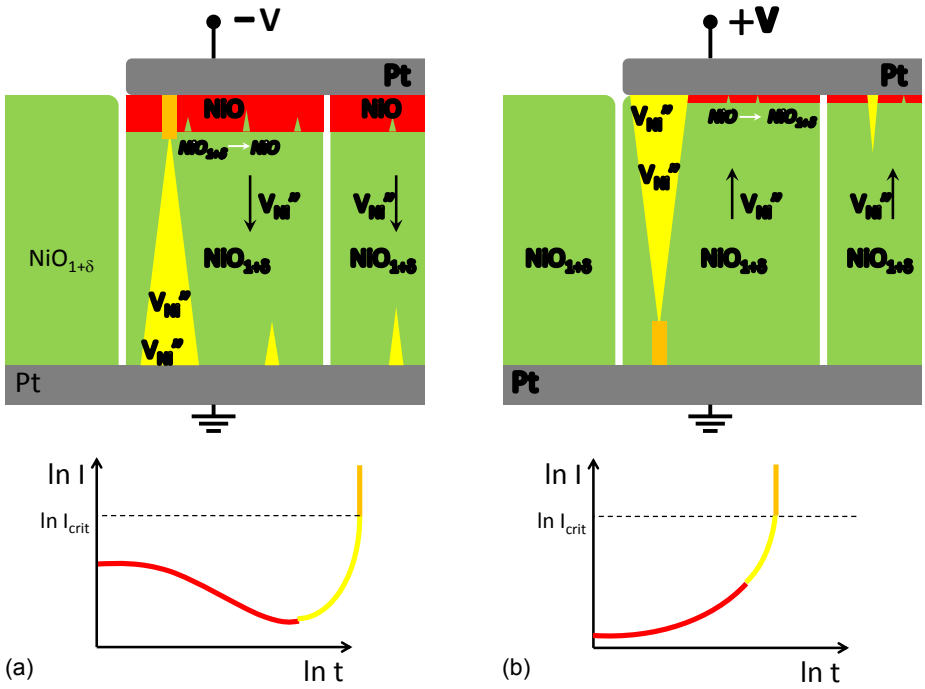

Figure 8.16: Schematic representation of the reactions and drifts of the particles involved in the forming process under negative voltage stress (a) and positive voltage stress (b) in vacuum or oxygen ambient atmosphere. Below the affiliated forming characteristics are sketched. The colours in the forming characteristics represent the different stages of the forming processes and correspond to the formation of the layers in the device sketched in the same colour.

To explain the reversal of the forming characteristics in vacuum conditions and oxygen ambient atmosphere, compared to air and water ambient atmosphere, it is supposed that water desorbs from the NiO surface and grain boundaries (inner surfaces) because of the low partial water pressure in vacuum and oxygen conditions. Therefore, the NiO film consists of NiO grains without $Ni(OH)_2$ layer (according to reaction 8.2) and with (nearly) stoichiometric NiO at the top electrodes, caused by the sputter deposition of the Pt top electrodes (see chapter 5.4 and chapter 6.2).

Upon the application of negative voltage on the top electrode, a drift of nickel vacancies ($V_{Ni}^{''}$) towards the bottom electrode causes a depletion of nickel va-

cancies at the top electrode, resulting in a growth of the stoichiometric NiO layer at the top electrode. The experiments shown in chapter 8.1 show, that the forming behaviour in oxygen and vacuum conditions are qualitatively equal. This means that there is *no oxygen exchange* with the ambient environment, as described in chapter 7.4. Therefore, the depletion of nickel vacancies at the top electrode is apparently not compensated by (oxygen) exchange with the ambient atmosphere and the resistance of the cell increases, causing a decrease of the current directly after the application of the negative voltage stress (red colour in figure 8.16(a)).

The enrichment of nickel vacancies at the bottom electrode exhibits a statistical spread, causing spots where the concentration of nickel vacancies is larger than at other spots. Regions with high concentration of nickel vacancies that are closer to the top electrode will experience a field enhancement, resulting in a faster growth in this spot. In this way a filament consisting of nickel vacancies grows from the bottom towards the top electrode (yellow colour in figure 8.16(a)).

The growth of the filament will continue, until the field between the tip of the filament and the top electrode reaches the dielectric breakdown field strength of NiO. Then dielectric (soft) breakdown will occur, resulting in a sudden increase of the current (orange colour in figure 8.16(a)). To prevent hard dielectric breakdown, a current compliance has to be set.

In case of application of positive voltage on the top electrode, the drift of the nickel vacancies in the opposite direction will lead to an enrichment of nickel vacancies at the top electrode, resulting in a thinning of the stoichiometric NiO layer at the top electrode. Therefore, instantly after application of the positive voltage stress, a decrease in resistance is observed (red colour in figure 8.16(b)).

The enrichment of nickel vacancies at the top electrode exhibits a statistical spread, causing spots where the concentration of nickel vacancies is larger than at other spots. Regions with high concentration of nickel vacancies that are closer to the bottom electrode will experience a field enhancement, resulting in a faster growth in this spot. In this way a filament consisting of nickel vacancies will grow from the top towards the bottom electrode (yellow colour in figure 8.16(b)).

The growth of the filament will continue, until the field between the tip of the filament and the bottom electrode reaches the dielectric breakdown field strength of NiO. Then dielectric (soft) breakdown will occur, resulting in a sudden increase of the current (orange colour in figure 8.16(b)). To prevent hard dielectric breakdown, a current compliance has to be set.

In chapter 8.1 it is found, that a sample, previously exposed to air, shows more and more prominently the forming behaviour typically observed in vacuum conditions, the longer the sample is exposed to the vacuum conditions. This observation can be explained by the model proposed above: The less $Ni(OH)_2$ is present in grain boundaries, the more prominent the forming behaviour inside

the NiO grains becomes.

Additionally, this model gives an explanation for the morphological changes observed after the forming in air, discussed in chapter 7.4 figure 7.13. All observed morphological changes are located at the *edges* of the top electrodes, where the interaction of the NiO layer with the ambient atmosphere is most likely. Because mainly grain boundaries at the edges of the electrodes have access to the air or water ambient atmosphere, mainly in these grain boundaries $Ni(OH)_2$ will form. This supports the proposed model, which describes the forming of resistive switching devices by the interplay of $Ni(OH)_2$ in the grain boundaries of the NiO film and the applied voltage stress. On the other hand, field enhancement at the edges of the electrodes is also higher than under the electrodes, which can also be a reason for the location of the morphological changes at the edges of the top electrodes.

Finally, this model gives a possible location for the subsequent resistive switching. It is plausible, that after completion of the forming step, the resistive switching takes place in the heavily damaged regions near the electrodes. Within these regions a lot of dangling bonds exist and the binding energies between the chemical compounds are presumably lowest.

9 Conclusions

9.1 Summary

Within this work, the resistive switching properties of NiO thin films have been investigated. To investigate the potential integration into CMOS and the related required performance of NiO-based memory devices, devices with several nanometer sized tungsten plugs were used as bottom electrodes. To elucidate and avoid effects like oxidation of the tungsten plugs as a result of the subsequent NiO deposition, also so called nano crossbar structures with platinum bottom and top electrodes were fabricated. These were made of 100 nm wide bottom platinum lines and 100 nm wide top platinum lines, that overlay each other in a resulting active cell area of 100 nm by 100 nm. To investigate the scaling properties, devices with planar platinum bottom electrode and square platinum top electrodes were fabricated. The thickness of the active NiO layer is thereby varied from 25 nm to 300 nm while the top electrode sizes reach from 50 μm by 50μm to 600 μm by 600 μm.

The NiO thin films were deposited by direct current (DC) sputtering technique from a metallic Ni target as well as by radio frequency (RF) sputtering technique using a stoichiometric NiO target and were afterwards characterized by RBS, XRD, SEM, XPS and TEM. Because of the higher reproducibility of the film properties most films used in this thesis were sputtered by the RF sputtering technique. On the other hand, the DC sputtering technique enables the growth of NiO films with different Ni/O ratio's. The study of these films revealed a maximum in $R_{pristine}$ and R_{sheet} at the point of stoichiometry, as predicted by the theory of point defect chemistry. However, no influence of the different Ni/O ratio's on the resistive switching properties of the films in question could be shown, probably because of the inherent stochasticity of the resistive switching effect.

From the thickness dependence of $R_{pristine}$, R_{sheet} and by AFM analysis, a model for the growth of the NiO films could be derived, involving a transition from granular into columnar grain growth. Analysis of the current-voltage

characteristics of pristine devices revealed, that the Poole-Frenkel effect is the dominating conduction mechanism at higher field strength. A trap energy of ϕ_{PF} of about 600 meV and a charge carrier density of about $2 \cdot 10^{19}\ m^{-3}$ to $10 \cdot 10^{19}\ m^{-3}$ was determined. Impedance measurements of pristine devices confirmed the bulk limited conduction.

Impedance studies indicated that correlated barrier hopping is the dominating conduction mechanism at low voltages. Impedance measurements of the HRS revealed that the NiO layer in a device in the HRS, in respect to the pristine state, is not changed over the whole electrode area, but is rather locally changed by forming and subsequent resistive switching. The LRS could be modeled by a parallel resistance that shortcuts the bulk impedance. This, in addition to the identical capacitance of devices in the pristine state and HRS indicates that the switching behaviour in NiO thin films originates from local, filamentary changes in conductivity, embedded in an almost unchanged NiO matrix.

From the memory devices integration point of view *forming free* samples could be produced. The unnecessity of a forming process is big step towards a market launch of ReRAM. A statistical analysis of the first 60 switching cycles of these devices yielded several findings. First of all, an estimation of the filament radius could be made yielding a radius r_{CF} of about 2 nm to 4 nm. Moreover it was found, that for all resistances of the previous LRS a constant RESET voltage $V_{RESET} = 0.4$ V was necessary to switch the devices back to the HRS. Using the model of *Ielmini et.al.* [147, 63] of a thermally activated dissolution of a nickel filament for the RESET process, a maximum temperature of $T_{RESET} = 1126$ K was estimated. This rules melting of a nickel filament out as a possible mechanism for the RESET process and supports the nickel dissolution model. Further, it was found that for every observed RESET process a maximum current density j_{CF}^{RESET} of about $2 \cdot 10^{14}$ A/m^2 within the conductive filament was needed to carry out the RESET process, for all resistances of the previous LRS. On the other hand, for the SET process no dependence on the resistance of the preceding HRS was found.

The scaling properties of $R_{Pristine}$, R_{HRS}, R_{LRS}, V_{SET}, V_{RESET}, I_{SET} and I_{RESET} on the electrode area of the resistive switching devices all support the picture of the creation and dissolution of a localized well conducting filamentary path in a insulating NiO matrix. However, simple estimations of the size of the conducting filamentary path, based on the measured resistances of the LRS and HRS, contradict the model of *Ielmini et.al.* [147, 63] insofar, that most probably the conductive filament is not completely dissolved in the HRS. This is supported by *Jung et al.* [72], who showed that the HRS still shows metallic conduction at low temperatures. Resistive switching in NiO resistive switching devices can therefore be seen as the increase and decrease of the cross-sectional area of the conductive filamentary path(s).

From the memory devices performance point of view SET pulses as short as 300 ns at 2.5 V were sufficient to achieve reliable SET operation and RESET pulses as short as 150 ns at 1.2 V were sufficient to achieve reliable RESET

operation [90]. Endurance tests showed an endurance of at least 1000 switching cycles maintaining a R_{HRS} / $R_{LRS} \geq 40$. Repeated pulsed reading of LRS and HRS resistance was stable for more than 30 minutes for both states. Accelerated retention tests at 25 °C, 70 °C and 110 °C showed a R_{HRS} / $R_{LRS} \geq 100$ for at least 10^4 s [90].

To retrieve a better insight in the underlying mechanisms behind the resistive switching effects, the first resistance change, so called forming, which turns the capacitor structures into resistive switching devices was investigated by potentiostatic breakdown studies within the framework of Weibull statistics.

The dielectric breakdown in air was found to be intrinsic for devices with small electrode sizes (100 nm × 100 nm) and extrinsic for devices with bigger electrodes (50 μm × 50 μm). This was explained by the much higher probability of fabrication-induced defects under the bigger electrodes. At elevated temperatures the Weibull statistics of the dielectric breakdown in the devices with bigger electrodes showed both intrinsic and extrinsic breakdown.

Additionally, the statistical investigations on the stochastic nature of the forming process of the memory devices in air revealed an unexpected asymmetry in the forming characteristic and forming time, depending on the applied voltage polarity. This asymmetry was supported by SEM images of the memory devices after forming, showing volcano-like structures for positive and larger elongated structures for all negative voltages at the edges of the electrodes.

From potentiostatic measurements on pristine devices in different ambient atmospheres (e.g. air, water, oxygen, vacuum), as well as from resistivity measurements at elevated temperatures and the subsequent recovery of the resistivity at room temperature in air of devices in LRS, HRS and pristine state, it was concluded, that physisorbed water from the ambient atmosphere is related to the observed asymmetry of forming. XPS analysis during heating of a NiO film in vacuum, showing a decreasing intensity at Ni-OH binding energies and an increasing intensity for metallic Ni for increasing temperatures up to 350 °C supported this conclusion. In another experiment a NiO film of 50 nm thickness was reduced to metallic conductivity at a temperature of 400°C and a oxygen partial pressure of $7 \cdot 10^{-8}$ mbar and subsequently reoxidized at a temperature of 400°C and a oxygen partial pressure of 133 mbar. However, according to the Ellingham Richardson diagram bulk single crystalline NiO is expected to form/dissociate at an oxygen partial pressure of $p(O_2) = 2.6 \cdot 10^{-25}$ mbar and a temperature $T = 400$°C, indicating the porosity and therefore the accessability of the NiO films for ambient gas atmospheres.

The combination of these results led to a proposed model for the forming process in air or water ambient atmosphere, involving the incorporation of water into the grain boundaries in the NiO layer, resulting in the formation of $Ni(OH)_2$ in the grain boundaries. Proton diffusion, induced by the applied voltage, gives rise to the formation of excess NiOOH at the proton depleted electrode and of excess $Ni(OH)_2$ at the proton enriched electrode. However, at the top electrode the excess NiOOH or $Ni(OH)_2$ is compensated by water, originating from the

ambient atmosphere. Therefore, upon the application of negative or positive voltage on the top electrode excess high conductive NiOOH or low conductive $Ni(OH)_2$ is formed in the grain boundaries at the bottom electrode, respectively, resulting in the asymmetric forming behaviour observed equally in air and in water ambient atmosphere. Subsequently a proton-diffusion-driven growth of a conducting NiOOH filament from bottom to top electrode, or vice versa, occurs for negative or positive voltage applied at the top electrode, respectively.

In vacuum conditions or oxygen ambient atmosphere, no $Ni(OH)_2$ is supposed to form in the grain boundaries, because of the lack of water in the ambient atmosphere. In this case, the applied voltage results in a drift of nickel vacancies within the NiO grains, causing a depletion or enrichment of nickel vacancies at the electrodes, depending on the applied voltage polarity. In the case of negative polarity, the depletion of nickel vacancies at the top electrode causes a growth of the stoichiometric NiO layer formed by the deposition of the platinum top electrodes. Positive applied voltage causes a enrichment of nickel vacancies at the stoichiometric NiO layer at the top electrode, resulting in a thinning of the stoichiometric NiO layer. This causes the asymmetric polarity dependent forming behaviour observed in vacuum conditions and oxygen ambient atmosphere, opposite of the polarity dependent forming behaviour observed in air and water ambient atmosphere.

The final phase of the forming process takes place at the interface which is approached by the growing filament. When the field strength between the tip of the filament and the opposite electrode exceeds the breakdown field strength of the material in between, the final (soft) dielectric breakdown takes place.

9.2 Outlook

Despite of the above mentioned achievements and the proposed model for the forming processes in NiO memory devices, it is still a long way to go for a sufficient understanding of the resistive switching phenomena to launch NiO memory devices into reliable industrial applications. First of all, to test the proposed model for the forming processes in NiO memory devices, the forming of annealed samples in vacuum conditions should be investigated. In that case, the water in the grain boundaries of the NiO should be desorbed and the stoichiometric NiO layer at the top electrode should be compensated by nickel vacancies originating form the bulk NiO. If these devices are formed, without breaking the vacuum conditions after the annealing process, the forming characteristics and forming times should become voltage polarity independent.

The emphasis in this work was placed on the investigation of the forming process to gain a better understanding in the formation and nature of the conducting filament(s) in NiO resistive switching devices. To expand the already gained achievements, the forming experiments should be extended to switching experiments in different ambient atmospheres to elucidate the nature of the conductive

filament after forming and/or the nature of the part of the filament where resistive switching takes place.

For future industrial applications, it would be important to investigate the potentiostatic measurements also on the LRS and HRS at different voltages and temperatures to gain information about the kinetics of the resistive switching processes in NiO memory devices. If additionally performed in different ambient atmospheres, more additional information about the resistive switching reactants could be gained.

Publications

Kügeler C., Weng R., Schroeder H., Symanczyk R., Majewski P., Ufert K.-D., Waser R., Kund M.
"Study on the dynamic resistance switching properties of NiO thin films"
Thin Solid Films 518, 22582260 (2010)

Bruchhaus R., Münstermann R., Menke T., Hermes C., Lentz F., Weng R., Dittmann R., Waser R.
"Bipolar resistive switching in oxides: Mechanisms and scaling"
Current Applied Physics 11, e75-e78 (2011)

Kügeler C., Rosezin R., Weng R., Menzel S., Klopstra B., Böttger U., Waser R.
"Fast resistive switching in WO_3 thin films for nonvolatile memory applications"
9th Nanotechnology Conference: IEEE NANO (2009)

Soni R., Meuffels P., Staikov G., Weng R., Kügeler C., Petraru A., Hambe M., Waser R., Kohlstedt H.
"On the stochastic nature of resistive switching in Cu doped $Ge_{0.3}Se_{0.7}$ based memory devices"
Journal of Applied Physics 110, 054509 (2011)

Weng R., Kügeler C., Schroeder H., Bruchhaus R., Waser R.
"Resistive Switching in Nickel Oxide Thin Films as a Promising Candidate for Future High Density Memory Devices" (Poster)
JARA-FIT nanoelectronics days 2010, Aachen, Germany

Szot K., Bruchhaus R., Weng R.
"Optisches Speichermaterial und Verfahren zur Speicherung" (Patent)
European Patent Office, EP 2 521 123 A1, 07.11.2012 Patentblatt 2012/45

Bibliography

[1] European Commission - European Chemicals Bureau, CAS No. 1313-99-1. *IUCLID Dataset* (2000), 1–39.

[2] Ahn, K., Nah, Y., and Sung, Y. The role of defects on the electrochromic response time of sputter-deposited Ni oxide films. *Solid State Ionics 156* (2003), 433–437.

[3] Ahn, K. S., Nah, Y. C., Yum, J. H., and Sung, Y. E. The effect of ar/o2 ratio on electrochromic response time of ni oxides grown using an rf sputtering system. *Jpn. J. Appl. Phys. 41* (2002), L212–L215.

[4] Ahn, S.-E., Lee, M.-J., Park, Y., Kang, B. S., Lee, C. B., and Kim, K. H. Write Current Reduction in Transition Metal Oxide Based Resistance-Change Memory. *Adv. Mater. 20* (2008), 924–928.

[5] Aiken, J. G., and Jordan, A. G. Electrical transport properties of single crystal nickel oxide. *J. Phys. Chem. Solids 29* (1968), 2153–2167.

[6] Altland, A., and Simons, B. *Condensed Matter Field Theory*. Cambridge University Press, 2006.

[7] Anderson, P. W. Antiferromagnetism. Theory of Superexchange Interaction. *Phys. Rev. 79*, 2 (1950), 350–356.

[8] Anderson, P. W. New Approach to the Theory of Superexchange Interactions. *Phys. Rev. 115*, 1 (1959), 2–13.

[9] Asamitsu, A., Tomioka, Y., Kuwahara, H., and Tokura, Y. Current switching of resistive states in magnetoresistive manganites. *Nature 388*, 6637 (1997), 50–52.

[10] Ashcroft, N. W., and Mermin, N. D. *Solid State Physics*. Saunders College, 1976.

[11] Atkinson, A., Moon, D. P., Smart, D. W., and Taylor, R. I. Tracer diffusion studies in NiO bicrystals and polycrystals. *Journal of Material Science 21* (1986), 1747–1757.

[12] B. P. Löchel, H. H. S. Breakdown of passivity of nickel by fluoride. *J. Electrochem. Soc. 131*, 4 (1984), 713–723.

[13] Baek, I. G., Lee, M. S., Seo, S., Lee, M. J., Seo, D. H., Suh, D.-S., Park, J. C., Park, S. ., Kim, H. S., Yoo, I. K., Chung, U.-I., and Moon, J. T. Highly Scalable Non-volatile Resistive Memory using Simple Binary Oxide Driven by Asymmetric Unipolar Voltage Pulses. *IEEE Technical Digest International Electron Devices Meeting* (2004), 587–590.

[14] Baker, B. G., Johnson, B. B., and Maire, G. L. C. Photoelectric work function measurements on nickel crystals and films. *Surface Science 24* (1971), 572–586.

[15] Beck, A., Bednorz, J. G., Gerber, C., Rossel, C., and Widmer, D. Reproducible switching effect in thin oxide films for memory applications. *Appl. Phys. Lett. 77*, 1 (2000), 139–141.

[16] Biesinger, M. C., Payne, B. P., Lau, L. W. M., Gerson, A., and Smart, R. S. C. X-ray photoelectron spectroscopic chemical state quantification of mixed nickel metal, oxide and hydroxide systems. *Surf. Interface Anal. 41* (2009), 324–332.

[17] Biju, V., and Khadar, M. A. Ac conductivity of nanostructured nickel oxide. *J. Mater. Sci. 36* (2001), 5779–5787.

[18] Biju, V., and Khadar, M. A. DC conductivity of consolidated nanoparticles of NiO. *Mat. Res. Bull. 36* (2001), 21–33.

[19] Biju, V., and Khadar., M. A. Dielectric properties of nanostructured nickel oxide. *J. Mater. Sci. 38* (2003), 4055–4063.

[20] Boer, J. H. D., and Verwey, E. J. W. Semi-conductors with partially and with completely filled 3d-lattice bands. *Proc. Phys. Soc. 49*, 1 (1937), A59–A71.

[21] Bogatskii, D. P. DIAGRAMMA SOSTOYANIYA SISTEMY NI-O_2 I FIZIKO-KHIMICHESKAYA PRIRODA TVERDYKH FAZ V ETOI SISTEME. *Zh. Obshch. Khim 21*, 1 (1951), 3–10.

[22] Bosman, A. J., and Crevecoeur, C. Mechanism of the Electrical Conduction in Li-Doped NiO. *Phys. Rev. 144*, 2 (1966), 763–770.

[23] Bourgeois, S., and Perdereau, M. Sims study of the interaction of ni-o surfaces with h_2 and h_2o. *Surf. Sci. 117* (1982), 165–168.

[24] Bozano, L. D., Kean, B. W., Beinhoff, M., Carter, K. R., Rice, P. M., and Scott, J. C. Organic materials and thin-film structures for cross-point memory cells based on trapping in metallic nanoparticles. *Adv. Funct. Mater. 15*, 12 (2005), 1933–1939.

[25] Bransky, I., and Tallan, N. M. High-Temperature Defect Structure and Electrical Properties of NiO. *J. Chem. Phys. 49*, 3 (1968), 1243–1249.

[26] Brouwer, G. A GENERAL ASYMPTOTIC SOLUTION OF REACTION EQUATIONS COMMON IN SOLID-STATE CHEMISTRY. *Philips Res. Rept. 9*, 5 (1954), 366–376.

[27] Buchanan, D. A., Stathis, J. H., Cartier, E., and DiMaria, D. J. On the Relationship between Stress Induced Leakage Currents and Catastrophic Breakdown in Ultra-thin SiO_2 Based Dielectrics. *Microelectronic Engineering 36* (1997), 329–332.

[28] Buh, G. H., Hwang, I., and Park, B. H. Time-dependent electroforming in NiO resistive switching devices. *Appl. Phys. Lett. 95* (2009), 142101–1–3.

[29] Cagli, C., Nardi, F., and Ielmini, D. Modeling of set/reset operations in NiO-based resistive-switching memory (RRAM) devices. *IEEE Trans. Electron Devices 56*, 8 (2009), 1712–1720.

[30] Cappus, D., Xu, C., Ehrlich, D., Dillmann, B., Jr., C. A. V., Shamery, K. A., Kuhlenbeck, H., and Freund, H. J. Hydroxyl groups on oxide surfaces: Nio(100), nio(111) and cr_2o_3(111). *Chemical Physics 177* (1993), 533–546.

[31] Chang, S. H., Chae, S. C., Lee, S. B., Liu, C., Noh, T. W., Lee, J. S., andJ. H. Jang, B. K., Kim, M. Y., Kim, D. W., and Jung, C. U. Effects of heat dissipation on unipolar resistance switching in Pt/NiO/Pt capacitors. *App 92* (2008), 183507–1–3.

[32] Chen, H. L., Lu, Y. M., and Hwang, W. S. Characterization of sputtered NiO thin films. *Surface & Coating Technology 198* (2005), 138–142.

[33] Chen, H. L., Lu, Y. M., and Hwang, W. S. Thickness dependence of electrical and optical properties of sputtered Nickel oxide films. *Thin solid films 514* (2006), 361–365.

[34] Choi, J. S., and Moore, W. J. DIFFUSION OF NICKEL IN SINGLE CRYSTALS OF NICKEL OXIDE. *J. Phys. Chem 66* (1962), 1308–1311.

[35] Chopra, K. L. Avalanche-Induced Negative Resistance in Thin Oxide Films. *J. Appl. Phys. 36*, 1 (1965), 184–187.

[36] Courtade, L., Turquat, C., Muller, C., Lisoni, J., Goux, L., and Wouters, D. Improvement of resistance switching characteristics in NiO films obtained from controlled Ni oxidation. *Proceedings IEEE Non-Volatile Memory Symp.* (2007), 1–4.

[37] Cox, J. T., and Quinn, C. M. Conductivity measurements on cobalt and nickel oxides in highly-enriched oxygen atmospheres. *J. Mater. Sci. 4*, 1 (1969), 33–38.

[38] Danikas, M. G., and Papaschinopoulos, G. Thermal breakdown in solid dielectrics: A new approach. *J. Franklin Inst. 335B*, 4 (1998), 617–621.

[39] Dearnaley, G., Stoneham, A. M., and Morgan, D. V. Electrical phenomena in amorphous oxide films. *Rep. Prog. Phys. 33*, 3 (1970), 1129–1191.

[40] Degraeve, R., Ogier, J. L., Bellens, R., Roussel, P. J., Groeseneken, G., and Maes, H. E. A New Model for the Field Dependence of Intrinsic and Extrinsic Time-Dependent Dielectric Breakdown. *IEEE TRANSACTIONS ON ELECTRON DEVICES 45*, 2 (1998), 472–481.

[41] Delmon, B., and Roman, A. Kinetic study of the reduction of nickel oxide near its antiferromagnetic-paramagnetic transition. *J. Chem. Soc., Faraday Trans. 1 69* (1973), 941–948.

[42] Demtröder, W. *Molekülphysik: Theoretische Grundlagen und experimentelle Methoden*. Oldenbourg Verlag, 2013.

[43] Dubois, C., Monty, C., and Philibert, J. Oxygen self-diffusion in NiO single crystals. *Philosophical Magazine A 46*, 3 (1982), 419–433.

[44] Duval, A., Miserque, F., Tabarant, M., Nogier, J. P., and Gédéon, A. Influence of the oxygen partial pressure on the oxidation of inconel 617 alloy at high temperature. *Oxidation of Metals 74*, 5-6 (2010), 215–238.

[45] Einstein, A. Über die von der molekularkinetischen Theorie der Wärme geforderte Bewegung von in ruhenden Flüssigkeiten suspendierten Teilchen. *Annalen der Physik 17* (1905), 549.

[46] Elliott, S. R. A.c. conduction in amorphous chalcogenide and pnictide semiconductors. *Advances in Physics 36*, 2 (1987), 135–217.

[47] Eror, N. G., and Jr., J. B. W. Electrical Conductivity of Single Crystalline Nickel Oxide. *Phys. Stat. Sol. 35*, 2 (1969), 641–651.

[48] Fors, R., Khartsev, S. I., and Grishin, A. M. Giant resistance switching in metal-insulator-manganite junctions: evidence for Mott transition. *Phys. Rev. B 71*, 4 (2005), 45305–1–10.

[49] Frenkel, J. On Pre-Breakdown Phenomena in Insulators and Electronic Semi-Conductors. *Phys. Rev. 54*, 8 (1938), 647–648.

[50] Fueki, K., and J. B. Wagner, J. Studies of the Oxidation of Nickel in the Temperature Range of 900C to 1400C. *J. Electrochem. Soc. 112* (1965), 384–388.

[51] Fujii, T., Kawasaki, M., Sawa, A., Akoh, H., Kawazoe, Y., and Tokura, Y. Hysteretic current-voltage characteristics and resistance switching at an epitaxial oxide Schottky junction $SrRuO_3/SrTi_{0.99}Nb_{0.01}O_3$. *Appl. Phys. Lett. 86* (2005), 12107.

[52] Gibbons, J. F., and Beadle, W. E. Switching properties of thin NiO films. *Solid-State Electronics 7*, 11 (1964), 785–790.

[53] Gmelin, L., and Pietsch, E. H. *Gmelins Handbuch der Anorganischen Chemie, Nickel Teil B - Lieferung 2*, 8 ed. Verlag Chemie GmbH (Weinheim), 1966 (p378).

[54] Granqvist, C. G. *Handbook of Inorganic Electrochromic Materials*. Elsevier, Amsterdam, 1995.

[55] Grossmann, M., Lohse, O., Bolten, D., and Boettger, U. The interface screening model as origin of imprint in $PbZr_xTi_{1-x}O_3$ thin films. II. Numerical simulation and verification. *J. Appl. Phys. 92*, 5 (2002), 2688–2696.

[56] Guan, W., Long, S., Liu, M., Li, Z., Hu, Y., and Liu, Q. Fabrication and charging characteristics of MOS capacitor structure with metal nanocrystals embedded in gate oxide. *J. Phys. D: Appl. Phys. 40* (2007), 2754–2758.

[57] Gurfinkel, M., Horst, J. C., Suehle, J. S., Bernstein, J. B., Shapira, Y., Matocha, K. S., Dunne, G., and Beaupre, R. A. Time-Dependent Dielectric Breakdown of 4H-SiC/SiO_2 MOS Capacitors. *IEEE TRANSACTIONS ON DEVICE AND MATERIALS RELIABILITY, 8*, 4 (2008), 635–641.

[58] Hellwege, K. H., and Madelung, O. *Landolt-Brnstein: Numerical Data and Functional Relationships*, vol. 17g. Springer-Verlag, 1984.

[59] Heras, J. M., and Albano, E. V. Photoelectrical work function and electrical resistance measurements on iron, cobalt and nickel films annealed at temperatures between 77 and 478 K. *Thin Solid Films 106* (1983), 275–284.

[60] Hiatt, W. R., and Hickmott, T. W. BISTABLE SWITCHING IN NIOBIUM OXIDE DIODES. *Appl. Phys. Lett. 6*, 6 (1965), 106–108.

[61] Holländer, B., Heer, H., Wagener, M., Halling, H., and Mantl, S. New high-precision 5-axes RBS/channeling goniometer for ion beam analysis of 150 mm circle divided wafers. *NUCL. INST. B 161* (2000), 227–230.

[62] Ielmini, D., Cagli, C., and Nardi, F. Resistance transition in metal oxides induced by electronic threshold switching. *Appl. Phys. Lett. 94* (2009), 063511–1–3.

[63] Ielmini, D., Cagli, C., and Nardi, F. Physical models of size-dependent nanofilament formation and rupture in NiO resistive switching memories. *Nanotechnology 22*, 25 (2011), 254022.

[64] Ielmini, D., Nardi, F., and Cagli, C. Universal Reset Characteristics of Unipolar and Bipolar Metal-Oxide RRAM. *Electron Devices, IEEE Transactions on Electron Devices 58*, 10 (2011), 3246–3253.

[65] Ielmini, D., Nardi, F., Cagli, C., and Lacaita, A. L. Size-dependent retention time in NiO-based resistive switching memories. *IEEE Electron Device Lett. 31*, 4 (2010), 353–355.

[66] Inoue, I. H., Yasuda, S., Akinaga, H., and Takagi, H. Nonpolar resistance switching of a metal/binary transition metal oxides/metal sandwich: homogeneous/inhomogeneous transition of current distribution. *Phys. Rev. B 77* (2008), 035105–1–7.

[67] Irwin, M. D., Buchholz, D. B., Hains, A. W., Chang, R. P. H., and Marks, T. J. p-Type semiconducting nickel oxide as an efficiency-enhancing anode interfacial layer in polymer bulk-heterojunction solar cells. *PNAS 105*, 8 (2008), 2783–2787.

[68] Jang, W. L., Lu, Y. M., Hwang, W. S., Dong, C. L., Hsieh, P. H., Chen, C. L., Chan, T. S., and Lee, J. F. A study of thermal decomposition of sputtered nio films. *EPL 96* (2011), 37009–p1–p6.

[69] Jarzebski, Z. M., and Mrowec, S. Defect structure Model for Nickel Oxide. *Oxidation of Metals 1*, 2 (1969), 267–277.

[70] Jeong, D. S., Schroeder, H., and Waser, R. Impedance spectroscopy of TiO_2 thin films showing resistive switching. *Appl. Phys. Lett. 89*, 8 (2006), 2909–1–3.

[71] Jeong, D. S., Schroeder, H., and Waser, R. Coexistence of Bipolar and Unipolar Resistive Switching Behaviors in Pt/TiO2/Pt Stack. *Electrochemical and Solid-State Letters 10*, 8 (2007), G51–G53.

[72] Jung, K., Seo, H., Kim, Y., Ima, H., Hong, J., Park, J.-W., and Lee, J.-K. Temperature dependence of high- and low-resistance bistable states in polycrystalline NiO films. *Appl. Phys. Lett. 90* (2007), 052104–052106.

[73] Kampfrath, T., Sell, A., Klatt, G., Pashkin, A., Mhrlein, S., Dekorsy, T., Wolf, M., Fiebig, M., Leitenstorfer, A., and Huber, R. Coherent terahertz control of antiferromagnetic spin waves. *Nature Photonics 5* (2010), 31–34.

[74] Kao, K. C., and Hwang, W. *Electrical Transport in Solids - With Particular Reference to Organic Semiconductors.* Pergamon Press; 1st edition (February 1981), 1981.

[75] Karakasidis, T., and Meyer, M. Grain-boundary diffusion of cation vacancies in nickel oxide: A molecular-dynamics study. *Phys. Rev. B, Condens. Matter 55*, 20 (1997), 13853–13864.

[76] Kever, T., Klopstra, B., Boettger, U., and Waser, R. On the Existence of Two Different Resistive Switching Mechanisms in Metal Organic Charge Transfer Complex Thin Films. *IEEE Non Volatile Memory Technology Symposium 2006* (2006), 116–119.

[77] Kim, D. S., Kim, Y. H., Lee, C. E., and Kim, Y. T. Colossal electroresistance mechanism in a $Au/Pr_{0.7}Ca_{0.3}MnO_3/Pt$ sandwich structure: evidence for a Mott transition. *Phys. Rev. B 74*, 17 (2006), 174430–1–6.

[78] Kim, K. S., and Winograd, N. X-Ray Photoelectron Spectroscopic Studies of Nickel-Oxygen Surfaces using Oxygen and Argon Ion-Bombardement. *Surface Science 43* (1974), 625–643.

[79] Kim, K. S., and Winograd, N. X-ray photoelectron spectroscopic studies of nickel-oxygen surfaces using oxygen and argon ion-bombardment. *Surf. Sci. 43* (1974), 625–643.

[80] Kim, M. G., , Kim, S. M., Choi, E. J., Moon, S. E., Park, J., Kim, H. C., Park, B. H., Lee, M. J., Seo, S., Seo, D. H., Ahn, S. E., and Yoo, I. K. Study of Transport and Dielectric of Resistive Memory States in NiO Thin Film. *Jpn. J. Appl. Phys. 44*, 42 (2005), L1301–L1303.

[81] Kinoshita, K., Tamura, T., Aoki, M., Sugiyama, Y., and Tanaka, H. Bias polarity dependent data retention of resistive random access memory consisting of binary transition metal oxide. *Appl. Phys. Lett. 89* (2006), 103509–1–3.

[82] Kinoshita, K., Tamura, T., Aoki, M., Sugiyama, Y., and Tanaka, H. Lowering the switching current of resistance random access memory using a hetero junction structure consisting of transition metal oxides. *Jpn. J. Appl. Phys. Part 2 - Lett. Express Lett. 45*, 37 (2006), L991–L994.

[83] Kinoshita, K., Tsunoda, K., Sato, Y., Noshiro, H., Yagaki, S., Aoki, M., and Sugiyama, Y. Reduction in the reset current in a resistive random access memory consisting of NiO_x brought about by reducing a parasitic capacitance. *Appl. Phys. Lett. 93* (2008), 033506–1–3.

[84] Kohmoto, O., Nakagawa, H., Ono, F., and Chayahara, A. Ni-defective value and resistivity of sputtered NiO films. *Journal of Magnetism and Magnetic Materials 226-230* (2001), 1627–1628.

[85] Kondo, J. N., Shibata, S., Ebina, Y., Domen, K., and Tanaka, A. Preparation of a sio_2-pillared $k_{0.8}fe_{0.8}ti_{1.2}o_4$ and ir study of n_2 adsorption. *J. Phys. Chem. 99*, 43 (1995), 16043–16046.

[86] Kozicki, M. N., Yun, M., Yang, S.-J., Aberouette, J. P., and Bird, J. P. Nanoscale effects in devices based on chalcogenide solid solutions. *Supper 27*, 5-6 (2000), 485–488.

[87] Kröger, F. A. *The Chemistry of Imperfect Crystals*. North-Holland Publ. Co., Amsterdam, 1964.

[88] Kröger, F. A., and Vink, H. J. *Solid State Physics*, vol. 3. Academic Press, New York, 1956.

[89] Kügeler, C., Rosezin, R., Weng, R., Menzel, S., Klopstra, B., Boettger, U., and Waser, R. Fast resistive switching in WO_3 thin films for non-volatile memory applications. *Proceedings of the 9th IEEE Conference on Nanotechnology* (2009), 900–903.

[90] Kügeler, C., Weng, R., Schroeder, H., Symanczyk, R., Majewski, P., Ufert, K.-D., Waser, R., and Kund, M. Study on the dynamic resistance switching properties of NiO thin films. *Thin Solid Films 518*, 8 (2008), 2258–2260.

[91] Kügeler, C., Zhang, J., Hoffmann-Eifert, S., Kim, S. K., and Waser, R. Nanostructured resistive memory cells based on 8-nm-thin TiO_2 films deposited by atomic layer deposition. *J. Vac. Sci. Technol. B 29*, 1 (2011), 1AD01/1–5.

[92] Kuiper, P., Kruizinga, G., Ghijsen, J., Sawatzky, G. A., and Verweij, H. Character of Holes in $Li_xNi_{1-x}O_2$ and Their Magnetic Behaviour. *Phys. Rev. Lett. 62*, 2 (1989), 221–224.

[93] Kumari, S. V., Natarajan, M., Vaidyan, V. K., and Koshy, P. Surface oxidation of nickel thin films. *J. Mater. Sci. Lett. 11* (1992), 761–762.

[94] Lee, C. T., Lin, Y. J., and Lee, T. H. Mechanism investigation of NiO_x in Au/Ni/p-Type GaN Ohmic contacts annealed in air. *Journal of Electronic Materials 32*, 5 (2003), 341–345.

[95] Lee, M. J., Han, S., Jeon, S. H., Park, B. H., Kang, B. S., Ahn, S. E., Kim, K. H., Lee, C. B., Kim, C. J., Yoo, I. K., Seo, D. H., Li, X. S., Park, J. B., Lee, J. H., and Park, Y. Electrical Manipulation of Nanofilaments in Transition-Metal Oxides for Resistance-Based Memory. *Nano Lett. 9*, 4 (2009), 1476–1481.

[96] Lee, S. B., Chae, S. C., Chang, S. H., Lee, J. S., Seo, S., Kahng, B., and Noh, T. W. Scaling behaviors of reset voltages and currents in unipolar resistance switching. *Appl. Phys. Lett. 93* (2008), 212105–1–3.

[97] Li, D., Hu, J., Wu, R., and Lu, J. G. Conductometric chemical sensor based on individual cuo nanowires. *Nanotechnology 21* (2010), 485502–1–6.

[98] Li, W. X., Österlund, L., Vestergaard, E. K., Vang, R. T., Matthiesen, J., Pedersen, T. M., Laegsgaard, E., Hammer, B., and Besenbacher, F. Oxidation of pt(110). *Phys. Rev. Lett. 93*, 14 (2004), 146104–1–4.

[99] Lide, D. R., Ed. *CRC Handbook of Chemistry and Physics: A ready-reference book of chemical and physical data*, 86 ed. CRC Taylor & Francis, 2009.

[100] Long, A. R. Frequency-dependent loss in amorphous semiconductors. *Advances in Physics 31*, 5 (1982), 553–637.

[101] Lunkenheimer, P., Loidl, A., Ottermann, C. R., and Bange, K. Correlated barrier hopping in NiO films. *Phys. Rev. B 44*, 11 (1991), 5927–5930.

[102] MacDonald, J. R., Ed. *Impedance Spectroscopy*. Wiley, New York, 1969.

[103] Makhlouf, S. A. Electrical properties of NiO films obtained by high-temperature oxidation of nickel. *Thin Solid Films 516* (2008), 3112–3116.

[104] McIntyre, N. S., and Cook, M. G. X-ray photoelectron studies on some oxides and hydroxides of cobalt, nickel, and copper. *Anal. Chem. 47*, 13 (1975), 2208–2213.

[105] McKay, J. M., and Henrich, V. E. Surface electronic structure of nio: Defect states, o_2 and h_2o interactions. *Phys. Rev. B 32*, 10 (1985), 6764–6772.

[106] McPherson, J., Kim, J.-Y., Shanware, A., and Mogul, H. Thermochemical description of dielectric breakdown in high dielectric constant materials. *Appl 82*, 13 (2003), 2121–2123.

[107] McPherson, J. W., Khamankar, R. B., and Shanware, A. Complementary model for intrinsic time-dependent dielectric breakdown in sio2 dielectrics. *J. Appl. Phys. 88*, 9 (2000), 5351–5359.

[108] McPherson, J. W., and Mogul, H. C. Underlying physics of the thermochemical e model in describing low-field time-dependent dielectric breakdown in sio_2 thin films. *J. Appl. Phys. 84*, 3 (1998), 1513–1523.

[109] Meijer, G. I., Staub, U., Janousch, M., Johnson, S. L., Delley, B., and Neisius, T. Valence states of Cr and the insulator-to-metal transition in Cr-doped $SrTiO_3$. *Phys. Rev. B 72* (2005), 155102–1–5.

[110] Menke, T., Meuffels, P., Dittmann, R., Szot, K., and Waser, R. Separation of bulk and interface contributions to electroforming and resistive switching behavior of epitaxial Fe-doped $SrTiO_3$. *J. Appl. Phys. 105*, 6 (2009), 066104–1–3.

[111] Merlin, R., Martin, T., Polian, A., Cardona, M., Andlauer, B., and Tannhauser, D. TWO MAGNON RESONANT RAMAN SCATTERING IN TRANSITION METAL OXIDES. *J. Magn. Magn. Mat. 9* (1978), 83–85.

[112] Moore, G. E. Cramming more Components onto Integrated Circuits. *Electronics 38*, 8 (1965), 114–117.

[113] Moore, G. E. No exponential is forever: but "Forever" can be delayed! [semiconductor industry]. *Dig. Tech. Papers IEEE Solid-State Circuits Conf. (ISSCC) 2003 1* (2003), 20–23.

[114] Moore, W. J. *Der Feste Zustand*. Vieweg, 1977.

[115] Moriya, T. *Electron Correlation and Magnetism in Narrow-Band Systems*. Springer Series in Solid-State Sciences. Springer, 1981.

[116] Mortimer, C. E. *Chemie : das Basiswissen der Chemie*. Thieme, 2007.

[117] Mott, N. F. The Basis of the Electron Theory of Metals, with Special Reference to the Transition Metals. *Proc. Phys. Soc. A 62*, 7 (1949), 416–422.

[118] Mott, N. F., and Peierls, R. Discussion of the paper by De Boer and Verwey. *Proc. Phys. Soc. 49* (1937), 72–73.

[119] Mrowec, S., and Grzesik, Z. Oxidation of nickel and transport properties of nickel oxide. *Journal of Physics and Chemistry of Solids 65* (2004), 1651–1657.

[120] Muenstermann, R., Dittmann, R., Szot, K., Mi, S., Jia, C.-L., Meuffels, P., and Waser, R. Realization of regular arrays of nanoscale resistive switching blocks in thin films of Nb-doped $SrTiO_3$. *Appl. Phys. Lett. 93*, 2 (2007), 23110–1–3.

[121] Münstermann, R., Menke, T., Dittmann, R., and Waser, R. Coexistence of filamentary and homogeneous resistive switching in fe-doped $srtio_3$ thin film memristive devices. *Adv. Mater. 22* (2010), 4819–4822.

[122] Nachman, M., Cojocaru, L. N., and Ribco, L. V. Electrical properties of non-stoichiometric nickel oxide. *phys. stat. sol. 8* (1965), 773–783.

[123] Nardi, F., Ielmini, D., Cagli, C., Spiga, S., Fanciulli, M., Goux, L., and Wouters, D. J. Control of filament size and reduction of reset current below 10 μA in NiO resistance switching memories. *Solid-State Electronics 58* (2011), 42–47.

[124] Natile, M. M., and Glisenti, A. Surface Reactivity of NiO: Interaction with Methanol. *Chem. Mater. 14* (2002), 4895–4903.

[125] Nauenheim, C., Kuegeler, C., Ruediger, A., and Waser, R. Investigation of the electroforming process in resistively switching TiO_2 nanocrosspoint junctions. *Appl. Phys. Lett. 96*, 12 (2010), 122902–1–3.

[126] Ohring, M. *The Materials Science of Thin Films*. Academic Press, Inc., 1991.

[127] O'Keefe, M., and Moore, W. J. DIFFUSION OF OXYGEN IN SINGLE CRYSTALS OF NICKEL OXIDE. *J. Phys. Chem. 65* (1961), 1438–1439.

[128] Osburn, C. M., and Vest, R. W. Defect structure and electrical properties of NiO - I. High temperature. *J. Phys. Chem. Solids 32* (1971), 1331–1342.

[129] Oswald, S., and Brückner, W. XPS depth profile analysis of non-stoichiometric NiO films. *Surf. Interface Anal. 36* (2004), 17–22.

[130] Ouyang, J., Chu, C. W., Szmanda, C. R., Ma, L., and Yang, Y. Programmable polymer thin film and non-volatile memory device. *Nat. Mater. 3*, 12 (2004), 918–922.

[131] Ovshinsky, S. R. Reversible Electrical Switching Phenomena in Disordered Structures. *Phys. Rev. Lett. 21*, 20 (1968), 1450–1453.

[132] Oxley, D. P. Electroforming, Switching and Memory effects in oxide thin films. *Electrocomp. Sci. Technol. 3* (1977), 217–224.

[133] Pagnia, H., and Sotnik, N. Bistable Switching in Electroformed Metal-Insulator-Metal Devices. *Phys. Stat. Sol. A 108*, 1 (1988), 11–65.

[134] Pancharatnam, S., Huggins, R. A., and Mason, D. M. Catalytic decomposition of nitric oxide on zirconia by electrolytic removal of oxygen. *J. Electrochem. Soc. 122*, 7 (1975), 869–875.

[135] Park, C., Jeon, S. H., Chae, S. C., Han, S., Park, B. H., Seo, S., and Kim, D.-W. Role of structural defects in the unipolar resistive switching characteristics of pt/nio/pt structures. *Appl. Phys. Lett. 93* (2008), 042102–1–3.

[136] Park, G. S., Li, X. S., Kim, D. C., Jung, R. J., Lee, M. J., and Seo, S. Observation of electric-field induced Ni filament channels in polycrystalline NiOx film. *Appl. Phys. Lett. 91* (2007), 222103–1–3.

[137] Park, J. W., Park, J. W., Jung, K., Yang, M. K., and Lee, J. K. Influence of oxygen content on electrical properties of NiO films grown by rf reactive sputtering for resistive random-access memory applications. *J. Vac. Sci. Technol. B 24*, 5 (2006), 2205–2208.

[138] Pike, G. E. ac Conductivity of Scandium Oxide and a New Hopping Model for Conductivity. *Phys. Rev. B 6*, 4 (1972), 1572–1580.

[139] Pizzini, S., and Morlotti, R. Thermodynamic and Transport Properties of Stoichiometric and Nonstoichiometric Nickel Oxide. *J. Electrochem. Soc. 114*, 11 (1967), 1179–1189.

[140] Potember, R. S., Poehler, T. O., and Cowan, D. O. Electrical switching and memory phenomena in Cu-TCNQ thin films. *Appl. Phys. Lett. 34*, 6 (1979), 405–407.

[141] Powell, R. J., and Spicer, W. E. Optical properties if NiO and CoO. *Phys. Rev. B 2*, 6 (1970), 2182–2193.

[142] Rao, K. V., and Smakula, A. Dielectric Properties of Cobalt Oxide, Nickel Oxide, and Their Mixed Crystals. *J. Appl. Phys. 36*, 6 (1965), 2031–2038.

[143] Ristova, M., Velevska, J., and Ristov, M. Chemical bath deposition and electrochromic properties of NiO_x films. *Solar Energy Materials & Solar Cells 71* (2002), 219–230.

[144] Rooksby, H. P. A note on the structure of nickel oxide at subnormal and elevated temperatures. *Acta Cryst. 1* (1948), 226.

[145] Rosezin, R., Meier, M., Trellenkamp, S., Kuegeler, C., and Waser, R. Observation of unipolar resistance switching in silver doped methyl-silsesquioxane. *Microelectron. Eng. 87* (2010), 1531–1533.

[146] Rosin, P., and Rammler, E. The Laws Governing the Fineness of Powdered Coal. *Journal of the Institute of Fuel 7* (1933), 29–36.

[147] Russo, U., Ielmini, D., Cagli, C., and Lacaita, A. L. Filament conduction and reset mechanism in NiO-based resistive-switching memory (RRAM) devices. *IEEE Trans. Electron Devices 56*, 2 (2009), 186–192.

[148] Russo, U., Ielmini, D., Cagli, C., Lacaita, A. L., Spiga, S., Wiemer, C., Perego, M., and Fanciulli, M. Conductive-filament switching analysis and self-accelerated thermal dissolution model for reset in NiO-based RRAM. *IEEE International Electron Devices Meeting 2*, 1 (2007), 775–778.

[149] Sasi, B., and Gopchandran, K. G. Nanostructured mesoporous nickel oxide thin films. *Nanotechnology 18* (2007), 115613–1–6.

[150] Sawa, A., Fujii, T., Kawasaki, M., and Tokura, Y. Interface resistance switching at a few nanometer thick perovskite manganite active layers. *Appl. Phys. Lett. 88* (2006), 232112.

[151] Sawatzky, G. A., and Allen, J. W. Magnitude and Origin of the Band Gap in NiO. *Phys. Rev. Lett. 53*, 24 (1984), 2339–2342.

[152] Schindler, C., Staikov, G., and Waser, R. Electrode kinetics of Cu-SiO_2-based resistive switching cells: Overcoming the voltage-time dilemma of electrochemical metallization memories. *Appl. Phys. Lett. 94*, 7 (2009), 072109–1–3.

[153] Seo, S., Lee, M. J., Kim, D. C., Ahn, S. E., Park, B.-H., Kim, Y. S., Yoo, I. K., Byun, I. S., Hwang, I. R., Kim, S. H., Kim, J.-S., Choi, J. S., Lee, J. H., Jeon, S. H., Hong, S. H., and Park, B. H. Electrode dependence of resistance switching in polycrystalline NiO films. *Appl. Phys. Lett. 87* (2005), 263507–1–3.

[154] Seo, S., Lee, M. J., Seo, D. H., Choi, S. K., Suh, D. S., Joung, Y. S., Yoo, I. K., Byun, I. S., Hwang, I. R., Kim, S. H., and Park, B. H. Conductivity switching characteristics and reset currents in NiO films. *Appl. Phys. Lett. 86*, 9 (2005), 93509–1–3.

[155] Seo, S., Lee, M. J., Seo, D. H., Jeoung, E. J., Suh, D.-S., Joung, Y. S., Yoo, I. K., Hwang, I. R., Kim, S. H., Byun, I. S., Kim, J.-S., Choi, J. S., and Park, B. H. Reproducible resistance switching in polycrystalline NiO films. *Appl. Phys. Lett. 85*, 23 (2004), 5655–5657.

[156] Shen, W., Dittman, R., and Waser, R. Reversible alternation between bipolar and unipolar resistive switching in polycrystalline barium strontium thin films. *J. Appl. Phys. 107* (2010), 094506.

[157] Shim, M. T., and Moore, W. J. Diffusion of Nickel in Nickel Oxide. *J. Chem. Phys. 26*, 4 (1957), 802–804.

[158] Shima, H., Takano, F., and Akinaga, H. Resistance switching in the metal deficient-type oxides: NiO and CoO. *Appl. Phys. Lett. 91* (2007), 012901–1–3.

[159] Simmons, J. G. Transition from Electrode-Limited to Bulk-Limited Conduction Processes in Metal-Insulator-Metal Systems. *Phys. Rev. 166*, 3 (1968), 912–920.

[160] Simmons, J. G., and Verderber, R. R. New conduction and reversible memory phenomena in thin insulating films. *Proc. Roy. Soc. A 301* (1967), 77–102.

[161] Soni, R., Meuffels, P., Petraru, A., Weides, M., Kgeler, C., Waser, R., and Kohlstedt, H. Probing Cu doped $Ge_{0,3}Se_{0,7}$ based resistance switching memory devices with random telegraph noise. *J. Appl. Phys. 107* (2010), 024517–1–10.

[162] Soriano, L., Gutiérrez, A., Preda, I., Palacin, S., Sanz, J. M., Abbate, M., Trigo, J. F., Vollmer, A., and Bressler, P. R. Splitting of Ni 3*d* states at the surface of NiO nanostructures. *Phys. Rev. B 74* (2006), 193402–1–4.

[163] Stanescu, S., Boeglin, C., Barbier, A., and Deville, J. P. Growth mode of NiO on Cu(111) studied using scanning tunneling microscopy and surface x-ray diffraction. *Phys. Rev. B 67* (2003), 035419.

[164] Strachan, J. P., Yang, J. J., Münstermann, R., Scholl, A., Medeiros-Ribeiro, G., Stewart, D. R., and Williams, R. S. Structural and chemical characterization of Tio_2 memristive devices by spatially-resolved NEXAFS. *Nanotechnology 20* (2009), 485701.

[165] Strukov, D. B., Snider, G. S., Stewart, D. R., and Williams, R. S. The missing memristor found. *Nature 453* (2008), 80–83.

[166] Strukov, D. B., and Williams, R. S. Exponential ionic drift: fast switching and low volatility of thin-film memristors. *Appl. Phys. A 94* (2009), 515–519.

[167] Suehle, J. S. Ultrathin Gate Oxide Reliability: Physical Models, Statistics, and Characterization. *IEEE TRANSACTIONS ON ELECTRON DEVICES 49*, 6 (2002), 958–971.

[168] Szot, K., Bruchhaus, R., and Weng, R. Optisches speichermaterial und verfahren zur speicherung. *European Patent (EP2521123A1)* (2011).

[169] Thornton, J. A. High rate thick film growth. *Ann. Rev. Mater. Sci. 7* (1977), 239–260.

[170] Tsunoda, K., Kinoshita, K., Noshiro, H., Yamazaki, Y., Iizuka, T., Ito, Y., Takahashi, A., Okano, A., Sato, Y., Fukano, T., Aoki, M., and Sugiyama, Y. Low Power and High Speed Switching of Ti-doped NiO ReRAM under the Unipolar Voltage Source of less than 3 V. *Electron Devices Meeting, 2007. IEDM 2007. IEEE International* (2007), 767–770.

[171] Tung, C. H., Pey, K. L., Lin, W. H., and Radhakrishnan, M. K. Polarity-Dependent Dielectric Breakdown-Induced Epitaxy (DBIE) in Si MOSFETs. *IEEE ELECTRON DEVICE LETTERS 23*, 9 (2002), 526–528.

[172] Uhlenbrock, S., Scharfschwerdt, C., M. Neumann, G. I., and Freund, H. The influence of defects on the ni 2p and o 1s xps of nio. *J. Phys.: Condens. Matter 4* (1992), 7973–7978.

[173] Uno, R. Electrical Conduction of NiO at High Temperature. *J. Phys. Soc. Jpn. 22* (1967), 1502.

[174] van der Heide, P. *X-ray Photoelectron Spectroscopy: An introduction to Principles and Practices*. Wiley, 2012.

[175] Wagner, C. D., Riggs, W. M., Davis, L. E., and Moulder, J. F. *Handbook of X-ray Photoelectron Spectroscopy*. Englewood Cliffs, NJ: Prentice-Hall, 1979.

[176] Waser, R., Ed. *Nanoelectronics and Information Technology*, 2 ed. Wiley-VCH, Weinheim, 2005.

[177] Waser, R., Dittman, R., Staikov, G., and Szot, K. Redox-Based Resistive Switching Memories - Nanoionic Mechanisms, Prospects, and Challenges. *Adv. Mater. 21* (2009), 2632–2663.

[178] Watanabe, Y. Reproducible memory effect in the leakage current of epitaxial ferroelectric/conductive perovskite heterostructures. *Appl. Phys. Lett. 66*, 1 (1995), 28–30.

[179] Wazzan, A. R. Lattice and Grain Boundary Self-Diffusion in Nickel. *J. Appl. Phys. 36*, 11 (1965), 3596–3599.

[180] Wittenauer, M. A., and Zandt, L. L. V. Surface conduction versus bulk conduction in pure stoichiometric NiO crystals. *Philos. Mag. B 46*, 6 (1982), 659–667.

[181] Wruck, D. A., and Rubin, M. Structure and electronic properties of electrochromic nio films. *J. Electrochem. Soc. 140*, 4 (1993), 1097–1104.

[182] Year, J. R., and Taylor, H. L. The Poole-Frenkel Effect with Compensation Present. *J. Appl. Phys. 39*, 12 (1968), 5600–5604.

[183] Yoshida, C., Kinoshita, K., Yamasaki, T., and Sugiyama, Y. Direct observation of oxygen movement during resistance switching in nio/pt film. *Appl. Phys. Lett. 93* (2008), 042106–1–3.

[184] Yun, J.-B., Kim, S., Seo, S., Lee, M.-J., Kim, D.-C., Ahn, S.-E., Park, Y., Kim, J., and Shin, H. Random and localized resistive switching observation in Pt/NiO/Pt. *Phys. Stat. Sol. 1*, 6 (2007), 280–282.

Band / Volume 96
Immunohistochemical and electrophysiological characterization of the mouse model for Retinitis Pigmentosa, *rd10*
S. Biswas (2014), XII, 119 pp
ISBN: 978-3-95806-011-1

Band / Volume 97
Single molecule localization microscopy: Imaging of cellular structures and a new three-dimensional localization technique
X. Fan (2014), XII, 92 pp
ISBN: 978-3-95806-014-2

Band / Volume 98
Cryogenic Break-Junction Characterization of Single Organic Molecules
T. Grellmann (2014), VI, 86 pp
ISBN: 978-3-95806-015-9

Band / Volume 99
Interacting Interactions: A Study on the Interplay of Molecule-Molecule and Molecule-Substrate Interactions at Metal-Organic Interfaces
M. Willenbockel (2014), IX, 245 pp
ISBN: 978-3-95806-018-0

Band / Volume 100
Microwire crossbar arrays for chemical, mechanical, and thermal stimulation of cells
P. Rinklin (2015), xii, 184 pp
ISBN: 978-3-95806-022-7

Band / Volume 101
Modification and characterization of potential bioelectronic interfaces
K. Greben (2015), 76 pp
ISBN: 978-3-95806-028-9

Band / Volume 102
Extending the precision and efficiency of the all-electron full-potential linearized augmented plane-wave density-functional theory method
G. Michalicek (2015), 195 pp
ISBN: 978-3-95806-031-9

Band / Volume 103
Metabolic engineering of *Escherichia coli* for the production of plant phenylpropanoid derived compounds
P. V. van Summeren-Wesenhagen (2015), V, 92 pp
ISBN: 978-3-95806-039-5

Band / Volume 104
Spin-reorientation transition in epitaxial Ni_xPd_{1-x} fims on Cu(001): a microscopic analysis
D. Gottlob (2015), x, 134 pp
ISBN: 978-3-95806-049-4

Band / Volume 105
Resonant Magnetic Scattering Studies using Synchrotron Radiation and Laser-Generated Extreme Ultraviolet Light
C. M. Weier (2015), vii, 143 pp
ISBN: 978-3-95806-052-4

Band / Volume 106
Neutron Scattering
Lectures of the JCNS Laboratory Course held at Forschungszentrum Jülich and at the Heinz-Maier-Leibnitz Zentrum Garching
edited by Th. Brückel, D. Richter, G. Roth, A. Wischnewski and R. Zorn (2015), ca 300 pp
ISBN: 978-3-95806-055-5

Band / Volume 107
Neutron Scattering
Experimental Manuals of the JCNS Laboratory Course held at Forschungszentrum Jülich and at the Heinz-Maier-Leibnitz Zentrum Garching
edited by Th. Brückel, D. Richter, G. Roth, A. Wischnewski and R. Zorn (2015), ca 150 pp
ISBN: 978-3-95806-056-2

Band / Volume 108
STM-based quantum transport through molecular wires
N. Fournier (2015), ix, 295 pp
ISBN: 978-3-95806-059-3

Band / Volume 109
Study on the electroforming and resistive switching behaviour of nickel oxide thin films for non-volatile memory applications
R. Weng (2015), xxi, 159 pp
ISBN: 978-3-95806-062-3

Schlüsseltechnologien /
Key Technologies
Band / Volume 109
ISBN 978-3-95806-062-3